Prevention of Biofouling in Seawater Desalination via Initiated Chemical Vapor Deposition (iCVD)

by

Rong Yang

B.S. Chemical Engineering
Tsinghua University, Beijing, China, 2009

M.S. Chemical Engineering Practice
Massachusetts Institute of Technology, 2012

SUBMITTED TO THE DEPARTMENT OF CHEMICAL ENGINEERING
IN PARTIAL FULFILLMENT OF THE REQUIREMENTS FOR THE DEGREE OF

DOCTOR OF PHILOSOPHY IN CHEMICAL ENGINEERING
AT THE
MASSACHUSETTS INSTITUTE OF TECHNOLOGY

JUNE 2014

Signature of Author: _Signature redacted_______________

Department of Chemical Engineering
May 5, 2014

Certified by: ______Signature redacted_______________

Karen K. Gleason
Alexander and I. Michael Kasser Professor of Chemical Engineering
Thesis Supervisor

Accepted by: __________Signature redacted_______________

Patrick S. Doyle
Professor of Chemical Engineering
Chairman, Committee for Graduate Students

Prevention of Biofouling in Seawater Desalination via Initiated Chemical Vapor Deposition (iCVD)

by

Rong Yang

Submitted to Department of Chemical Engineering
on May 5, 2014 in Partial Fulfillment of the
Requirements for the Degree of
Doctor of Philosophy in Chemical Engineering

ABSTRACT

Biofouling, the undesirable settlement and growth of organisms, occurs immediately when a clean surface is immersed in natural seawater. It is a universal problem and the bottleneck for seawater desalination, which reduces both the yield and the quality of desalted water. Mitigation of fouling in a desalination operation is an on-going challenge due to the delicate nature of desalination membranes, the vast diversity of fouling organisms, and the additional cross-membrane transport resistance exerted by an extra layer of coating. This thesis focuses on benign interface engineering methods and ultra-thin zwitterionic coating synthesis to bridge this gap in surface modification strategies. The direct application of ultra-thin coatings on commercial membranes with intact membrane performance has been enabled by a room-temperature vapor treatment called initiated chemical vapor deposition (iCVD). Diffusion-limited reaction conditions have shown to significantly improve the surface concentration of the antifouling zwitterionic moieties, which is crucial to the fouling resistance of modified membranes. Robustness of the ultra-thin coating is enhanced through cross-linking and covalent attachment between the membrane and the film. The resulting durability of the antifouling coating and its resistance to oxidative reagents lead to an unprecedented synergistic effect that is critical to long-term fouling resistance, which provides unique insight into the adhesion of microbial foulant and promises to lower the price of freshwater in water-scarce countries, where desalination may serve as the only viable means to provide the water supply necessary to sustain agriculture, support personal consumption, and promote economic development.

Thesis Supervisor: Karen K. Gleason
Title: Alexander and I. Michael Kasser Professor of Chemical Engineering

Acknowledgements

It has been truly amazing what I have learnt and accomplished throughout my five years at MIT, much of which would not be possible without the support of many generous people. I would like to thank all, who have helped me get to this point. I am truly grateful.

First and foremost, I would like to express my deepest thanks to my advisor, Professor Karen Gleason for teaching me almost everything I have known about research and being a researcher. I am indebted to Karen for her patience, guidance, technical help and moral support. If it were not for her immense support and encouragement, I would never be pursuing an academic career path that I truly desire. Karen has been an incredible advisor, mentor and role model in all aspects of my academic life.

I would also like to gratefully acknowledge the help and support from Professor Bradley Olsen, an invaluable mentor during my time at MIT. I thank him for the insightful advice, scientifically and beyond, and for believing in me and generously dedicating so much of his time and effort to my various endeavors. I thank Professor Evelyn Wang for her support and comments as a member of my thesis committee.

The Gleason group, past and present, has been an exceptional environment of collaboration and support. A special thanks to David Borrelli for being an incredible classmate, colleague and friend. I have also thoroughly enjoyed collaborating with Christy Petruczok, Gozde Ozaydin-Ince, Jingjing Xu, Priya Moni, Andong Liu, and Baby Reeja Jayan. Gozde Ozaydin-Ince, Ayse Asatekin, and Jingjing Xu were amazingly helpful in guiding me through my first year in the lab. Additional thanks to Rachel Howden, Mahriah Alf, Miles Barr, Anna Coclite, Jose Yague, Francois De Luca, Asli Katmis, Nan Chen, Xiaoxue Wang, Peter Kovacik, and Amelia Servi for valuable discussions and being great company in the lab.

This thesis has benefitted tremendously from cross-department collaborations. I am grateful for the enthusiastic discussions and insightful feedbacks from Professor Tonio Buonassisi. I want to thank Yaron Segal in the Buonassisi group for his help in the lab and thoughtful discussions. Special thanks go to Professor Roman Stocker for his scientific support and incredible passion over the past year. I have truly enjoyed working with Hongchu Jang and Roberto Rusconi in the Stocker group and am excited to include some of our findings in this thesis. I also want to thank Jonathan Shu from Cornell Center for Material Research, Omar Khan from the Anderson group at MIT, Professor Chiesa Matteo and Carlo Amadei from Masdar Institute of Science and Technology in Abu Dhabi for the fruitful collaborations.

The research was generously supported by DOE office of ARPA-E and King Fahd University of Petroleum and Minerals in Dhahran, Saudi Arabia through the Centre for Clean Water and Clean Energy at MIT. Through this support, I have had the pleasure of working with many researchers with extraordinary passion on water research. I thank Bumjoo Kim, Si Won Choi, Jason Kovacs, and Simon Choong for sharing this passion with me, and for their constant help and support.

Additional thanks go to many wonderful people outside of the lab. To Gwen Wilcox and Joel Dashnaw, for their unconditional help at all times. To my classmates for their camaraderie and many fond memories, notably Siddarth Srinivasan, Amanda DiIenno, and Hyomin Lee for their technical supports and for introducing me to new and exciting research areas. Special thanks to Po-Yen Chen, for being an incredible collaborator and friend. I have especially appreciated his continuous wholehearted support, amazing intellectual curiosity and creativity. There are countless others, and my sincerest appreciation goes out to all; I would not have reached MIT without them.

Finally, I would like to thank my family, particularly my parents for their unconditional love and support. They have instilled in me the curiosity to observe and explore the world, the courage to follow my heart, and the persistence to proceed through the highs and lows of life, for which I will be forever grateful.

Table of Content

List of Figures

List of Tables

List of Acronyms and Abbreviations

4VP	4-vinylpyridine
AA	acrylic acid
AFM	atomic force microscope
ALD	atomic layer deposition
ARPA-E	Advanced Research Projects Agency-Energy
ARXPS	angle-resolved X-ray photoelectron spectroscopy
ATRP	atom transfer radical polymerization
BSA	bovine serum albumin
CA	contact angle
CCMR	Cornell Center for Materials Research
CMSE	Center for Materials Science and Engineering
CVD	chemical vapor deposition
DCA	dynamic contact angle
DD	1,9-decadiene
DI water	deionized water
DMAEMA	2-(dimethylamino)ethyl methacrylate
DMMSA	N,N-dimethyl-N-methacryloxyethyl-N-(3-sulfopropyl)
DOE	Department of Defense
DOPA	3,4-dihydroxyphenyl-L-alanine
DTGS	deuterated triglycine sulfate
DVB	divinylbenzene
E.coli	*Escherichia coli*
EGDA	ethylene glycol diacrylate
EGDMA	ethylene glycol dimethacrylate
E-I	ethanol-iodine
FTIR	Fourier transform infrared
gCVD	grafted chemical vapor deposition
HA	humic acid
HEMA	2'-hydroxythyl methacrylate
iCVD	initiated chemical vapor deposition
ISN	institute for soldier nanotechnologies
KFUPM	King Fahd University of Petroleum and Minerals
NF	nanofiltration
MFC	mass flow controller

OEG	olig(ethylene glycol)
P4VP	poly(4-vinylpyridine)
P(4VP-*co*-DVB)	poly(4-vinylpyridine-*co*-divinylbenzene)
PA	polyamide
PBS	phosphate buffered saline
PEGDA	poly(ethylene glycol diacrylate)
PDVB	polydivinylbenzene
PDE	poly[2-(dimethylamino)ethyl methacrylate-*co*-ethylene glycol dimethacrylate]
PDMMSA	poly[N,N-dimethyl-N-methacryloxyethyl-N-(3-sulfopropyl)]
PDMS	polydimethylsiloxane
PECVD	plasma enhanced chemical vapor deposition
PEG	poly(ethylene glycol)
PFDA	*1H,1H,2H,2H*-perfluorodecyl acrylate
PHEMA	poly(2'-hydroxythyl methacrylate)
P(HEMA-*co*-PFDA)	poly(2'-hydroxythyl methacrylate-*co-1H,1H,2H,2H*-perfluorodecyl acrylate)
piCVD	photo-initiated chemical vapor deposition
PPFDA	poly(*1H,1H,2H,2H*-perfluorodecyl acrylate)
PS	1,3-propanesultone
pSB	poly(sulfobetaine)
QCM-D	quartz crystal microbalance with dissipation monitoring
RO	reverse osmosis
RMS	root mean square
SA	sodium alginate
SAMs	self-assembled monolayers
sccm	standard cubic centimeters per minute
SEM	scanning electron microscope
SPR	surface plasmon resonance
TBPO	*tert*-butyl peroxide
TBO	*tert*-butoxide
TFC-HR	thin-film composite and high rejection
VASE	variable angle spectroscopic ellipsometry
V.cyclitrophicus	*Vibrio cyclitrophicus*
XPS	X-ray photoelectron spectroscopy
XRD	X-ray diffraction

CHAPTER ONE

Introduction

Reproduced with permission from Yang R., Asatekin A., Gleason K. K., *Soft Matter* **2012**, 8, 31.

1.1 Biofouling and mitigation of biofouling in seawater desalination

Fresh water scarcity affects one in three people in the world.[1] It is at the core of sustainability due to its essential role in the development of agriculture, industry and health care. In particular, energy production represents one of the largest ground water withdrawer in the US.[2] Consequently, fresh water scarcity profoundly impacts energy production. For example, in the Millstone nuclear-power plant in Connecticut one of two reactors was shut down in early August 2012 for two weeks due to the lack of cool, fresh water, which resulted in 255,000 megawatt hours of lost power production worth several million dollars.[3]

With nearly 98% of the world's available water supply being seawater or brackish water, desalination has become an important means to address the scarcity of freshwater resources. The breakthrough of seawater desalination occurred in early 1960s with the invention of reverse osmosis (RO) technology. RO membranes enable the removal of salt ions from seawater at room temperature by applying pressure to the seawater feed. In particular, thin film composite (TFC) RO membrane is considered to have the greatest water permeability with high salt rejection rate,[4] which has quickly become the dominating desalination method since its commercialization in the 1980s and is now used in nearly all RO desalination plants.[4]

RO technology has improved drastically since its invention and new designs of membrane modules and stage configurations can bring the energy consumption of a RO process close to the thermodynamic minimum energy of 1.06 kWh/m^3.[4] However, the RO technology suffers considerably from biofouling, which drives up the energy consumption, impairs water permeation and salt rejection of the highly efficient TFC-RO membranes and thus reduces freshwater yield of a desalination practice.[4,5] Biofouling — the unintended accumulation of biopolymers or whole organisms (microorganisms, plants, algae or animals) on wetted structures — represents a global problem across various maritime industries.[6] Biofouling occurs immediately when a RO process starts and has to be tolerated until the flux is reduced to 25% of the initial value.[5] It represents the bottleneck for the development of seawater desalination. Currently, marine biota and in particular bacteria are removed from the feed by pretreatment, the most energy-intensive (responsible for >36% of total plant energy consumption) and chemical-intensive step in a desalination plant and one that poses environmental risks to marine organisms when treated water is discharged back into the ocean.[4] Periodic cleaning is another standard industrial practice to reduce the adverse effects of fouling.[5] Despite its effectiveness, periodic cleaning at an average frequency of 1 day per month, interrupts the fresh water production process, reduces productivity and shortens the lifetime of the TFC RO membranes. Overall, this can lead to as much as 25% additional costs.[5] Therefore, fouling-resistant RO would bring major improvements in economic viability, energy usage, process reliability, and lower the environmental impact of seawater desalination.

Biofouling originates from surface properties of the TFC RO membranes and can be resolved by membrane surface modifications. The major challenge in the surface modification of the delicate TFC-RO membranes is to implement antifouling chemistries without compromising salt rejection and high water flux.[4] The limiting step for the transport of water and salt across the membrane is the extremely thin (~100 to 200 nm) polyamide selective layer, which is prone to damage when treated with solvents or at elevated temperature.[7] Pin-holes or defects in the polyamide layer are routes for non-selective salt transport and thus quench the salt rejection performance of the membranes. In addition, water permeability across the membrane decreases rapidly with additional layers of coating. Coating thicknesses >100 nm are undesirable because they cause >40% reduction in the water flux.[8] Therefore, an ideal surface modification method should be solvent-free, at mild temperature, and produces ultra-thin (<100 nm) antifouling coatings.

1.2 Overview of the initiated chemical vapor deposition

Most solvent-free and low temperature surface modification methods employ certain variants of chemical vapor deposition (CVD), among which parylene CVD, plasma enhanced CVD (PECVD), and initiated CVD (iCVD) are the most appropriate for the synthesis of antifouling polymer thin films (Fig. 1-1).

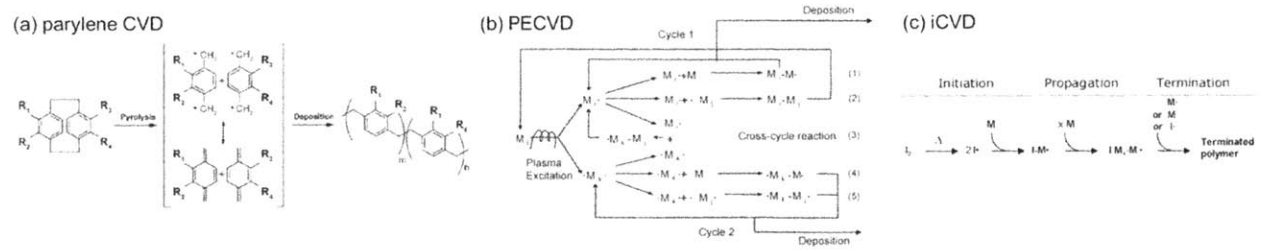

Figure 1-1 | Mechanisms of CVD techniques. In parylene CVD, substituted [2.2]paracyclophanes are pyrolyzed to prepare functionalized poly(p-xylylenes) (a). In PECVD, plasma excitation creates radical species from monomers and polymerization proceeds through various radical species (b). In iCVD, thermal energy dissociates the initiator to form radicals (c). The reaction mechanism of iCVD resembles that of a standard solution-phase free-radical polymerization.

During the synthesis of poly(*p*-xylylenes) and derivatives, substituted [2.2]paracyclophane dimer vapor is thermally cracked and self-initiates the polymerization on a cool substrate.[9-11] The application of poly(*p*-xylylenes) and derivatives features conformal coatings over high-aspect-ratio structures. The combination of topological and chemical patterning has been extensively used to immobilize biomolecules selectively. The use of functionalized poly(*p*-xylylenes) in many cases requires custom synthesis of substituted [2.2]paracyclophanes, which is economically and technically challenging to scale-up and commercialize.[10,12-14]

In PECVD, radical species are created by vapor phase plasma excitation (i.e., fragmentation of monomers), and then react and deposit on a substrate along with a wide range of molecular fragments and chemical species.[15] The retention of a specific organic functionality often increases with less plasma power, which can be achieved through pulsing plasma excitation[11] or performing the deposition downstream of an active plasma region.[11,15] Low retention of organic functional groups and poor conformality over structured surfaces are the two major drawbacks of PECVD. Despite these, PECVD has been demonstrated in industrial scale[16,17] due to a wide range of commercially available monomers that are compatible with PECVD.

To achieve better retention of organic functionalities, the activation by plasma can be replaced by radical-initiating species, namely initiator. Such initiators can be decomposed by heating (iCVD; Fig.1) to form free radicals under relatively benign conditions.[18] By avoiding the need for nonselective plasma excitation, high-rate depositions of true linear free-radical polymer chains can be achieved by iCVD with 100% functional retention.

The thermal excitation of initiator is supplied with resistively heated filaments. Substrates to be modified are placed on a cooled stage, to protect delicate substrates from the heat of the filaments, and to promote the adsorption of monomers on the surface. Proceeding from volatile monomer unites, polymer synthesis and film deposition occur simultaneously at modest vacuum. iCVD allows the facile integration of polymer coatings on virtually any substrates.[11,19] A wide range of commercially available monomers are compatible with this mild process, which gives rise to a library of functional surfaces enabled by iCVD.[20] In addition, it has been operated in a roll-to-roll manner, which is compatible with industrial infrastructures for RO membrane production.[21,22] Industrial scale iCVD reactors have been demonstrated at the GVD Corporation.

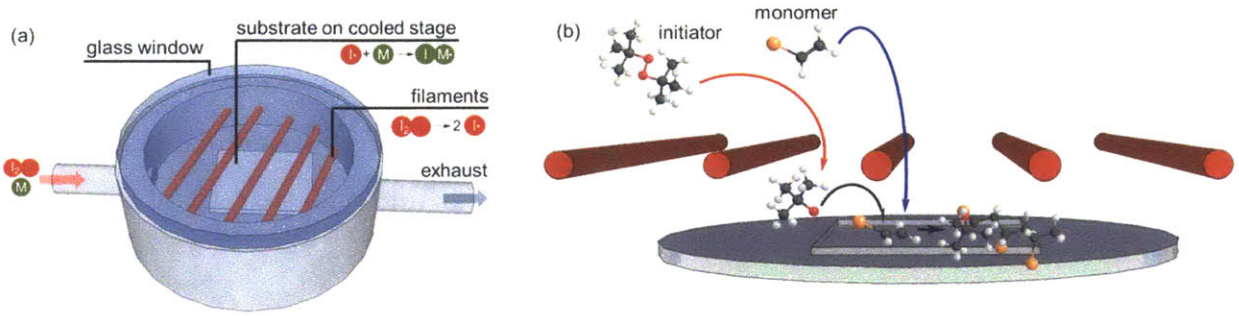

Figure 1-2 | Schematic of an iCVD reactor (a) and cross-section view of the reactor chamber interior (b). Red arrow represents the thermal decomposition reaction of initiator, *tert*-butyl peroxide in this case, and black half arrow indicates the free radical initiation of the vinyl bond in monomers. Monomer is presented in a generic formula here, with the orange ball representing a desirable organic functionality. Resistively heated filaments are indicated with red bars. Cooling lines and pumping systems are not shown in this figure.

Therefore, iCVD is selected as the appropriate surface modification technique for the integration of antifouling thin film coatings on delicate RO membranes given its benignity, versatility, scalability and compatibility with existing membrane production industry.

1.3 Antifouling coatings to control surface interactions

The development of antifouling chemistry has been an important subject of surface modification and control of surface interactions. Successful prevention of biofouling will have profound impact across all aspects of sustainability, including energy, water purification, food, and healthcare.

A variety of organic functionalities have demonstrated resistance to protein attachment.[23,24] In 2001, Whitesides *et al.* postulated the molecular characteristics of antifouling chemistry based on the screening results of approximately 60 surface functionalities afforded by self-assembled monolayers (SAMs):[25-27] (i) antifouling surfaces are hydrophilic; (ii) they contain hydrogen bond acceptor groups but not hydrogen bond donor groups; (iii) their net charge is neutral.[17,18] Among these surfaces, the ones containing derivatives of oligo(sarcosine), N-acetylpiperazine, and permethylated sorbitol groups showed protein resistance close to polyethylene glycol (PEG)-modified surfaces, which are often considered as the gold standard in protein resistance. Conformational flexibility is a non-essential characteristic of many of these groups.[28] Since this study, new materials have been developed with comparable, if not better, fouling resistance to PEG. Monolayers of chimeric peptoids (oligomers of peptide structures made of non-natural aminoacids) as one example, have shown exceptional inertness.[29,30] Ultra-low fouling has also been achieved with zwitterionic coatings synthesized via SAMs and atom-transfer radical-polymerization (ATRP).[24,31]

In general, hydrophilic surfaces, such as PEG or polyhydroxyethylmethacrylate (PHEMA), resist fouling because the enthalpic driving force for fouling (i.e., the enthalpic driving force for foulants to replace the surface-bound water molecules and adsorb to the surface) is small. Hydrogels have long been used in biomedical implants[32], tissue engineering[33], drug delivery[34] and biosensor fabrication[35] partly because of their good resistance to protein adsorption. The surface adsorption of protein on a hydrogel thin film (e.g., PHEMA) is ~250 ng cm^{-2} before removing of reversibly adsorbed foulants, which can be reduced to 2 – 25 ng cm^{-2} by prolonged washing of the fouled hydrogel films (Table 1-1). However, PEG and its derivatives are prone to degradation in long-term applications,[31] which has been attributed to oxidative degradation and enzymatic cleavage of PEG chains.[36,37]

Table 1-1 | Surface protein adsorption of different antifouling chemistries.

surface chemistry	*total protein adsorption* [ng cm^{-2}]	*irreversible protein adsorption*[ng cm^{-2}]
bare gold surface[38]*	~270	~240
hydrogel thin film coating[12,39,40]	~250	2 – 25
zwitterionic thin film coating[31,41]*	~10	< 0.3
amphiphilic coating[12,13]	~10	~1
	protein adsorption above LCST	*protein adsorption below LCST*
switchable surface[42,43]	~150 ng/cm^2	~10 ng/cm^2

*: The values were calculated from figures in the corresponding references

**: The unit of protein adsorption for hydrogel nano-structures is mg/cm^2, which is equivalent to 10^6ng/cm^2

The general molecular characteristics of antifouling surfaces describe many, but not all inert surfaces. Surfaces that simultaneously possess hydrophilic and hydrophobic properties, namely amphiphilic surfaces, have demonstrated excellent antifouling properties.[12,44,45] Compositional heterogeneities on the length scale of a foulant of interest may discourage the thermodynamically favorable interactions between foulant and surface and thus mitigate fouling. Amphiphilic materials have garnered much attention in applications on ship hulls to resist the adhesion of marine microorganisms.[13,44-46] The amphiphilic moieties usually reside on side chains of a polymer because the incorporation of comonomers with drastically different solubility is challenging. However, this can be accomplished via a solvent-free method. An amphiphilic random copolymer synthesized via iCVD has demonstrated reduced protein adsorption and bacterial adhesion.[47]

Thermo- and pH-responsive polymers that switch in hydrophilicity have also been used to impart to surfaces biofouling-release properties. Foulants can be released upon changing temperature of the underlying material that has been coated with responsive polymers.[24,48] However, such surfaces do not prevent or reduce the attachment of foulants at first, rendering them less attractive for most antifouling applications.

Within the rich library of antifouling chemistries, the primary focus of this thesis has been placed on the hydrophilic, ultra-low fouling zwitterionic materials due to their exceptional antifouling properties (Table 1-1).[31] The fouling resistance is due to the strong electrostatic hydration,[27,31,49] which is considered more effective than the hydrogen bond-induced hydration for PEG.[31] The nonspecific adsorption of proteins is not detectable by surface plasmon resonance (SPR) on carboxybetaine SAMs.[50] Furthermore, whole human blood has been used as the fouling media, and zwitterionic surfaces demonstrated very low surface adsorption.[38] Its resistance to bacterial adhesion and biofilm formation has been demonstrated by multi-hour culturing of zwitterionic surfaces in concentrated bacterial solutions.[51]

Zwitterionic coatings can be synthesized on glass or gold surfaces via SAMs,[27,31] ATRP,[31] solution polymerization and solvent evaporation.[52,53] However, these methods generally involve harsh process conditions and/or require specific surface functionalities, rendering zwitterionic chemistry not applicable to the delicate TFC RO membranes.

1.4 Scope of thesis

This thesis utilizes the enabling technology of iCVD to synthesize and apply zwitterionic, among other antifouling surface chemistries, to resolve the bottleneck of biofouling for seawater desalination. With novel designs of molecular structures and synthesis of ultrathin polymer coatings, effective and practical antifouling strategies that can benefit the desalination industry directly have been identified. Emphasis has been placed on fundamental understanding of structure-property correlations to direct the molecular design and to adapt the modified desalination membranes for long-term applications. To demonstrate the broader impact, a grafting chemistry developed for RO membranes is applied to silicon for high-efficiency hybrid solar cells. Silicon surfaces are functionalized with organic molecules via a variant of iCVD at room temperature, leading to the lowest surface recombination velocity reported to date for air-stable organic passivation.[54]

CHAPTER TWO describes the first attempt to synthesize zwitterionic surface chemistry via an all-dry method. Poly(sulfobetaine) (pSB)-based zwitterionic coatings were synthesized using iCVD and covalently grafted onto reverse osmosis (RO) membranes through a vapor phase reaction.[8] While organic solvents can damage RO membranes during the coating step,[7] this solvent-free method achieved intact membrane performance after the surface treatments. Antifouling properties of the as-fabricated zwitterionic coatings were tested with static bacterial adhesion tests. While unmodified RO membrane coupons were completely covered by

Escherichia coli at the end of the test, zwitterion-coated RO membranes exhibited no signs of adhesion.

CHAPTER THREE lends further insight into the antifouling mechanism of the iCVD zwitterionic coatings. Angle-resolved X-ray photoelectron spectroscopy (ARXPS) revealed that the diffusion-limited functionalization step led to unique film architecture – the antifouling zwitterionic moieties are highly concentrated in the top 3 nm. The fouling resistance of iCVD zwitterionic coatings was understood to a greater extent. Low absorption of various foulants including bovine serum albumin (BSA), humic acid (HA), and sodium alginate (SA), was demonstrated with the quartz crystal microbalance with dissipation monitoring (QCM-D). The first attempt to demonstrate long-term stability of the iCVD zwitterionic films was conducted. Dynamic contact angles were assessed before and after 100 days of storage in air, and unchanged contact angle values elucidated the film stability under normal storage conditions. The substrate-independent nature of this surface modification method was demonstrated by applying the iCVD zwitterionic coatings to a variety of substrates, including micro trenches cut into a silicon wafer, commercial RO membranes, and custom-fabricated electrospun nanofiber mats.

CHAPTER FOUR extended the application of the surface grafting scheme developed in chapter two to silicon surfaces. A new method of creating surface passivation on silicon by using a vapor phase treatment was demonstrated. iCVD passivation offers several advantages over previous techniques including a largely simplified reaction scheme, inexpensive reactants, mild reaction conditions, fast kinetics, and excellent long-term stability. In addition, the iCVD passivation technique allows for the fabrication of a large variety of surface functionalities with desirable surface coverage and adhesion properties on a silicon surface. The organic layer composed of 1,9-decadiene that was synthesized directly on silicon obtained the lowest surface recombination velocity reported to date (less than 10 cm s^{-1}), and remained unchanged over 200 hours of air contact.

CHAPTER FIVE introduces a novel pyridine-based zwitterionic chemistry enabled by iCVD that has superior stability to the existing zwitterionic molecular structures. The novel zwitterionic chemistry is based on a precursor copolymer film composed of 4-vinylpyridine and divinylbenzene repeat units, whose compositions are not trivial to reveal. This chapter therefore focuses on detailed chemical characterizations of this copolymer.

CHAPTER SIX reveals a very interesting observation of the synergy between low-level chlorination of the surrounding media and the surface zwitterionic chemistry to further reduce surface fouling. The new zwitterionic coatings show strong antifouling activity against marine organic compounds and bacteria. The fouling resistance of these surfaces is 100 times better than bare glass, a notable achievement in view of the fact that glass is already a rather good antifouling surface.[37] The zwitterionic coatings are transformative compared to existing antifouling materials because the pyridine molecular structure renders them stable against exposure to chlorine, the most prevalent disinfection reagent in the water industry. This led to the discovery of an unprecedented, dual-strategy antifouling scheme: coupling our chlorine-resistant surface treatment, having already superior antifouling properties, with low-level chlorination. At concentrations comparable to those in drinking water (5 ppm),[20] chlorine enhances the long-term fouling resistance of the zwitterionic coatings by almost 10 times.

CHAPTER SEVEN investigates and compares the molecular fouling of the iCVD zwitterionic and amphphiphilic antifouling coatings by molecular force spectroscopy. A reductionist approach was adopted, where the molecular interactions between AFM tips functionalized with specific organic moieties and the iCVD films are quantified.

Appendix details the visualization of nano-scale heterogeneities of the iCVD amphiphilic copolymers and sheds light on the antifouling mechanism of this unique category of antifouling materials.

References

1. WHO. *Book 10 facts about water scarcity*, <http://www.who.int/features/factfiles/water/en/> (2009).
2. Torcellini, P., Long, N. & Judkoff, R. Consumptive Water Use for U.S. Power Production. (National Renewable Energy Laboratory, Golden, Colorado 2003).
3. Smith, R. in *Wall Street Journal* (Lex Fenwick, New York, NY 10036, 2012).
4. Elimelech, M. & Phillip, W. A. *Science* **333,** 712-717, (2011).
5. Fritzmann, C., Löwenberg, J., Wintgens, T. & Melin, T. *Desalination* **216,** 1-76, (2007).
6. Callow, J. A. & Callow, M. E. *Nat Commun* **2,** 244, (2011).
7. Louie, J. S., Pinnau, I. & Reinhard, M. *J. Membr. Sci.* **367,** 249-255, (2011).
8. Yang, R., Xu, J., Ozaydin-Ince, G., Wong, S. Y. & Gleason, K. K. *Chem. Mater.* **23,** 1263-1272, (2011).
9. Tan, C., P. & Craighead, H., G. *Materials* **3,** 1803-1832, (2010).
10. Chen, H.-Y. & Lahann, J. *Langmuir* **27,** 34-48, (2011).
11. Alf, M. E. *et al. Adv. Mat.* **22,** 1993-2027, (2010).
12. Baxamusa, S. H. & Gleason, K. K. *Adv. Funct. Mat.* **19,** 3489-3496, (2009).
13. Gudipati, C. S., Finlay, J. A., Callow, J. A., Callow, M. E. & Wooley, K. L. *Langmuir* **21,** 3044-3053, (2005).
14. Krishnan, S., Weinman, C. J. & Ober, C. K. *J Mater Chem* **18,** 3405-3413, (2008).
15. Yasuda, H. *Luminous Chemical Vapor Deposition and Interface Engineering*. Vol. 122 (Marcel Dekker, New York, 2005).
16. Starostin, S. A. *et al. Appl. Phys. Lett.* **96,** 061502-061502-061503.
17. Starostine, S., Aldea, E., de Vries, H., Creatore, M. & van de Sanden, M. C. M. *Plasma Processes Polym.* **4,** S440-S444, (2007).
18. Tenhaeff, W. E. & Gleason, K. K. *Adv. Funct. Mat.* **18,** 979-992, (2008).
19. Coclite, A. M. *et al. Adv. Mat.* **25,** 5392-5423, (2013).
20. Baxamusa, S. H. I., S. G.; Gleason, K. K. *Phys. Chem. Chem. Phys.* **11,** 5227-5240, (2009).
21. Gupta, M. & Gleason, K. K. *Thin Solid Films* **515,** 1579-1584, (2006).
22. Pryce Lewis, H. G., Bansal, N. P., White, A. J. & Handy, E. S. *Thin Solid Films* **517,** 3551-3554, (2009).
23. Yang, R., Asatekin, A. & Gleason, K. K. *Soft Matter* **8,** 31-43, (2012).
24. Banerjee, I., Pangule, R. C. & Kane, R. S. *Adv. Mat.* **23,** 690-718, (2010).
25. Ostuni, E., Chapman, R. G., Holmlin, R. E., Takayama, S. & Whitesides, G. M. *Langmuir* **17,** 5605-5620, (2001).
26. Ostuni, E. *et al. Langmuir* **17,** 6336-6343, (2001).
27. Holmlin, R. E., Chen, X. X., Chapman, R. G., Takayama, S. & Whitesides, G. M. *Langmuir* **17,** 2841-2850, (2001).
28. Prime, K., L. & Whitesides, G. M. *JACS* **115,** 10714-10721, (1993).
29. Statz, A. R., Barron, A. E. & Messersmith, P. B. *Soft Matter* **4,** 131-139, (2008).
30. Statz, A. R., Meagher, R. J., Barron, A. E. & Messersmith, P. B. *JACS* **127,** 7972-7973, (2005).
31. Jiang, S. & Cao, Z. *Adv. Mat.* **22,** 920-932, (2010).
32. Yammine, P., Pavon-Djavid, G., Helary, G. & Migonney, V. *Biomacromolecules* **6,** 2630-2637, (2005).
33. Stevens, M. M. & George, J. H. *Science* **310,** 1135-1138, (2005).
34. Hsiue, G.-H., Guu, J.-A. & Cheng, C.-C. *Biomaterials* **22,** 1763-1769, (2001).
35. Gavalas, V., Berrocal, M. & Bachas, L. *Anal. Bioanal. Chem.* **384,** 65-72, (2006).
36. Konradi, R., Pidhatika, B., Mühlebach, A. & Textor, M. *Langmuir* **24,** 613-616, (2008).
37. Kerem, Z., Bao, W. & Hammel, K. E. *Proceedings of the National Academy of Sciences* **95,** 10373-10377, (1998).
38. Ladd, J., Zhang, Z., Chen, S., Hower, J. C. & Jiang, S. *Biomacromolecules* **9,** 1357-1361, (2008).

39. Lopez, G., P., Ratner, B., D., Rapoza, R., J. & Horbett, T., A. *Macromolecules* **26,** 3247-3253, (1993).
40. Johnston, E. E., Bryers, J. D. & Ratner, B. D. *Langmuir* **21,** 870-881, (2004).
41. Zhang, Z., Chen, S., Chang, Y. & Jiang, S. *J. Phys. Chem. B* **110,** 10799-10804, (2006).
42. Yu, Q. *et al. Colloids Surf., B* **76,** 468-474, (2010).
43. Cole, M. A., Voelcker, N. H., Thissen, H. & Griesser, H. J. *Biomaterials* **30,** 1827-1850, (2009).
44. Finlay, J. A. *et al. Langmuir* **24,** 503-510, (2008).
45. Krishnan, S. *et al. Langmuir* **22,** 5075-5086, (2006).
46. Gan, D. J., Mueller, A. & Wooley, K. L. *J. Polym. Sci., Part A: Polym. Chem.* **41,** 3531-3540, (2003).
47. Baxamusa, S. H. & Gleason, K. K. *Adv Funct Mater* **19,** 3489-3496, (2009).
48. Bordawekar, M., Lipscomb, G. G. & Escobar, I. *Sep. Sci. Technol.* **44,** 3369-3391, (2009).
49. Tegoulia, V. A., Rao, W., Kalambur, A. T., Rabolt, J. F. & Cooper, S. L. *Langmuir* **17,** 4396-4404, (2001).
50. Li, G. *et al. Biomaterials* **29,** 4592-4597, (2008).
51. Cheng, G. *et al. Biomaterials* **30,** 5234-5240, (2009).
52. Kitano, H. *et al. Macromol. Biosci.* **5,** 314-321, (2005).
53. Futamura, K., Matsuno, R., Konno, T., Takai, M. & Ishihara, K. *Langmuir* **24,** 10340-10344, (2008).
54. Yang, R., Buonassisi, T. & Gleason, K. K. *Advanced Materials* **25,** 2078-2083, (2013).

CHAPTER TWO

Solvent-free synthesis of zwitterionic ultrathin coatings for reverse osmosis membranes

Reproduced with permission from Yang R., Xu J., Ozaydin-Ince G., Wong S. Y. and Gleason K. K., *Chemistry of Materials* **2011**, 23, 1263.

2.1 Abstract

Poly[2-(dimethylamino)ethyl methacrylate-*co*-ethylene glycol dimethacrylate] (PDE) thin films were synthesized via initiated chemical vapor deposition (iCVD) and reacted with 1,3-propanesultone to obtain the zwitterionic structure. The crosslinker ethylene glycol dimethacrylate (EGDMA) was utilized to make the copolymer insoluble in water. The composition of the copolymer was tuned by varying the flowrates of precursors and calculated from Fourier transform infrared spectroscopy (FTIR) spectra. The zwitterionic coatings were covalently grafted on to reverse osmosis (RO) membranes and surface characterizations were carried out. Scanning electron microscope (SEM) and atomic force microscope (AFM) revealed that the iCVD zwitterionic coatings were conformal and smooth over the RO membrane and the coating thickness can be measured by using ellipsometry. Salt rejection was not impaired by the coating. Permeation tests were carried out under different feed pressures, film thicknesses and film compositions, showing a 15% to 43% reduction in permeation. Cell adhesion tests were carried out using *Escherichia coli* (*E. coli*), and the coated RO membranes showed superior antifouling performance compared with the bare RO membrane. This is the first time that the library of iCVD functional groups has been extended to charged zwitterionic moieties, and the zwitterionic coatings have been applied on delicate substrates, such as RO membranes.

2.2 Introduction

Biofouling is receiving increased attention in various applications, ranging from biomedical devices to water desalination membranes. Biofouling refers to the unintended accumulation of biopolymers or whole organisms (microorganisms, plants, algae or animals) on wetted structures, and the subsequent formation of biofilms. It is always associated with the degraded performance or decreased efficiency of a system. For example, reverse osmosis (RO) membranes are one of the most popular water purifying materials due to their high salt rejection and permeation rates as well as their excellent chemical, thermal, and mechanical stability.[1] However, fouling of RO membranes can lead to reduction in flux, salt rejection impairment, and shortened membrane lifetime.[2] This limitation is considered the bottleneck to improve the efficiency of RO technology.[3] The biofouling process can be reduced or delayed by methods such as pretreating the feed water,[4] periodic cleaning,[5] or surface modification of RO membranes.[3,6-10] However, the former two methods are costly, time consuming and periodic cleaning will shorten the membrane lifetime.[3] Surface modification such as physical adsorption and chemical bond formation are potential solutions to the biofouling problem.[6] However, the modification is no longer effective in preventing fouling once the deposition of foulants has taken place because the effect of solute/membrane interaction is reduced and replaced by solute/foulant interaction. Therefore, stable polymer architectures and surface modification strategies that impart ultralow-fouling characteristics to a surface are highly desired.

Poly(ethylene glycol) (PEG)/Oligo (ethylene glycol) (OEG) are the most widely used nonfouling materials.[11] PEG/OEG and other hydrophilic materials are less prone to biofouling due to hydration via hydrogen bonding.[12] However, their antifouling properties degrade during long-term applications. This failure has been attributed to oxidative degradation and enzymatic cleavage of PEG/OEG chains.[13] Zwitterionic-based materials can bind water molecules even more strongly than PEG/OEG chains via electrostatically induced hydration.[14,15] For this reason, zwitterionic-based materials are considered as the most promising candidates for preparation of ultra-low fouling surfaces.[16,17] Zwitterionic-materials-modified surfaces can reduce the nonspecific protein adsorption to the ultra-low level from single-protein solutions[18] and perform similarly or superiorly compared with PEG/OEG-modified surfaces in reducing plasma protein adsorption.[19,20] Furthermore, zwitterionic materials exhibit high resistance to bacterial adhesion and biofilm formation in long-term cell adhesion tests.[17,21]

Innovative techniques have been developed to synthesize zwitterionic coatings. Self-assembled monolayers (SAMs),[17] solution polymerization and solvent evaporation,[14,22] and atom transfer radical polymerization (ATRP)[18,20,23,24] are the most common (Table 2-1).

Table 2-1| Synthesis methods for the zwitterionic coatings.

method	*solvent*	*temperature / °C*	*compatibility with RO membrane substrates*	*post-treatment roughness*/ nm*
SAMs[17,25]	ethanol	25	no	~ 1 – 4
solution polymerization and solvent evaporation[14,22]	methanol, hexane or tetrahydrofuran	70	no	0.9 – 34
ATRP[26]	methanol, water	25	no	0.5 – 1.2

*: for SAMs, the roughness is estimated from the cross-section profile; for Solution Polymerization and Solvent Evaporation, the roughness is reported as average roughness, r_a; for ATRP, the roughness is reported as the root-mean-square roughness, r_q

However, these methods generally involve harsh process conditions, for instance organic solvents, which may cause damage to delicate substrates (such as RO membrane). This limits their applications to certain surfaces (gold, glass etc.). In addition, these methods may lead to high surface roughness, which is undesirable for the antifouling purpose. Poly[N,N-dimethyl-N-methacryloxyethyl-N-(3-sulfopropyl)] (PDMMSA or poly(sulfobetaine) or pSB) is one of the ultralow fouling zwitterionic polymers. Li and Jiang physically adsorbed pSB on to a gold surface covered by methy-terminated SAMs, and the surface exhibited undetectable nonspecific protein adsorption (<0.3 ng cm^{-2}) from single-protein solutions by surface plasmon resonance (SPR)-sensor measurements.[23] pSB coating can be synthesized through ATRP,[17] solution polymerization and solvent evaporation,[14,22] or incorporated into ultrafiltration membrane through water phase suspension polymerization and solution phase reaction.[9] The synthesis of zwitterionic polymers through vapor phase treatment has not yet been reported. Initiated chemical vapor deposition (iCVD) is an all-dry free-radical polymerization technique performed at low temperatures and low operating pressures,[27] which has shown great promise as a surface modification technique. It has been successfully utilized in synthesizing many distinct homopolymers,[28,29] random copolymers,[30,31] and alternating copolymers.[32] Poly(tetrafluoroethylene) has been coated on tissue paper using iCVD technique.[33] The wetting behavior was changed without affecting the bulk properties of the substrate material. Nylon fabric has been coated with poly (dimethylamino)methyl styrene with grafting chemical vapor deposition (gCVD) which is a similar process to iCVD.[34] The low substrate and filament temperatures and the solventless nature of iCVD make it an attractive polymer deposition technique on delicate substrates.

In this chapter, a copolymer containing pSB zwitterionic groups was synthesized through the initiated chemical vapor deposition (iCVD) technique and was applied onto an RO membrane for the first time. 2-(dimethylamino)ethyl methacrylate (DMAEMA) was chosen as the precursor (vapor pressure=0.45 Torr at 25 °C), which is compatible with the iCVD process. A random copolymer poly[2-(dimethylamino)ethyl methacrylate-*co*-ethylene glycol dimethacrylate] (PDE) was synthesized and deposited as a thin film in a single step. Ethylene glycol dimethacrylate (EGDMA) was chosen as the crosslinker to increase the stability of the coating. The PDE copolymer was then reacted with the 1,3-propanesultone (PS) at the solid-gas interface to convert the DMAEMA group into zwitterionic DMMSA functional group (Fig. 2-1).

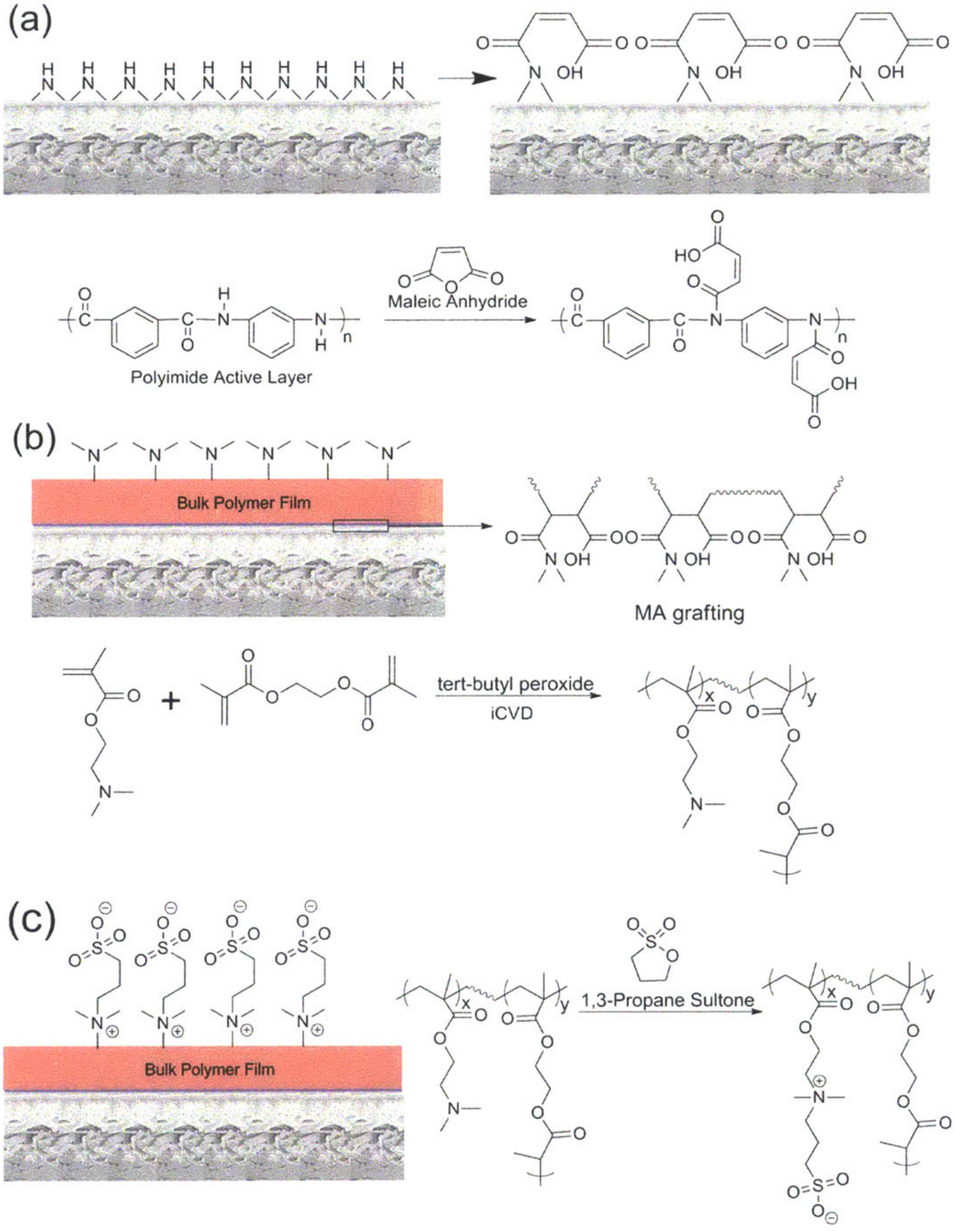

Figure 2-1| Surface modification process on RO membrane with zwitterionic films. (a) Treatment of RO membranes with MA for 20 min (b) iCVD deposition of random copolymer poly[2-(dimethylamino)ethyl methacrylate-co-ethylene glycol dimethacrylate] (c) Reaction with 1.3-propanesultone at 80 °C for 6 hours.

The zwitterionic structure was confirmed by FT-IR and XPS utilizing films deposited on silicon wafers. Coatings of identical composition were also grown directly on RO membranes. A strategy to covalently attach the polymer to RO membranes was developed to further increase the stability of the coating and adapt the coated membrane for long-term usage in water processing. Finally, surface properties of the coated RO membranes were characterized, along with their salt-rejection, permeation and antifouling performance.

2.3 Experimental Section

Film preparation and derivatization. All iCVD films were deposited in a custom built vacuum reactor (Sharon Vacuum), as previously described.[28,35] Thermal excitations of the initiator were provided by heating a 0.5 mm Nickel/Chromium filament (80% Ni/ 20% Cr, Goodfellow) mounted in a parallel array and the temperature was measured by a thermocouple attached to one of the filaments. The filament holder straddled the deposition stage which was maintained at a set point temperature using water cooling. The vertical distance between the filament and the stage was 2 cm.

All the chemicals were used as purchased without further purification. Silicon (Si) wafers (Wafer World, test grade) were coated with PDE copolymer without pre-treatment. Prior to deposition, commercial RO membranes (Sterlitech, TFC-HR) were treated with maleic anhydride (MA, Fluka, puriss $\geq$99.0%). MA was heated to 65 °C in the glass jar and the vapor was delivered into the vacuum chamber maintained at a pressure of 200 mTorr for 20 minutes. Filament temperature was kept at 200 °C to induce the MA to react with the secondary amide group in the RO barrier layer. At the end of the grafting reaction, flow of MA was stopped; the vacuum chamber was pumped out for a minimum of 1 h to remove any physisorbed MA from the surface of RO membranes.

During iCVD depositions, *tert*-butyl peroxide (TBPO, Aldrich, 97%) initiator and the nitrogen patch flow were fed to the reactor at room temperature through mass flow controllers (1479 MFC, MKS Instruments) at 1 sccm and 0.5 sccm respectively. 2-(dimethylamino)ethyl methacrylate (DMAEMA, Aldrich, 98%) and ethylene glycol dimethacrylate (EGDMA, Aldrich, 98%) monomers were heated up to 55 °C and 80 °C in glass jars, respectively and delivered into the reactor using needle valves. Systematic variation of the flow rate ratios was performed to yield high-zwitterionic-percentage, yet insoluble films of poly[2-(dimethylamino)ethyl methacrylate-co-ethylene glycol dimethacrylate] (PDE). Films were deposited at a filament temperature of 250 °C and a stage temperature of 20 °C. Total pressure in the vacuum chamber was maintained at 0.215 torr for all depositions.

In situ interferometry with a 633 nm HeNe laser source (JDS Uniphase) was used to monitor the film growth and deposit desired thicknesses on Si substrates. A more accurate film thickness on the Si wafer substrates was measured post-deposition using a J.A. Woollam M-2000 spectroscopic ellipsometry at three different incidence angles (65°, 70°, 75°) using 190 wavelengths from 315 to 718 nm. The data were fit using a Cauchy-Urbach model.

After deposition, the PDE coated substrates were fixed in a crystallizing Dish (VWR) with 1g 1,3-propanesultone (Aldrich, 98%). The crystallizing dish was placed inside a vacuum oven (Shel Lab, 1415M) which was maintained at 60 Torr, 80 °C for 6 h to let 1,3-propanesultone vapor react with the coating on substrates.

Film characterization. Fourier transform infrared (FTIR) measurements were performed on a Nicolet Nexus 870 ESP spectrometer in normal transmission mode. A deuterated triglycine sulfate (DTGS) KBr detector over the range of 400-4000 cm^{-1} was utilized with a 4 cm^{-1} resolution. Films were measured immediately after deposition and measurements were averaged over 128 scans to improve the signal-to-noise ratio. All spectra were baseline corrected by subtracting a background spectrum of the Si wafer substrate.

X-ray photoelectron spectroscopy (XPS) survey spectrum and high-resolution spectra of N_{1s} were obtained on a Kratos Axis Ultra spectrometer with a monochromatic Al Kα source. Samples were stored under vacuum overnight prior to analysis.

The thickness of the coating on the RO membrane was measured from Scanning electron microscope (SEM) images. Membranes were frozen by liquid nitrogen and broken to obtain cross-sections. 6 nm of gold (Denton Desk II) was sputter coated onto the samples and SEM images were obtained by a JEOL J5M-6700F with acceleration voltage of 10 kV.

Surface roughness characterization of the coatings was performed using atomic force microscope (AFM, Veeco, Nanoscope V with Dimension 3100). Tapping mode was employed to prevent damage to the membrane surface morphology.

Hydrophilicity of coatings and bare RO membranes was evaluated by contact angle measurements performed on a goniometer equipped with an automatic dispenser (Model 500, Ramé-Hart) using a 2 μL DI water droplet.

Permeation test. Permeation tests of the coated/bare membranes were performed using a commercial cross-flow membrane filtration unit (Sterlitech Corp., Sepa CF II) with a Hydracell Pump (M-03S) with DI water at 25 °C. The feed pressure was adjusted using a pressure control valve and a secondary metered valve. The flowrates of the feed were monitored by a vortex shedding flowmeter (FV101, Omega Engineering Inc.). The temperature of the feed was kept constant using a NESLAB chiller. The flowrates of the permeate were determined using a 100 mL metered flask. For the salt rejection calculations, a conductivity meter (CDH-152, Omega Engineering Inc.) was used.

Bacterial adhesion tests. *Escherichia coli* (*E. coli*) were used as the model microorganism. Static bacterial adhesion tests were performed following the protocol reported by Atar Adout and co-workers with minor modifications.[8] A single colony of *E. coli* was inoculated into Lysogeny broth (LB) medium and cultured overnight. The bacterial liquid was reinoculated into fresh LB medium and cultured until the logarithmic phase, centrifuged and resuspended with fresh LB medium to the concentration of 4×10^7 cells mL^{-1}. The suspension was incubated with fluorescent dye fluorescein (Sigma-Aldrich) at 20 rpm and room temperature for 2 hours. Then the bacterial liquid was centrifuged and resuspended with fresh LB medium to get rid of the excess fluorescein. Then membranes were placed into this dye-free suspension and incubated for 1 h. The membranes were then rinsed gently with a bacteria-free LB medium and observed under a fluorescent microscope (Carl Zeiss Axioskop 2 MAT).

2.4 Results and Discussion

2.4.1 Film synthesis and characterization

Homopolymers pDMAEMA, pEGDMA, and copolymer PDE films were deposited by iCVD. The deposition rate and conformality of polymers were controlled by adjusting P^m/P^{sat}, the ratio of partial pressure of the monomer and its saturated partial pressure at the temperature of the substrate during deposition. This ratio is adjusted between 0.1 and 0.7 during the iCVD process to prevent condensation of the monomer inside the reactor. High P^m/P^{sat} values usually correspond to high deposition rate and poor conformality.[27] A P^{DMAEMA}/P^{sat} of ~0.4 and a P^{EGDMA}/P^{sat} of ~0.1 were adopted in the copolymer depositions after optimization.

Prior to deposition, the RO membranes were treated with maleic anhydride (Fig. 2-1a, 2-1b); MA groups at the interface of polymer film and substrate form covalent bonds with the substrate through the reaction between the anhydride and amide functional groups in RO membrane. Without MA grafting, zwitterionic films delaminated from the membrane surface when placed in water. The monomer DMAEMA was chosen because the tertiary amine group is the precursor of zwitterionic structure; the reaction between DMAEMA in polymer and 1,3-propanesultone in various organic solvents was previously reported[9,14]. However, homopolymer pDMAEMA was soluble in water; therefore ethylene glycol dimethacrylate (EGDMA) was used as the cross-linker to prevent the coating from dissolving in water. The copolymer shown in Fig. 1b is a three-dimensional network; EGDMA groups link different polymer chains to one another. The chemical composition of copolymer was controlled by adjusting flow rates of precursors, as shown in Table 2-2. N_2 patch flow was used to keep the total flow rate constant, maintaining the same residence time for each deposition.

Table 2-2| Deposition conditions for the five iCVD coating compositions.

material	*F(DMAEMA) (sccm)*	*F(EGDMA) (sccm)*	*F(TBPO) (sccm)*	*$F(N_2)$ (sccm)*	*$mol\%_{DMAEMA}$* (%)*
pDMAEMA	3.03	0	1	1	100
Copolymer 1	3.27	0.16	1	0.5	70
Copolymer 2	3.04	0.22	1	0.7	35
Copolymer 3	1.79	0.18	1	2	15
pEGDMA	0	1.04	1	3	0

*: calculated from the FTIR analysis

The Fourier transform infrared spectroscopy (FTIR) spectra of DMAEMA monomer precursor, the as-deposited homopolymers pDMAEMA and pEGDMA, and copolymer films provide resolved features of the polymerized DMAEMA and EGDMA units. The vinyl bond in monomer precursor contributes to the sharp C=C stretching mode at 1630 cm^{-1} (Fig. 2-2a); the multiple peaks at 1299 and 1321 cm^{-1} are assigned to the conjugation structure between ester and vinyl bond[36] in the methacrylate precursor. The formation of polymer backbones with saturated carbon groups is verified by the disappearance of those C=C characteristic peaks (Fig. 2-2b to 2-2e). The double absorption at 2771 and 2822 cm^{-1} is characteristic of the tertiary amine structure in DMAEMA unit; this absorption is absent from quaternary amine spectra. The peak at 1721 cm^{-1}, which is characteristic of the carbonyl in carboxylic acid groups, was used along with the peak at 2771 cm^{-1} to calculate the content of DMAEMA unit in the copolymers (Fig. 2-2c and 2-2d).

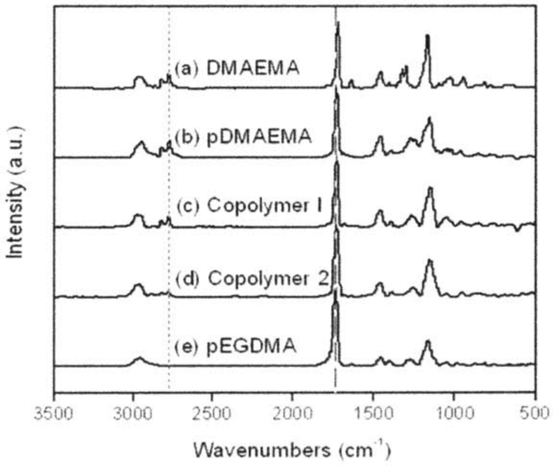

Figure 2-2| Fourier transform infrared spectroscopy (FTIR) spectra of (a) DMAEMA monomer, (b) iCVD deposited homopolymer of pDMAEMA, (c) copolymer with a pDMAEMA content of ~70%, (d) copolymer with a pDMAEMA content of ~35%, and (e) homopolymer of pEGDMA. Dot line indicates the characteristic of tertiary amine group and dash line indicates characteristic of the carbonyl in carboxylic acid groups.

According to the Beer-Lambert equation,[36] the absorbance of a mode is proportional to the concentration of the moiety that is responsible for that particular mode, assuming that the bond oscillator strength is the same for each film. According to this equation, the areas under 2771 cm^{-1} and 1721 cm^{-1} are proportional to the concentration of tertiary amine and carbonyl groups respectively in the copolymers. Assuming these copolymers follow Beer-Lambert equation, the chemical compositions can be calculated. In homopolymer pDMAEMA, the ratio of the carbonyl peak area to the amine peak area is 8.42 (denoted as r in Eq. 2-1). Using this ratio, the corresponding carbonyl intensity contributed by DMAEMA units can be obtained from the amine peak area, A_{amine}. Taking into account the two carbonyl bonds per EGDMA unit, the ratio of EGDMA units to DMAEMA units in a copolymer can be calculate as,

$$\frac{[\text{EGDA}]}{[\text{DMAEMA}]} = \frac{(A_{\text{C=O}} - r \cdot A_{\text{amine}})/2}{r \cdot A_{\text{amine}}} \tag{2-1}$$

This method has previously been reported to calculate the composition of p(2-hydroxyethyl methacrylate-*co*-ethylene glycol dimethacrylate).[37] The calculated compositions (Table 2-2) were confirmed by XPS results (not shown here).

Reaction with 1,3-propanesultone was carried out following the synthesis of films. As shown in Fig. 1c, the tertiary amine in DMAEMA was converted to a quaternary amine inner salt by reacting with 1,3-propanesultone vapor at 80 °C for 6 h. The FTIR spectrum (Fig. 2-3a) confirms that the zwitterionic structure is obtained. The 1036 cm^{-1} adsorption is ascribed to the symmetric stretch vibration of the SO_3^- group[36] and the characteristic peak of tertiary amine (2771 cm^{-1}) is undetectable after the reaction, indicating the formation of quaternary amine. This charged zwitterionic structure is also confirmed by the XPS nitrogen (1s) high resolution scan (Fig. 2-3b and 2-3c). The peak around 398.8 eV corresponds to the quaternary amine (reaction product) in the sulfobetaine unit while the 396.5 eV peak is assigned to tertiary amine in DMAEMA unit (reactant). Before the reaction, the tertiary amine peak is dominant and the small amount of quaternary amine is attributed to the post-treatment adsorption of atmospheric CO_2,[38] which takes place in milliseconds and is inevitable. The occurrence of the reaction is indicated by the reduction of tertiary peak and the increased intensity of quaternary amine.

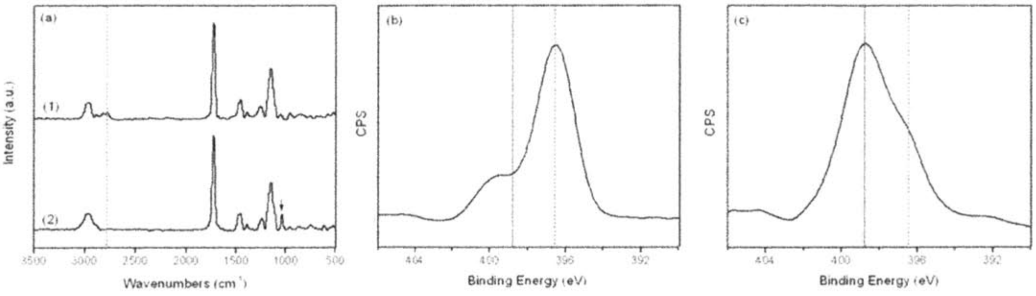

Figure 2-3| Confirmation of the sulfobetaine repeat units. (a) the FT-IR spectra of copolymer 2 films (1) before reaction and (2) after reaction; the arrow indicates the characteristic peak of the SO_3^- group and the dash line represents for the tertiary amine peak, which does not appear in quaternary amine, (b) the XPS nitrogen high resolution scan before reaction and (c) after reaction with 1,3-propanesultone.

Both FTIR and XPS data confirmed the hypothesis that iCVD produced the zwitterionic copolymer poly[N,N-dimethyl-N-methacryloxyethyl-N-(3-sulfopropyl)-*co*-ethylene glycol dimethacrylate], which contains the sulfobetaine repeat units.

2.4.2 Characterization of surface-coated RO membranes

Commercial reverse osmosis (RO) membranes were coated with PDE (with 15% or 35% DMAEMA content in the PDE copolymer) and reacted with 1,3-propanesultone to form a zwitterionic copolymer layer on RO barrier layer. The SEM images before and after the surface modification shown in Fig. 2-4 confirm this.

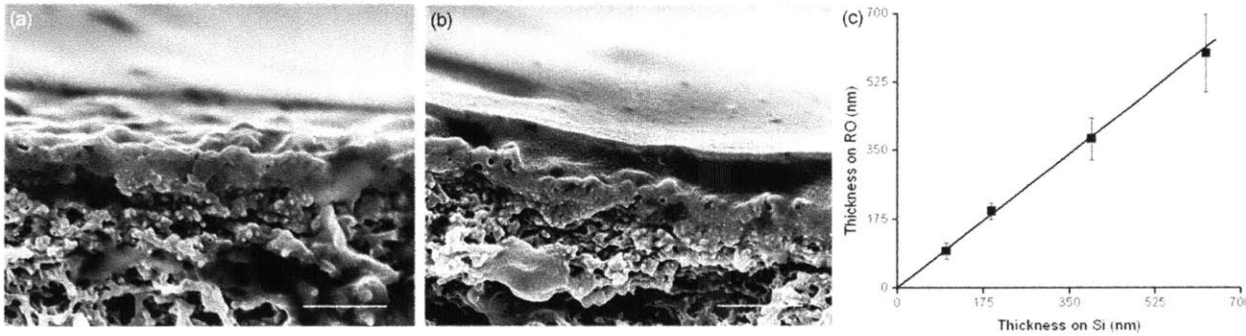

Figure 2-4| SEM images of cross-sections of bare and modified RO membranes. For bare RO membrane (a), polysulfone layer and polyamide barrier layer (i.e., the non-porous top layer) were shown in the image. After iCVD deposition, it is very clear that a smooth and conformal coating with the thickness of 600 nm formed on top of the polyamide. (c) the correlation between the film thickness on Si measured by ellipsometer and film thickness on RO membrane measure by SEM images. The scale bars indicate 1 μm.

A high surface roughness was observed on the bare RO membrane cross-sectional SEM image. This was due to the mechanical stretching and tearing during the freeze fracture breaking of RO membrane, which has been reported by Ferlita and co-workers.[39] iCVD was *controlled in situ* with an interferometer monitoring the film thickness on the Si wafer, which was measured more precisely afterwards with a variable angle spectroscopic ellipsometer. To check that the thickness of the coating on the Si wafer is representative of the thickness on the RO membrane, additional cross-sectional SEM measurements were performed on separate samples. Four PDE coatings (with the thickness of ~100, 200, 400 and 600 nm respectively) were deposited on Si wafers and RO membranes by iCVD. For each coating, 10 SEM images were taken and the average thickness was calculated. The relationship between the thicknesses on Si and the four SEM averages were plotted and shown in Fig. 2-4c. There is a clear linear relation, and the slope of linear fitting is 0.97 (nm on RO/ nm on Si) with an intercept of 1.91 (nm on RO). Therefore, the film thickness on Si is comparable to the film thickness on the RO membrane and will be used to estimate the film thickness on RO membrane.

In the permeation process of coated RO, water molecules have to diffuse through the coating layer in addition to the barrier layer; therefore the coating thickness needs to be optimized for high water throughput and shear strength. The film thickness also affects the morphology of the RO membrane surface and consequently the antifouling property of the surface. A surface with micron scale roughness may induce an uneven flow distribution or channeling, thus acting as physical barriers and entrapping bacteria.[40] The uneven flow distribution may also impair the throughput and lifetime of the membrane. Irregularities within tens of nanometers would provide "shield" to attached proteins from shear forces by disturbing static boundary layer. The probability of membrane fouling increases with the surface roughness also because rough surfaces have larger surface areas and more binding sites for foulants to attach. Furthermore, the formation of defects such as pinholes increases with surface roughness, which will accelerate the formation of the biofilm.

Due to the conformal nature of the iCVD process,[29,41,42] thin iCVD coatings have little effect on the surface roughness of RO membranes according to the AFM characterization of the iCVD coating on RO membranes. As shown in Fig. 2-5, compared to the surface roughness of bare RO membranes (~0.3 ± 0.02 nm root mean square (RMS) roughness), thin coatings (~30 nm) with 35% sulfobetaine increased the roughness to 0.9 ± 0.1 nm RMS roughness, and thick coatings (~100 nm) with the same composition increases the surface roughness to 2.8 ± 0.2 nm RMS roughness. The increase in roughness is due to the instability on the surface, which increases with the film thickness. However, the iCVD coated surface remains relatively smooth (<3 nm RMS roughness). It is worth noting that at this low surface roughness, morphological effects on measured contact angles are minimal and thus the contact angle data will primarily reflect the surface energy of the film.

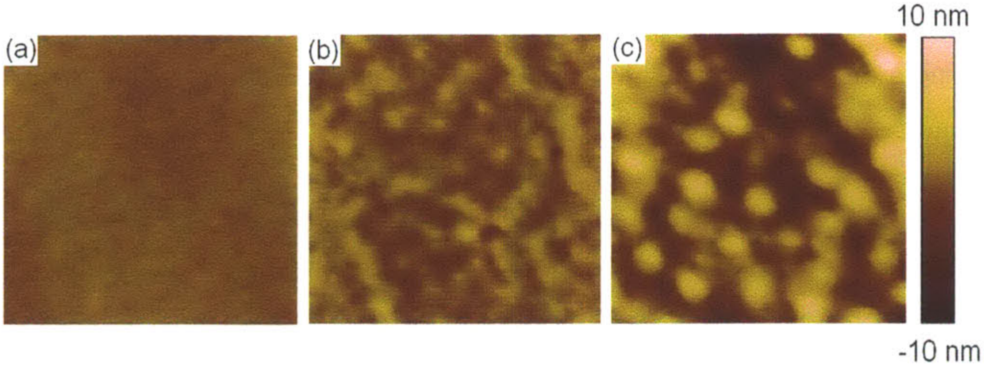

Figure 2-5| AFM images of membranes. As the thickness increases the surface roughness increases. The RMS roughness values for bare RO membrane (a), membrane modified with 30-nm iCVD coating (b), and membrane modified with 100-nm iCVD coating (c) are 0.3, 0.9 and 2.8 nm respectively.

Therefore, in order to minimize the surface roughness and maximize the throughput of coated membrane, thick coatings need to be prevented; therefore a thickness of 30 nm was adopted as a compromise between the membrane performance and stability. The later will be discussed in the next section.

Because of its effects on permeate throughput, hydrophilicity is another very important criterion for evaluating surface modification of membranes used in water processing. Static contact angles were analyzed to evaluate the surface hydrophilicity in this work. Measurements before and after the reaction with 1,3-propanesultone with the film on Si are 48.3 ± 1.0 degrees and 33.9 ± 0.9 degrees (for polymer 2, Table 2-3), respectively which demonstrates the strong hydration via ionic salvation of zwitterionic units. For RO membranes, the contact angles before and after the modification with polymer 2, are 41.9 ± 1.5 degrees and 33.3 ± 0.9 degrees respectively (Table 2-3). With decreased zwitterions and increased cross-linker content in the film (polymer 3), the contact angle becomes 60.7 ± 0.7 degrees. Therefore, it is clear that sulfobetaine units are the reason for increased hydrophilicity after modification.

Table 2-3| Static contact angles of coated/bare RO membranes before/after water soaking.

material	*contact angle before soaking*	*contact angle after soaking*
bare RO	41.9 ± 1.5	48.7 ± 1.3
copolymer 2	33.3 ± 0.9	40.5 ± 1.0
copolymer 3-grafted	60.7 ± 0.7	68.2 ± 0.6
copolymer 3-non-grafted	61.3 ± 1.0	49.4 ± 1.7

2.4.3 Stability of the iCVD zwitterionic thin films

In commercial or industrial operations, RO membranes are used for prolonged periods in order to cut the cost. With proper pretreatment and cleaning, commercial RO membranes can last for up to 2 years.[43] In order to reduce fouling and protect the membrane, the antifouling coating has to be mechanically strong and adhesive to the RO membrane.

Covalent bonding of PDE to the RO membrane through MA grafting was required for stability in long-term usage. The grafting process is shown in Fig. 2-1a. The anhydride moiety in MA reacted with the secondary amide group on the RO surface and the MA vinyl bonds polymerized with DMAEMA and EGDMA to covalently bond the PDE coating to the substrate. In order to test the stability of the grafting method, iCVD coated membranes with and without MA treatment were put in DI water for 24 hours. Contact angles before and after the soaking (Table 2-3) were used to indicate the condition of the iCVD coating. The coating composition of copolymer 3 was used because the difference between bare and coated membrane contact angles is largest for this composition. For the bare RO membrane and grafted iCVD coating, the contact angles increased by ~7 degrees after soaking, while for the non-grafted coating, the contact angle dropped to 49.4 ± 1.7 degrees, which is comparable to the bare RO membrane surface (48.7 ± 1.3). This drastic decrease in contact angle indicates the detachment of coating from the RO membrane during the soaking. Wrinkles on soaked membranes were observed with AFM; this increase in surface roughness explains the ~7 degrees of change of contact angles for bare RO membrane and grafted iCVD coating.

2.4.4 Permeation tests

Permeation tests were performed with the bare RO membranes and RO membranes coated with different thicknesses and different compositions of iCVD coatings. The thickness of 30 nm and the composition of 35% sulfobetaine were adopted in the salt rejection tests.

Two pressures were used in the permeation tests in order to study the effect of hydrophilicity of the surface. Fig. 2-6a and 2-6b are operated under 80 psi, while Fig. 2-6c and 2-6d were operated under 300 psi.

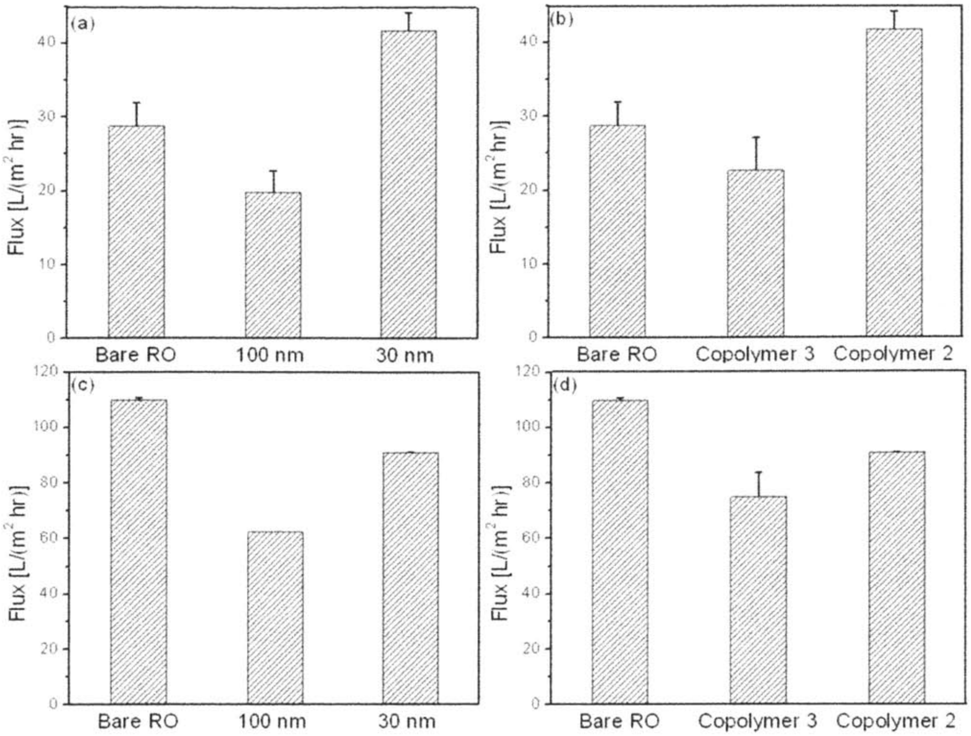

Figure 2-6| Flux of DI water across bare and modified RO membranes. Permeation rates are measured with DI water at the pressure of 80 psi through bare RO membranes and the coated membranes of different thicknesses with the pSB content of ~35% (a), different compositions with the thickness of 30 nm (b) and at the pressure of 300 psi through bare membranes and ones modified with iCVD polymers (35% pSB) with different thicknesses (c), and with different compositions with the thickness of 30 nm (d).

The permeation of water through an RO membrane consists of several steps. First, water molecules are adsorbed onto the membrane surface, and then these molecules will diffuse through the coating layer and barrier layer, and become permeate. The adsorption step is slower under low pressure than that under high pressure; therefore the hydrophilicity of the surface plays a more important role in determining the permeation rate under low pressure. In Fig. 2-6a, the composition of coating is 35% pSB. When the thickness was 30 nm, the permeation rate of the coated RO membranes became higher than the bare membrane due to the more hydrophilic surface after surface modification. However, with the film thickness of 100 nm, the diffusion through membrane became rate-limiting, and therefore the thicker coating induced slower permeation rate than bare RO membrane. Furthermore, when the composition of 15% sulfobetaine was adopted, the surface hydrophilicity was less than bare RO, and a lower permeation flux was observed (Fig. 2-6b).

Under high pressure (300 psi), the diffusion step becomes the slow step; therefore coated membranes have lower permeation flux compared to bare RO membranes. With the increase of film thickness from 30 nm to 100 nm, the flux was further reduced from 91.1 L h^{-1} m^{-2} to 62.3 L h^{-1} m^{-2} compared to the 109.8 L h^{-1} m^{-2} of bare RO membranes (Fig. 2-6c). The flux can be increased by further decreasing the coating thickness. Increasing the surface hydrophilicity can also increase the permeation of coated membrane. The flux increased from 75.0 L h^{-1} m^{-2} to 91.1 L h^{-1} m^{-2} when the chemical composition of the coating was changed from 15% sulfobetaine to 35% sulfobetaine.

Salt rejection of the bare and coated membranes were measured by monitoring the conductivity of the permeate using a conductivity meter. The measurements were recorded every 2 minutes for 4 hours. 2000 ppm NaCl solution was used as the feed, and the tests were operated under 300 psi. The overall salt rejection of the bare RO membrane is around 97%. Fig. 2-7 shows the salt rejection percentages for bare and coated membranes at the end of 4 hours. The minor decrease in salt rejection (~2%) after coating is within the experiment error.

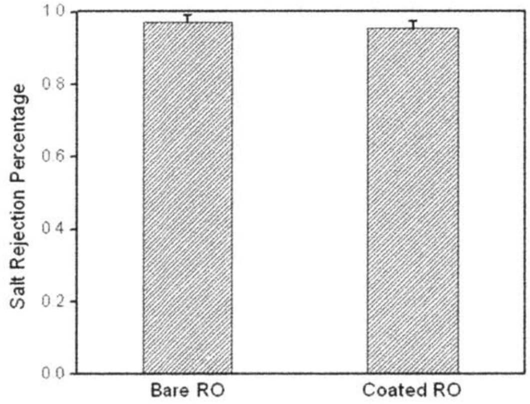

Figure 2-7| Salt rejection percentages of the bare and coated RO membranes. The coating chemistry has no effect on the salt rejection of the membranes.

2.4.5 Cell adhesion tests

The antifouling capability of the zwitterionic surface modification was tested with *E. coli*. The attachment and settlement of bacteria is the key step in the formation of biofilm, and *E. coli* is a gram negative bacterium which is widely used in membrane antifouling studies.[8,44,45] In this work, the static adhesion of *E. coli* cells onto the zwitterionic films was studied and compared with bare RO membrane.

The membrane coupons were incubated with concentrated *E. coli* bacteria culture for 1 hour, and then observed under fluorescent microscope. It should be pointed out that in order to prevent the fluorescent dye from diffusing into the films and the consequent "false-positive" phenomenon, the bacteria were centrifuged and washed thoroughly with fresh LB medium before the static adhesion tests.

The representative fluorescence microscopy images showing *E. coli* attachment to the coated/uncoated RO membranes are shown in Fig. 2-8. On the bare RO membrane surface, significant bacterial adhesion and formation of a confluent biofilm of *E. coli* were observed at the end of the 1 hour incubation. However, no such film formed on the zwitterion-coated RO membrane. It has further been shown by Li and coworkers that after 3-day flowing adhesion experiments, polysulfobetaine SAM surface reduced 99.6% of the adhesion of bacteria compared to that on bare glass surfaces.[17] In future work, rigorous testing will be performed to quantify this antifouling behavior.

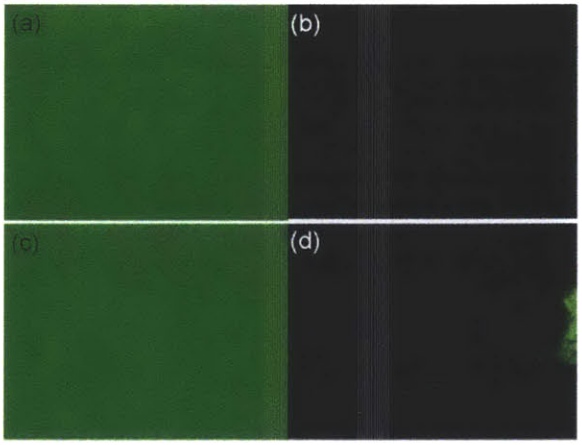

Figure 2-8| Bacterial attachment on bare and modified RO membranes. Fluorescence micrographs are taken after the incubation with concentrated *E. coli* culture for bare RO membrane (a and c), iCVD coated RO membrane (b), and iCVD coated RO membrane with scratch (d), exhibiting the contrast between the antifouling capabilities of coated/uncoated membranes.

The antifouling property of zwitterionic materials in inhibiting the formation of biofilm is attributed to the electrostatically induced strong hydration. The excellent ability of pSBMA to reduce protein adsorption as well as bacteria adhesion has been shown before. This work provides a technique for grafting a stable, defects-free thin layer of zwitterionic polymer onto delicate substrates, and rendering them the ultralow fouling properties for various applications.

2.5 Conclusion

Antifouling, surface-attached zwitterionic ultra-thin (30 to 100 nm) films were synthesized using initiated chemical vapor deposition (iCVD) for the first time. The zwitterionic moiety in the iCVD film was confirmed by FTIR and XPS results. The content of zwitterionic units in the copolymer was controlled precisely in the iCVD process.

The motivation to use the iCVD synthesis process was demonstrated by depositing iCVD zwitterionic thin films on commercial RO membranes, where traditional solution-phase modifications were not favored because of the harsh conditions involved. The capabilities of the all-dry iCVD process in the surface modification of delicate substrates were demonstrated. The iCVD zwitterionic coating on RO membrane is highly smooth as confirmed by AFM measurements. The coating thickness on an RO membrane was shown to be comparable to the film thickness on Si and can be controlled *in situ*. However, increasing the thickness of the coatings increases the surface roughness and decreases the permeation rates. For a 30 nm coating with the composition of 35% sulfobetaine, the permeation flux was reduced by ~15% compared to bare RO membranes. It is possible to further decrease the coating thickness and obtain higher flux. The coating left the salt rejection of the membrane intact. Furthermore, cross-linker in the copolymer and MA grafting improved the coating stability compared with non-grafting coatings. The enhancement in antifouling performance was exhibited by the static cell adhesion tests with *E. coli*. The attachment of bacteria is readily prevented by coating the membranes with iCVD zwitterionic thin film.

Combining the high stability and the significant antifouling performance, this surface-tethered antifouling zwitterionic thin film made the prolonged usage of RO membranes possible. Future work will investigate techniques to optimize membrane permeability and extensively characterize the antifouling performance of the membrane.

ACKNOWLEDGMENT. The authors would like to thank the King Fahd University of Petroleum and Minerals in Dhahran, Saudi Arabia, for funding the research reported in this paper through the Center for Clean Water and Clean Energy at MIT and KFUPM. We thank Jonathan Shu from Cornell Center for Materials Research (CCMR) for his help with XPS measurements.

References

1. Shannon, M. A. B., P. W.; Elimelech, M.; Georgiadis, G. J.; Marinas, B. J.; Mayes, A. M. *Nature* **452,** 301-310, (2008).
2. Herzberg, M. E., M. *Journal of Membrane Science* **295,** 11-20, (2007).
3. Lin, N. H. K., M.; Lewis, G. T.; Cohen Y. *Journal of Materials Chemistry* **20,** 4642-4652, (2010).
4. Griebe, T. F., H. C. *Desalination* **118,** 153-156, (1998).
5. Qin, J.-J. L., B.; Kekre, K. A. *Open Chemical Engineering Journal* **3,** 8-16, (2009).
6. Wei, X. W., Z.; Zhang, Z.; Wang, J.; Wang, S. *Journal of Membrane Science* **351,** 222-233, (2010).
7. Freger, V. G., J.; Belfer, S. *Journal of Membrane Science* **209,** 283-292, (2002).
8. Adout, A. K., S.; Asatekin, S.; Mayes, A. M.; Elimelech. M. *Environmental Science & Technology* **44,** 2406-2411, (2010).
9. Sun, Q. S., Y.; Ma, X.; Wang, Y.; Jiang, Z. *Journal of Membrane Science* **285,** 299-305, (2006).
10. Kang, G. L., M.; Lin, B.; Cao, Y.; Yuan Q. *Polymer* **48,** 1165-1170, (2007).
11. Harris, J. M. *Poly(Ethylene Glycol) Chemistry: Biotechnical and Biomedical Applications.* (Plenum Press, New York, 1992).
12. Tu, S.-C. R., V.; Den, W.; Pirbazari, M. *AIChE Journal* **47,** 1346-1362, (2001).
13. Krishnan, S. W., C. J.; Ober, C. K. *Journal of Materials Chemistry* **18,** 3405-3413, (2008).
14. Kitano, H. M., T.; Takeuchi, Y.; Tada, S.; Gemmei-Ide, M.; Yokoyama, Y.; Tanaka, M. *Macromolecular Bioscience* **5,** 314-321, (2005).
15. Futamura, K. M., R.; Konno, T.; Takai, M.; Ishihara K. *Langmuir* **24,** 10340-10344, (2008).
16. Jiang, S. C., Z. *Advanced Materials* **22,** 920-932, (2010).
17. Li, G. C., G.; Xue, H.; Chen, S.; Zhang, F.; Jiang, S. *Biomaterials* **29,** 4592-4597, (2008).
18. Zhang, Z. C., S.; Chang, Y.; Jiang, S. *Journal of Physical Chemistry B* **110,** 10799-10804, (2006).
19. Chang, Y. L., S.-C.; Higuchi, A.; Ruaan, R.-C.; Chu, C.-W.; Chen, W.-Y. *Langmuir* **24,** 5453-5458, (2008).
20. Ladd, J. Z., Z.; Chen, S.; Hower, J. C.; Jiang S. *Biomacromolecules* **9,** 1357-1361, (2008).
21. Cheng, G. L., G.; Xue, H.; Chen, S.; Bryers, J. D.; Jiang S. *Biomaterials* **30,** 5234-5240, (2009).
22. Zhang, S. F. R., P.; Wright, G.; Lian, W.; Milling, A. J.; Tanaka, S.; Ishihara, K. *Biomaterials* **19,** 691-700, (1998).
23. Chang, Y. C., S.; Zhang, Z.; Jiang, S. *Langmuir* **22**, (2006).
24. Rodriguez Emmenegger, C. B., E.; Riedel, T.; Sedlakova, Z.; Houska, M.; Bologna Alles, A. *Langmuir* **25,** 6328-6333, (2009).
25. Wang, H., Chen, S., Li, L. and Jiang, S. *Langmuir* **21,** 2633-2636, (2005).
26. Cheng, N. B., A. A.; Azzaroni, O.; Huck, W. T. S. *Macromolecules* **41,** 6317-6321, (2008).
27. Baxamusa, S. H. I., S. G.; Gleason, K. K. *Physical Chemistry Chemical Physics* **11,** 5227-5240, (2009).
28. Martin, T. P. K., S. E.; Chang, S. H.; Sedransk, K. L.; Gleason, K. K. *Biomaterials* **28,** 909-915, (2007).
29. Xu, J. G., K. K. *Chemistry of Materials* **22,** 1732-1738, (2010).
30. Baxamusa, S. H. G., K. K. *Advanced Functional Materials* **19,** 3489-3496, (2009).
31. Tenhaeff, W. E. G., K. K. *Chemistry of Materials* **21,** 4323-4331, (2009).
32. Tenhaeff, W. E. G., K. K. *Langmuir* **23,** 6624-6630, (2007).
33. Martin, T. P. L., K. K. S.; Chan, K.; Mao, Y.; Gupta, M.; O'Shaughnessy, W. S.; Gleason, K. K. *Surface and Coatings Technology* **201,** 9400-9405, (2007).
34. Martin, T. P. S., K. L.; Chan, K.; Baxamusa, S. H.;Gleason, K. K. . *Macromolecules* **40,** 4586-4591, (2007).
35. Ozaydin-Ince, G. G., K. K. *Journal of Vacuum Science and Technology A* **27,** 1135-1143, (2009).
36. Lin- Vien, D. C., N. B.; Fateley, W. G.; Grasselli, J. G. *The Handbook of Infrared and Raman Characteristic Frequencies of Organic Molecules.* (Academic Press, New York, 1991).

37. Chan, K. G., K. K. *Langmuir* **21,** 8930-8938, (2005).
38. Spanos, C. G. B., J. P. S.; Goodwin, A. J.; Merlin, P. J. *Polymer* **46,** 8908-8912, (2005).
39. Ferlita, R. R. P., D.; Safarik, J.; Yeh, D. H. *Environmental Progress* **27,** 204-209, (2008).
40. Ghayeni, S. B. S. B., P. J.; Schneider, R. P.; Fane, A. G. *Journal of Membrane Science* **138,** 29-42, (1998).
41. Baxamusa, S. H. G., K. K. *Thin Solid Films* **517,** 3536-3538, (2009).
42. Lau, K. K. S. G., K. K. *Advanced Materials* **18,** 1972-1977, (2006).
43. Into, M. J., A.-S.; Lengden, G. *Journal of Membrane Science* **242,** 21-25, (2003).
44. Kim, S. H. K., S.-Y; Sohn, B.; Park, T. H. *Journal of Membrane Science* **211,** 157-165, (2003).
45. Tan, K. O., S. K. *Journal of Membrane Science* **305,** 287-298, (2007).

CHAPTER THREE

Enhanced fouling resistance via surface-concentrated zwitterionic moieties

Reproduced with permission from Yang R. and Gleason K. K., *Langmuir* **2012**, 28, 12266.

3.1 Abstract

Antifouling thin films of poly[N,N-dimethyl-N-methacryloxyethyl-N-(3-sulfopropyl)-*co*-2-(dimethylamino)ethyl methacrylate-*co*-ethylene glycol dimethacrylate] (PDDE) were synthesized via a substrate-independent, all-dry initiated Chemical Vapor Deposition (iCVD) technique followed by a diffusion-limited vapor phase reaction with 1,3-propane sultone. Coated surfaces exhibited very low absorption of various foulants including bovine serum albumin (BSA), humic acid (HA) and sodium alginate (SA), as measured by quartz crystal microbalance measurements with dissipation monitoring (QCM-D). The fouling by humic acid was dependent on the presence of divalent cations such as Ca^{2+}. Both depth profiling and angle-resolved X-ray photoelectron spectroscopy (XPS) measurements indicated that the zwitterionic groups were highly concentrated in the top ~3 nm of the film. The contact angle measurements revealed a limited degree of surface chain reorganization upon contacting water. The dynamic contact angles remained unchanged after 100 days of storage in air, indicating the stability of the interface. The coating was substrate-independent, and the film was conformal on surface nanostructures including trenches, reverse osmosis membranes and electrospun nanofiber mats.

3.2 Introduction

Reducing protein adsorption to surfaces has been a significant challenge due to its crucial role in many applications including biosensors, medical implants and equipment, water purification systems, marine and industrial equipment.[1,2] Innovative techniques have been applied to synthesize surfaces that strongly resist protein adsorption and cell adhesion, termed "inert" surfaces. Among them, zwitterionic surfaces synthesized via self-assembled monolayer (SAMs) and atom transfer radical polymerization (ATRP) exhibit ultralow adsorption of protein and bacteria.[3,4] Zwitterionic surfaces are of great interest in various antifouling applications due to their comparable inertness relative to polyethylene glycol (PEG)/polyethylene oxide (PEO), and better stability.[5]

With the rapid development of zwitterionic surfaces, comes the challenge of applying such functionalities to a much wider range of substrates and fabricating more sophisticated surface structures with these materials. SAMs with zwitterionic moieties can only be applied to gold substrates with limited coating thickness.[3] Zwitterionic brushes generated by "graft-from" or "graft-to" methods require certain surface functional groups, which are not possessed (or could not be possessed through pretreatment) by all substrates.[4,6] Polyelectrolyte multilayer films containing zwitterionic moieties that resist the adhesion from proteins and cells have been fabricated via layer-by-layer (LbL) assembly on glass surfaces.[7,8] More rapid assembly via spray LbL has been demonstrated for several compositions, but not zwitterionic films specifically.[9,10] However, the conformality of the sprayed films on non-planar substrates is variable and requires forced convection through a porous substrate. The gas flow required to achieve conformality with spray LbL is not possible for liquid- or gas-impermeable substrates.[11] Many attempts have been made to synthesize zwitterionic copolymer films via bulk solution polymerization and solvent evaporation, [12-15] where cross-linker is needed to prevent the films from dissolving in water. Under dry conditions, however, as-synthesized copolymers provide only low concentrations of zwitterionic surface moieties as the hydrophilic zwitterions tend to bury themselves under the hydrophobic chains in the cross-linkers. This process is favored to minimize the interfacial free energy under dry conditions.[12,13,16] This effect diminishes the antifouling performance because the fouling resistance is directly related to the surface density of zwitterions for both ATRP brushes and polymer thin films.[17,18] Prolonged wetting pretreatment induces surface group reorientation and increases the surface density of zwitterions. However, the restricted rate of steric rearrangement in a solid thin film makes the process very time-consuming.[14] The treated surface still undergoes surface rearrangement and becomes hydrophobic again if it is stored in air.[13] Naphthalene side groups have been added to the copolymer to restrict the chain mobility in hopes of sterically trapping the zwitterionic groups on the surface.[16] However, the required polymerization time increased by 4 folds due to the large steric hindrance. In addition, very specific molecular structures are required to reduce the chain mobility to an extent that no surface rearrangement occurs. This requirement limits the viable copolymer chemistries, restricts potential physical properties, and eliminates the possibility of multi-functional design.

We recently reported the first synthesis of zwitterionic thin film via iCVD. iCVD is a vacuum-based, vapor phase technique for the facile integration of polymer coating on virtually any substrates. Proceeding from volatile monomer unites, polymer synthesis and film deposition occur simultaneously at modest vacuum and low temperature. This all-dry process enabled the application of zwitterionic thin film directly onto delicate substrate such as reverse osmosis (RO) membranes.[19] Here, we first demonstrate that the diffusion limitation of the gas phase reaction is critical to obtain high surface zwitterionic concentration. This is elucidated by the ARXPS of the as-fabricated coatings. Contrary to most bulk solution phase polymerization and solvent evaporation methods, this reaction scheme results in the highest concentration of zwitterionic moieties on the top surface, which is desirable for antifouling applications. Compared with the chain-mobility-constraining (CMC) method, [16] where the polymerization time was 46 hours at 60°C, high surface densities of zwitterionic antifouling groups are achieved with only 1/8 the fabrication time of the CMC method. We also proved that the undesirable changes in surface energy over time can be reduced or prevented by crosslinking the bulk film. Finally, the zwitterionic coatings fabricated via this two-step scheme are inert and resist the adsorption of various foulants. The surface adsorption was quantified using quartz crystal microbalance measurements with dissipation monitoring (QCM-D) and modeled with Sauerbrey equation.

3.3 Experimental Section

Film preparation and derivatization. All initiated chemical vapor deposition (iCVD) films were deposited in a custom built vacuum reactor (Sharon Vacuum), as previously described.[20,21] Thermal excitations of the initiator were provided by heating a 0.5 mm Nickel/Chromium filament (80% Ni/ 20% Cr, Goodfellow) mounted in a parallel array and the temperature was measured by a thermocouple attached to one of the filaments. The filament holder straddled the deposition stage which was maintained at a set point temperature using water cooling. The vertical distance between the filament and the stage was 2 cm.

All the chemicals were used as purchased without further purification. Depositions were performed on several substrates including 100 mm diameter silicon wafers (Wafer World), trench wafers, electrospun nanofiber mats and Koch TFC-HR reverse osmosis membrane. During iCVD depositions, *tert*-butyl peroxide (TBPO, Aldrich, 97%) initiator and the nitrogen patch flow were fed to the reactor at room temperature through mass flow controllers (1479 MFC, MKS Instruments) at 0.5 sccm and 1 sccm respectively. 2-(dimethylamino)ethyl methacrylate (DMAEMA, Aldrich, 98%) and ethylene glycol dimethacrylate (EGDMA, Aldrich, 98%) monomers were heated up to 55 °C and 80 °C in glass jars, respectively and delivered into the reactor using needle valves. Systematic variation of the flow rate ratios was performed to yield insoluble films of poly[2-(dimethylamino)ethyl methacrylate-*co*-ethylene glycol dimethacrylate] (PDE) with high zwitterionic-percentage. Films were deposited at a filament temperature of 250 °C and a stage temperature of 20 °C. Total pressure in the vacuum chamber was maintained at 0.215 Torr for all depositions.

In situ interferometry with a 633 nm HeNe laser source (JDS Uniphase) was used to monitor the film growth and deposit desired thicknesses on Si substrates. A more accurate film thickness on the Si wafer substrates was measured post-deposition using a J.A. Woollam M-2000 Variable Angle Spectroscopic Ellipsometry (VASE) at three different incidence angles (65°, 70°, 75°) using 190 wavelengths from 315 to 718 nm. The data were fit using a Cauchy-Urbach model.

After deposition, the coated substrates were fixed in a crystallizing Dish (VWR) with 1g 1,3-propanesultone (Aldrich, 98%). The crystallizing dish was placed inside a vacuum oven (Shel Lab, 1415M) which was maintained at 60 Torr, 80 °C for 6 hour to let 1,3-propanesultone vapor react with the coating on substrates.

Film characterization. Fourier transform infrared (FTIR) measurements were performed on a Nicolet Nexus 870 ESP spectrometer in normal transmission mode. A deuterated triglycine sulfate (DTGS) KBr detector over the range of 400-4000 cm^{-1} was utilized with a 4 cm^{-1} resolution. Films on Si wafers were measured immediately after deposition or post-treatment and measurements were averaged over 128 scans to improve the signal-to-noise ratio. All spectra were baseline corrected by subtracting a background spectrum of the Si wafer substrate and smoothed by averaging 17 adjacent points.

An X-ray photoelectron spectroscopy (XPS) survey spectrum was obtained on a Kratos Axis Ultra spectrometer with a monochromatized Al KR source, operated at 150 Watts. The pass energy and step size for survey scans was 160 eV and 1 eV. For high-resolution scans, the pass energy and step size was 20 eV and 100 eV. Pressure during analysis was kept under 2×10^{-8} Torr. The analysis area was 400×750 μm and the take-off angles were 90^{o} and 19.5^{o} respectively for the angle-resolved XPS (ARXPS). CasaXPS was used to fit the high-resolution spectra, with Shirley as the background. All samples were stored under vacuum overnight prior to analysis.

Hydrophilicity and contact angle hysteresis of the coatings were evaluated by sessile drop measurements performed on a goniometer equipped with an automatic dispenser (Model 500, Ramé-Hart). 2 μL DI water droplet was used for the static contact angle measurement.

The scanning electron microscope (SEM) images were obtained by JEOL J5M-6700F with acceleration voltage of 10 kV. Reverse osmosis (RO) membranes were frozen by liquid nitrogen and broken to obtain cross-sections. 6 nm of gold (Denton Desk II) was sputter coated onto all the samples prior to taking images.

The surface roughness characterization of the coatings was performed using atomic force microscope (AFM, Veeco, Nanoscope V with Dimension 3100). Tapping mode was employed to prevent damage to the surface morphology.

Film thicknesses were measured using VASE (JA Woollam M-2000) for both dry and swollen films by mounting coated wafers in a liquid cell (JA Woollam). An incident angle of 75° was used and the data were fit to a Cauchy-Urbach isotropic model with an ambient water layer using commercial modeling software (WVASE32, JA Woollam).

Fouling tests. The inertness of the iCVD zwitterionic coating was determined using QCM-D (Model E4, Q-sense). Three foulants were selected including sodium alginate (SA), humic acid (HA) and bovine serum albumin (BSA), representing polysaccharide, natural organic matter and protein respectively. The solution concentration of 1mg/mL was used for all three foulants in all the tests. Gold-coated QCM-D sensors with a fundamental frequency of 5 MHz (QSX-301, Q-sense) were used as a deposition substrate. Duplicate coated sensors and blank reference were placed in flow cells and allowed to equilibrate at 25^{o}C for 30 minutes while flowing deionized water (DI, for SA and HA) or phosphate buffered saline (PBS, for BSA) at the rate of 100 μL/min. Then the solution was changed to SA or HA in DI, or BSA in PBS, and monitored at constant temperature.

3.4 Results and Discussion

3.4.1 Film synthesis and surface zwitterionic moieties

The chemical structure and synthesis route of the investigated zwitterionic copolymer PDDE are shown in Fig. 3-1. In addition to 2-(dimethylamino)ethyl methacrylate (DMAEMA), comonomer ethylene glycol dimethacrylate (EGDMA) was used as the cross-linker to render the copolymer water-insoluble. The copolymers were synthesized via iCVD. The copolymers feature full retention of the tertiary amine functional groups, which is difficult to achieve by other CVD methods such as PECVD.[22,23] The reaction with 1,3-propanesultone (PS) was carried out at the gas-solid interface. Due to the limited diffusivity of polymer thin films,[24,25] only the very top layer of the copolymer is anticipated to have access to the PS molecules and thus possess the zwitterionic moieties via the reaction shown in Fig.3-1b.

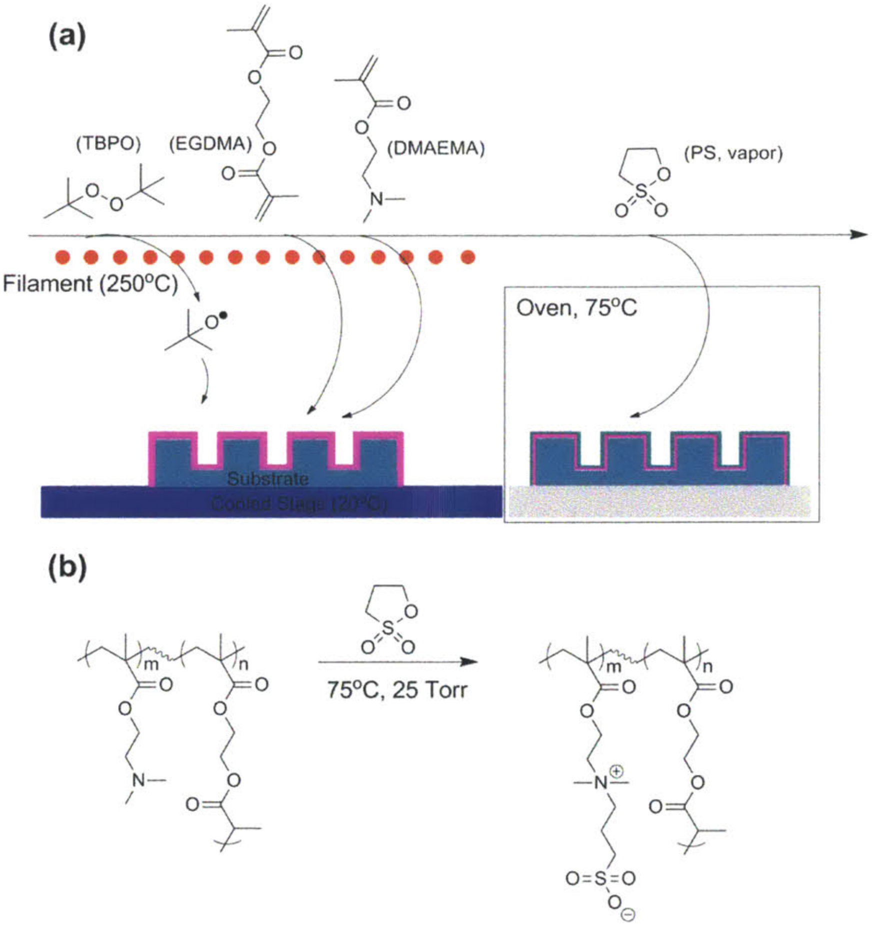

Figure 3-1| Synthesis scheme of the iCVD zwitterionic copolymers. iCVD deposition of random copolymer Poly[2-(dimethylamino)ethyl methacrylate-co-ethylene glycol dimethacrylate] (PDE) is followed by vapor phase reaction with PS at 75 °C for 6 hours (a). The red dots represent the heated filaments, which thermally decompose the initiator tert-butyl peroxide (TBPO) and generate oxide free radicals to initiate the polymerization. The pink layer represents the copolymer; the green layer represents the reacted zwitterionic top layer. The reaction between tertiary amine in the polymer and gas phase 1,3-propanesultone(b) is carried out under diffusion limitations.

The occurrence of this reaction was confirmed by Fourier transform infrared spectroscopy (FTIR) and X-ray photoelectron spectroscopy (XPS). The 1036 cm^{-1} adsorption on the FTIR spectrum (Fig. 3-2) is ascribed to the symmetric stretch vibration of the SO_3^- group,[26] indicating the ring-opening of 1,3-propanesultone.

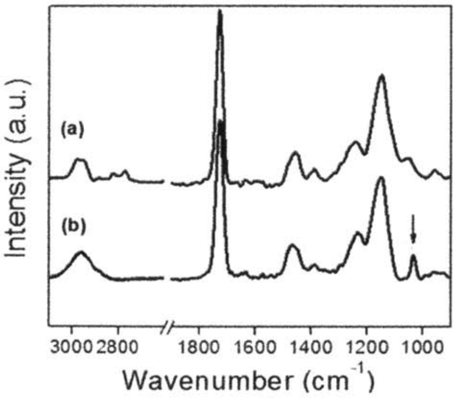

Figure 3-2| FT-IR spectra of the iCVD films before (a) and after (b) the reaction with PS. The arrow indicates the characteristic peak of the SO_3^- group, which appears only in the reacted films.

The formation of quaternary ammonium introduces a new nitrogen environment, as evidenced by the N (1s) XPS spectrum (Fig. 3-3). The reaction conversion is ~90%, as estimated by fitting the N (1s) envelop: tertiary amine (reactant) at 399.4-400.3 eV and quaternary ammonium (product) at 402.1-402.5 eV.[27-29] This set of data was obtained using a photoelectron takeoff angle of 55°, and the corresponding analysis depth is ~7 nm (1-1/e, i.e. ~63% of electrons collected are from < 3nm depth into the film; ~30% from 3-5 nm and ~5% from 5-7nm). It is worth noting that even in the control film (unreacted copolymer), a small protonated amine peak around 401.3-402.6 eV[27,30] was observed. This has been reported and attributed to post-treatment adsorption of atmospheric CO_2.[29,31]

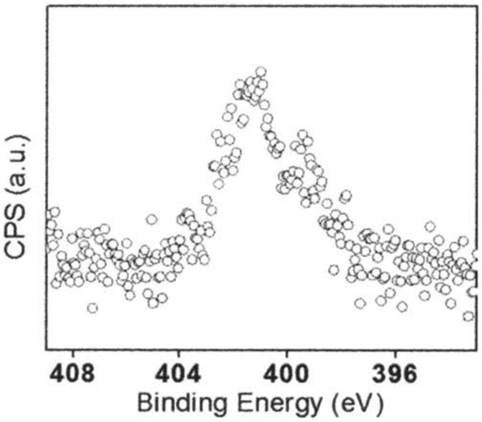

Figure 3-3| XPS spectrum of N(1s) of the iCVD zwitterionic film. The large peak near 401 eV represents quaternary amine (reacted); while the tail near 400 eV represents the tertiary amine (unreacted).

Depth profiling XPS of the N(1s) was carried out on a 100 nm film to test the assumption that the zwitterionic groups are highly concentrated on the top of the film. Ion bombardment was used to remove a ~10 nm thickness of the film with each time step, and XPS was conducted at each corresponding depth. The total percent of quaternary ammonium and protonated amine along the film cross section is plotted in Fig. 3-4a. The amount of quaternary ammonium and protonated amine in the top ~7 nm film is about 90%; while deeper in the film, this amount levels off at about 20%, which is likely due to the adsorption of atmospheric CO_2 as mentioned previously. To examine the fine composition profile of the top ~7 nm, angle-resolved XPS (ARXPS) measurements were carried out.

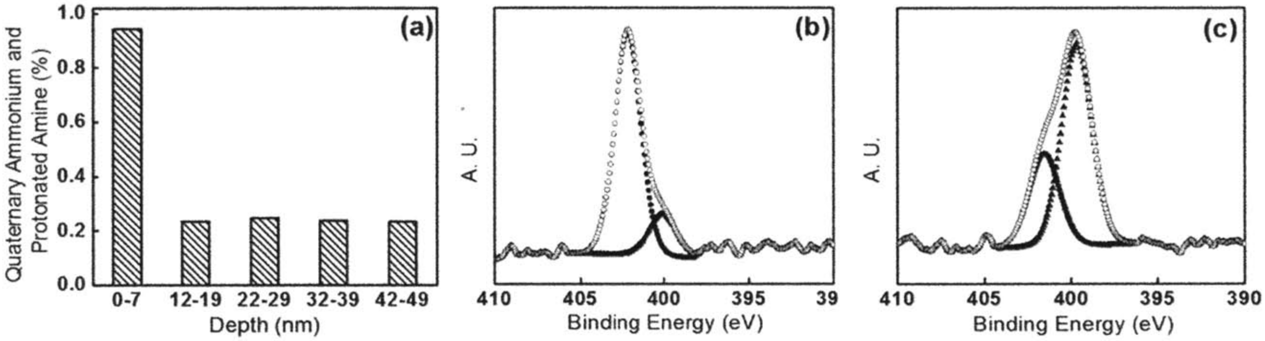

Figure 3-4| Concentrations of quaternary ammonium and protonated amine along the film cross-section and ARXPS spectra. Composition of the zwitterionic component (quaternary ammonium) at different depth in the film (a) was obtained by ion-bombardment followed by XPS measurement. High resolution ARXPS N (1s) scans were obtained with photoelectron takeoff angles of 19.5° (b) and 90° (c).

ARXPS has been widely used in characterizing the concentration profile in the z-direction (i.e., the cross-section) of a zwitterionic thin film coating. Ruiz *et al.* applied ARXPS on zwitterionic thin films synthesized and casted via bulk solution polymerization and solvent evaporation. The zwitterionic moieties were undetectable at 3 nm into the film; while at 9 nm, about 0.3% nitrogen component was detected, which corresponded to ~2% zwitterionic component in the terpolymer.[12] Yang *et al.* prepared terpolymer containing zwitterionic component and the ARXPS revealed decreased nitrogen content once the escape depth was decreased from 9nm to 2nm, indicating lower zwitterionic concentration near the interface than that in the bulk film. This concentration profile is not ideal for the antifouling purpose because the fouling resistance of a zwitterionic coating is strongly dependent on the surface concentration of zwitterionic moieties.[16,17] Therefore, surface-concentrated zwitterionic moieties are highly desirable. Here, two photoelectron takeoff angles (19.5° and 90°) were used, and the corresponding escape depths (depths sampled in ARXPS scans) are approximately ~3 nm (~63%

of electrons collected are from < 1nm depth into the film; ~30% from 1-2 nm and ~5% from 2-3nm) and ~9 nm (~63% of electrons collected are from < 3nm depth into the film; ~30% from 3-6 nm and ~5% from 6-9nm). As shown in Fig. 3-4b and 3-4c, the atomic ratios of quaternary ammonium are drastically different for these two scans. The zwitterionic groups are highly enriched (~97% of the total nitrogen) within the top ~3 nm, while at the escape depth of ~9 nm, the unreacted tertiary amine becomes the dominant species (with ~30% of the total nitrogen being quaternary ammonium). It is important to note that the currently observed high concentration of zwitterionic groups at the surface is exactly opposite to films formed by solution phase methods.[12,13,16] The current high surface concentrations are obtained because the gas phase reaction is diffusion-limited and thus the highest conversion is achieved on the surface, precisely where the anti-fouling properties of the zwitterionic groups can be exploited.

3.4.2 Surface structure reorganization and stability in ambient air

The dynamic water contact angle measurement was conducted using the sessile drop technique. The advancing and receding contact angles are ~43° and ~20° respectively (Fig. 3-5 inset (a) and (b)), with a contact angle hysteresis of ~23°(Fig. 3-5).

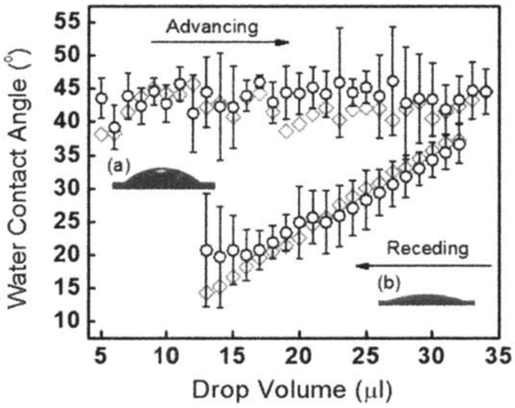

Figure 3-5| Contact angle hysteresis, and images of the droplets. ○ indicates the results obtained with freshly-prepared samples; ◊ represents the dynamic contact angles measured after 100 days of storage. There is no significant difference between the two sets of data, indicating that the surface composition remains the same. A droplet during the advancing measurement (a) and one during the receding measurement (b) are demonstrated as insets.

The three main factors to contact angle hysteresis are surface roughness, swelling and surface chain reorganization.[32] In order to estimate the effects of surface roughness, the contact angle hysteresis of a highly crosslinked, non-swelling iCVD polymer, poly(divinyl benzene) (PDVB) is measured. Given the similar surface roughness of all iCVD thin films,[19,22,33] the hysteresis of PDVB is a good presentation of the effects of surface roughness for the iCVD PDDE films. As shown in Fig. 3-6, the hysteresis of PDVB is ~14°, which is ~8° lower than that of our films. Then the swelling of the iCVD PDDE films was measured.

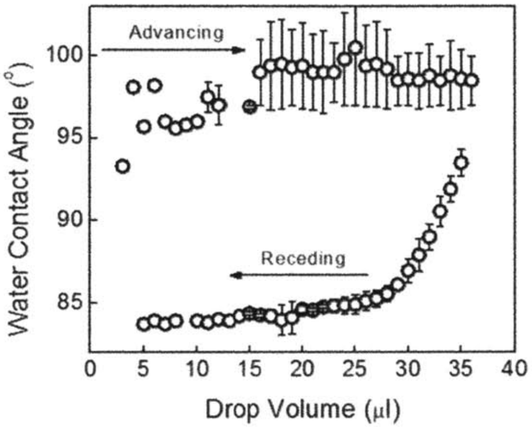

Figure 3-6| Water contact angle hysteresis of the iCVD PDVB film, measured via sessile drop method. PDVB is a highly-crosslinked and non-swelling polymer, and thus its hysteresis is mainly resulted from surface roughness. The advancing contact angle is about 98° and the receding contact angle is about 84°.

Interestingly, the iCVD PDDE film did not swell significantly upon contacting water (Fig. 3-7), which is likely resulting from the crosslinking in the bulk polymer. Thus the higher hysteresis is likely due to the quick surface chain reorganization upon contacting water.

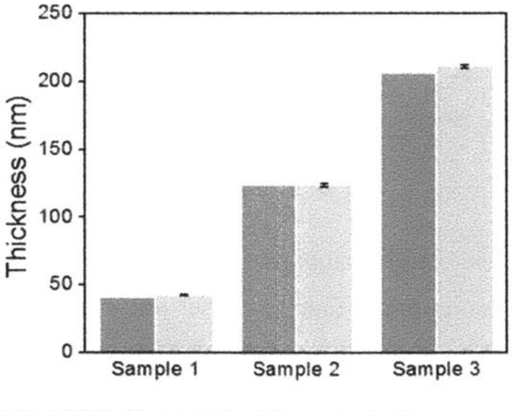

Figure 3-7| The swelling of iCVD PDDE films with different thicknesses, as measured by VASE. Under dry conditions, the thicknesses are about 43 nm, 124 nm and 207 nm for samples 1, 2 and 3 respectively. When samples are soaked in water, the thicknesses become 43 nm, 124 nm and 211 nm, which are essentially the same as those under dry conditions given the statistics of the measurement.

It has been reported that long periods of aging may result in the irreversible migration of hydrophobic sections toward the surface, which decreases the fouling resistance and biocompatibility of the materials.[13] Therefore iCVD PDDE films were stored in open air for 100 days and the dynamic contact angles, which indicate possible changes in surface structure, were measured again. As shown in Fig. 3-5 (grey diamonds), the advancing and receding contact angles of the "aged" sample overlap with the freshly-prepared samples, implying good stability of the surface structure against aging effects.

3.4.3 Substrate-independent and conformal coating on various substrates

iCVD is a mild process, which can successfully coat practical substrates that may lack solvent or thermal resistance or have non-planar geometries.[34,35] Fig. 3-8a and 3-8b display the conformality of iCVD zwitterionic film deposited over micron-scale trenches etched in silicon.

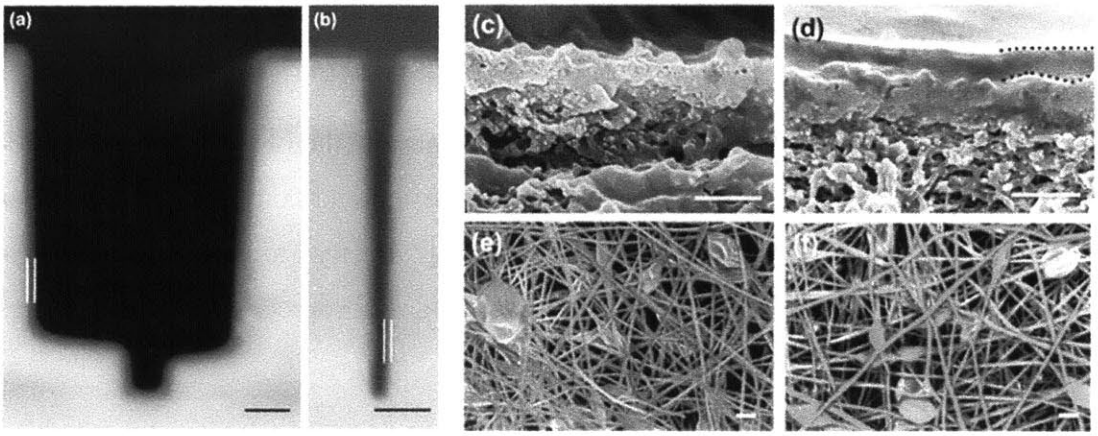

Figure 3-8| SEM images of various coated/uncoated substrates. a) Cross-section of iCVD coated trenches cut into a silicon wafer with aspect ratios of 1.5:1, and b) 14:1. Both images represent good conformality over surface features in the substrate. The white lines are guides to highlight film thickness. SEM images of c) uncoated and d) 600 nm coated reverse osmosis membranes, and e) uncoated and f) coated electronspun nanofiber mats. The dotted line in image b) ii highlights iCVD coating thickness of ~600nm. The scale bar represents 1 μm on images a), b), c) and d), and 10 μm on image e) and f).

In agreement with results for other iCVD polymers,[22,23,36] conformality improved on reduction of the monomer partial pressure. On the other hand, the non-conformal nature of various solution phase methods renders it difficult to coat nanostructures or modify the internal pores of membranes. Even for dry methods such as PECVD, good conformality can be difficult to achieve due to the presence of charged species and nonuniform electric fields.[22] For the iCVD process, conformality can also be achieved on the nano-scale features of both reverse osmosis membranes and electrospun nanofiber mats. Fig. 3-8c and 3-8d verifies that iCVD PDDE film can successfully coat RO membranes, preserving the thin composite film morphology while providing antifouling properties. The morphology of the nanofiber mat remained unchanged after deposition (Fig. 3-8e and 3-8f), without the merging of individual fibers at crossover points seen many times with solution processing methods, thus retaining the high surface area of the mat. The thickness of the coatings in Fig. 3-8 ranges from 300 to 600 nm. However, ultrathin coatings with the thickness around 30 nm have been deposited on RO membranes to minimize the impact on the membrane performance.

3.4.4 Fouling resistance of the iCVD zwitterionic thin film

Quartz crystal microbalance measurements with dissipation monitoring (QCM-D) were used to monitor the adsorption of various foulants on the PDDE films.[33,37] Frequency change of the QCM-D crystal was monitored while a solution of foulant was passed through the QCM-D cell. Fig. 3-9a depicts the frequency and dissipation changes when BSA was used as the foulant, with the black and grey curves representing the frequency signals and the blue curves representing the dissipation signals. The iCVD zwitterionic surface was tested and compared with gold and the unreacted copolymer surface (i.e., the coating obtained directly from iCVD deposition and without the reaction with 1,3-propanesultone). The surface-adsorbed mass can be quantified from the frequency change through the Sauerbrey relationship,

$$\Delta m = -C\frac{1}{n}\Delta f \tag{3-1}$$

where Δm is the mass change, C is a crystal-specific constant (17.7 ng s cm^{-2}), n is the harmonic overtone and Δf is the frequency change.[37] Therefore, the adsorbed mass is related linearly to the frequency changes provided that the adsorbed mass is evenly distributed, does not slip on the surface, and is sufficiently rigid and/or thin to have negligible internal friction.[38] The dissipation changes correlate with the viscoelasticity of the film and adsorbed mass. The small dissipation changes imply that the BSA molecules are surface adsorbed as opposed to absorbed. The frequency changes in Fig. 3-9a record the rapid adsorption of protein to the bare QCM-D crystal when the surface is gold and the absorbed surface BSA concentration is ~210 ng cm^{-2} as calculated using equation (3-1).

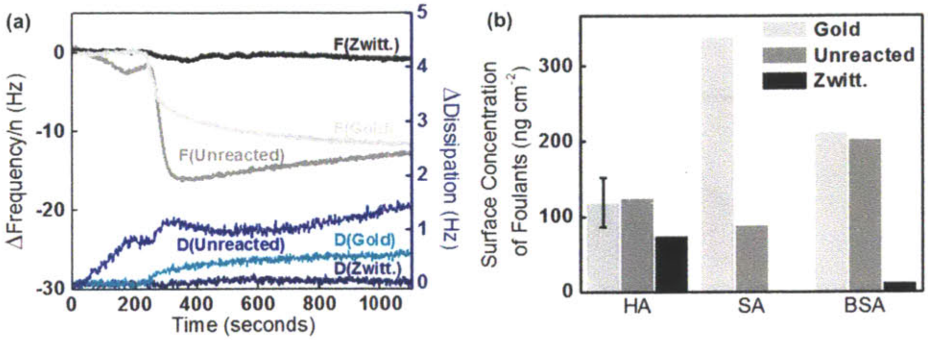

Figure 3-9| Fouling resistance of the iCVD zwitterionic coatings measured with QCM-D. QCM-D data depicts frequency and dissipation changes over time as BSA was introduced to the system at time = ~230 second (a). The black line represents the protein adsorption onto a QCM-D sensor coated with iCVD zwitterionic film. The dark grey line represents the protein adsorption onto a sensor coated with the unreacted copolymer film, while the light grey line represents that onto a bare gold sensor. The dissipation changes are not significant for all three surfaces. Therefore the frequency changes are proportional to the mass of the protein adsorbed. Fouling by protein (BSA), polysaccharide (sodium alginate, or SA) and natural organic matter (humic acid, or HA) onto all three surfaces are quantified with QCM-D (b). The black columns indicate the surface concentrations of the foulants at the end of the test on the iCVD zwitterionic surface; while dark grey columns indicate the results for the unreacted copolymer surface and light grey ones correspond to the gold surface.

The adsorption of BSA to the unreacted copolymer film is comparable to the gold surface (~200 ng cm^{-2}); while the adsorption onto the iCVD zwitterionic surface is much lower (~14 ng cm^{-2}), indicating the good antifouling properties of the iCVD zwitterionic coating. Therefore we demonstrated that the presence of the zwitterionic groups is responsible for the fouling resistance of the surface and the diffusion-limited gas phase reaction is necessary for rendering the copolymer coating antifouling. The protein resistance of the zwitterionic films was also confirmed by static protein-adsorption tests, characterized by atomic force microscopy (Fig. 3-10).

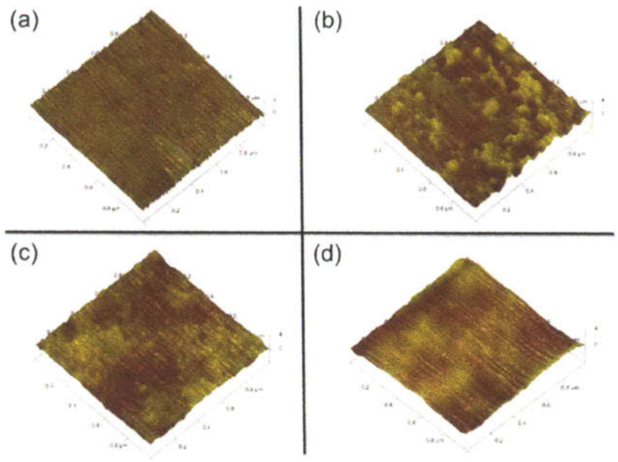

Figure 3-10| AFM images of bare and iCVD-modified surfaces before and after exposure to protein. Bare silicon wafer (a) and silicon wafer coated with iCVD PDDE film (c) were soaked in a solution of BSA for 12 hours. Surface roughness changed significantly for bare silicon (b) after the soaking, indicating the adsorption of BSA. For the coated wafer, the roughness remains almost unchanged before (c) and after the soaking (d).

Similar fouling tests were conducted by flowing 1mg/ml sodium alginate or humic acid in DI through the uncoated QCM-D sensor and the sensors coated with the unreacted copolymer and zwitterionic thin film (Fig. 3-9b). Sodium alginate (SA) is a model polysaccharide that is widely adopted as a representative foulant in marine fouling tests.[39] In this case, the observed surface adsorption for the gold surface was more dramatic. The dissipation change was more significant as well (~10 Hz), implying the formation of multilayers of adsorbed sodium alginate molecules. The frequency change was ~19 Hz, corresponding to a surface concentration of sodium alginate of ~340 ng cm^{-2}. The adsorption of sodium alginate on the unreacted copolymer coating was ~90 ng cm^{-2}. The adsorption onto the iCVD zwitterionic surface is undetectable. Humic acid (HA) is another important model foulant in marine fouling studies. When 1mg/ml humic acid solution was fed into the QCM-D flow cell containing the sensors with the three different surfaces (i.e., gold, unreacted copolymer and zwitterionic surfaces), lower fouling on the zwitterionic surface was observed than the gold and unreacted copolymer surfaces (Fig. 3-9b). The error bar (~33 ng cm^{-2}, corresponding to ~1.9 Hz in frequency) shows the standard deviation between two different runs. These results demonstrated the ability to resist protein adsorption on a surface afforded by an iCVD PDDE thin film, whose antifouling properties are comparable to the counterparts fabricated via solution phase methods.[3,4]

It has been accepted both theoretically and experimentally that the excellent fouling resistance of zwitterionic surfaces is a result of strong electrostatic interaction with the ambient water molecules.[17,18] It is important to note that the fouling resistance of zwitterionic surfaces depends strongly on the surface concentration of zwitteironic moieties. For the zwitterionic SAMs, even 1% impurity in the thiol can cause a 3-fold increase in protein adsorption.[17] This decreased fouling resistance has also been observed for thin film polymer coatings fabricated via bulk solution phase polymerization and solvent evaporation.[16,40] Ishihara *et al.* studied two different compositions of zwitterionic copolymers made from solution phase free radical polymerization, and discovered that the surface concentration of all proteins from human plasma decreased with increasing content of zwitterionic groups, and thus increasing hydrophilicity, in thin film polymer.[40] However, the uppermost surface of the polymer thin films fabricated via solution phase polymerization and solvent evaporation is often hydrophobic and depleted in zwitterionic groups (Fig. 3-11a upper panel). The hydrophilic zwitterionic moieites are rather cover by the more hydrophobic polymer chains to minimize the surface energy in dry environments.[12]

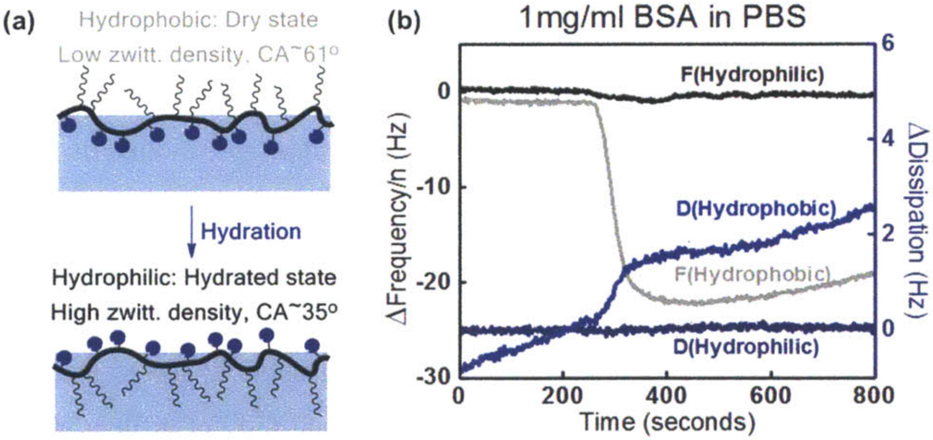

Figure 3-11| The correlation between the surface zwitterionic content, hydrophilicity and fouling resistance. a) the dependence of the surface hydrophilicity on the surface zwitterionic content. Solution phase polymerization and solvent evaporation usually results in hydrophobic surface (upper panel) under dry condition to minimize the interface energy in air. The hydrophobic chains predominantly cover the surface and result in low zwitterionic surface content, and thus the contact angle is high. The homopolymer of PEGDMA was used to mimic this surface and the static contact angle was 61±2°. When the zwitterionic coating fabricated via solution polymerization and solvent evaporation is fully hydrated, the zwitterionic moieties become the dominant species on the surface. The static contact angle of the iCVD zwitterionic surface was 35±1°. Therefore, the higher surface zwitterionic concentration corresponds to lower contact angle. b) The dependence of the surface fouling resistance on the surface hydrophilicity/zwitterionic content. The QCM-D data depicting frequency and dissipation change over time as BSA was introduced to the system at time = ~260 second. The black line represents the protein adsorption onto the hydrophilic iCVD zwitterionic film, while the grey line represents that onto the less hydrophilic PEGDMA surface. This illustrates that the resistance to protein fouling is highly dependent on the hydrophilicity/zwitterionic content of the surface.

The buried zwitterionic groups do not play a pivotal role in resisting foulants adsorption, but the surface can become hydrophilic and antifouling by the hydration treatment and a new minimum interfacial energy state is reached by surface chain reorganization to present the zwitterionic groups at the top surface (Fig. 3-11a, lower panel). Here, the correlation between the surface zwitterionic concentration and the fouling resistance was investigated using BSA as a model protein. To mimic the hydrophobic surface directly obtained from solution phase polymerization and solvent evaporation, 200nm homopolymer PEGDMA film was deposited on a QCM-D sensor. ARXPS results have proven that the two-step iCVD method obtains surface-concentrated zwitterionic moieties without hydration pretreatment. Therefore, the fouling resistance of the iCVD zwitterionic coatings was compared with that of the PEGDMA coating to elucidate the correlation between the surface zwitterion concentration and the fouling resistance. 1 mg/mL BSA in PBS solution was fed into the QCM-D flow cell at the rate of 100μL/min and changes in the frequency and the dissipation were recorded and plotted in Fig. 3-11b. The hydrophilic surface (i.e., iCVD zwitterionic surface) exhibited low surface adsorption of BSA, while the surface covered by the hydrophobic chains from the cross-linker showed significant adsorptions. No dissipation change was observed for the hydrophilic surface, which confirmed the fouling resistance. The dissipation change of the hydrophobic surface was ~3 Hz, which indicated that the BSA molecules were surface adsorbed and did not diffuse into the bulk film. Given the small change in the dissipation, Sauerbrey equation was used to model the frequency change and quantify the adsorbed protein concentration at the end of the test for the hydrophobic surface. The adsorbed protein was ~320 ng cm^{-2}. Therefore, we demonstrated that the presence of the zwitterionic moieties at the uppermost surface is closely correlated with the fouling resistance of the surface. Higher coverage of the zwitterionic groups gives better antifouling performance. The surface-concentrated zwitterionic functionalities generated via the two-step iCVD scheme does not require any hydration or pretreatment and showed superior fouling resistance compared with the hydrophobic surfaces, which mimicks the surface obtained directly from solution phase polymerization and solvent evaporation.

It is worth noting that the fouling characteristics of humic acid were found to be dependent on the solution chemistry. The fouling by humic acid increased dramatically with the presence of $CaCl_2$ (Fig. 3-12).

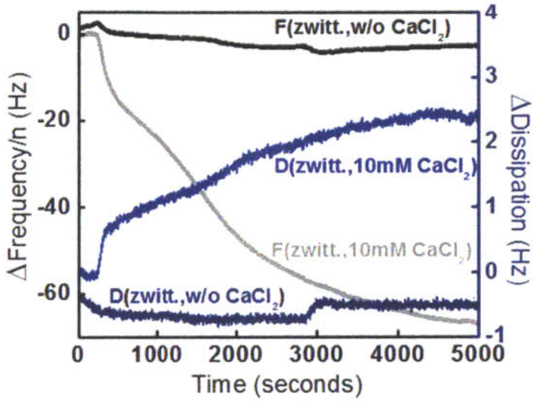

Figure 3-12| Dependence of the fouling properties of humic acid on the presence of divalent cations. The black line and deep blue line represent the frequency and dissipation changes respectively, when humic acid is introduced into the system without $CaCl_2$ in the feed solution. The grey line and blue line represent the frequency and dissipation changes when the concentration of $CaCl_2$ in the humic acid solution is ~10 mM. The surface adsorption of humic acid depends strongly on the presence of divalent cations, Ca^{2+} in this case.

Similar trends have been observed for the fouling of nano-filtration membranes by humic acid,[39,41] where the carboxyl moieties in humic acid interact with the Ca^{2+} cations in the solution and form a compact cake layer on the surface of interest. The increased fouling tendency with the presence of divalent cation is likely caused by a small amount of surface charge. Since the reaction with PS does not reach 100% conversion, it is possible that the tertiary amine residues are protonated in the humic acid solution, and therefore the surface becomes positively charged and loses the fouling resistance. It will be the focus of future work to develop a charge-neutral zwitterionic coating that resist fouling under all conditions.

3.5 Conclusion

The two-step fabrication of iCVD zwitterionic coatings resulted in high surface concentration of zwitterionic moieties, which rendered the substrate surface fouling-resistant for a variety of model biofoulants, including BSA, humic acid, and sodium alginate. The iCVD zwitterionic films are stable in air and display the same dynamic contact angles after 100 days of storage. ARXPS proves the high yield of zwitterionic functional groups on the top surface after a diffusion-limited gas phase reaction.

iCVD method has the ability to conform to the roughness and surface features in the substrate. Additionally, it is substrate independent, and able to form zwitterionic coatings on substrates which are incompatible with solution methods. The successful coating of various substrates, including the delicate reverse osmosis (RO) membranes and electrospun nanofiber mats, has been demonstrated. No re-optimization is required for each new type of substrate. This substrate independence is a result of the absence of concerns about wettability during vapor phase processing.

Combining the mild nature and the high conformality of iCVD, this substrate-independent surface modification made the zwitterionic chemistry more accessible for a larger variety of applications. Even higher densities of zwitterionic functionalities can be obtained by depositing "graded films"[42] and this will be a possible future direction of this work.

ACKNOWLEDGMENT. The authors would like to thank the King Fahd University of Petroleum and Minerals in Dhahran, Saudi Arabia, for funding the research reported in this paper through the Center for Clean Water and Clean Energy at MIT and KFUPM. We thank Jonathan Shu from Cornell Center for Materials Research (CCMR) for his help with XPS measurements and Looh Tchuin Choong from the Department of Chemical Engineering at Massachusetts Institute of Technology for providing the electrospun nanofiber mats.

References

1. Yang, R., Asatekin, A. & Gleason, K. K. *Soft Matter* **8,** 31-43, (2012).
2. Banerjee, I., Pangule, R. C. & Kane, R. S. *Adv. Mat.* **23,** 690-718, (2010).
3. Holmlin, R. E., Chen, X. X., Chapman, R. G., Takayama, S. & Whitesides, G. M. *Langmuir* **17,** 2841-2850, (2001).
4. Jiang, S. & Cao, Z. *Adv. Mat.* **22,** 920-932, (2010).
5. Nguyen, A. T., Baggerman, J., Paulusse, J. M. J., van Rijn, C. J. M. & Zuilhof, H. *Langmuir* **27,** 2587-2594, (2011).
6. Li, G. *et al. Biomaterials* **29,** 4592-4597, (2008).
7. Olenych, S. G., Moussallem, M. D., Salloum, D. S., Schlenoff, J. B. & Keller, T. C. S. *Biomacromolecules* **6,** 3252-3258, (2005).
8. Salloum, D. S., Olenych, S. G., Keller, T. C. S. & Schlenoff, J. B. *Biomacromolecules* **6,** 161-167, (2004).
9. Schlenoff, J. B., Dubas, S. T. & Farhat, T. *Langmuir* **16,** 9968-9969, (2000).
10. Nogueira, G. M., Banerjee, D., Cohen, R. E. & Rubner, M. F. *Langmuir* **27,** 7860-7867, (2011).
11. Krogman, K. C., Lowery, J. L., Zacharia, N. S., Rutledge, G. C. & Hammond, P. T. *Nat Mater* **8,** 512-518, (2009).
12. Ruiz, L., Hilborn, J. G., Leonard, D. & Mathieu, H. J. *Biomaterials* **19,** 987-998, (1998).
13. Yang, S., Zhang, S.-P., Winnik, F. M., Mwale, F. & Gong, Y.-K. *J. Biomed. Mater. Res., Part A* **84A,** 837-841, (2008).
14. Yamasaki, A. *et al. Colloids Surf., B* **28,** 53-62, (2003).
15. Lewis, A. L. *et al. Biomaterials* **21,** 1847-1859, (2000).
16. Futamura, K., Matsuno, R., Konno, T., Takai, M. & Ishihara, K. *Langmuir* **24,** 10340-10344, (2008).
17. Chen, S. F., Zheng, J., Li, L. Y. & Jiang, S. Y. *JACS* **127,** 14473-14478, (2005).
18. Kitano, H. *et al. Macromol. Biosci.* **5,** 314-321, (2005).
19. Yang, R., Xu, J., Ozaydin-Ince, G., Wong, S. Y. & Gleason, K. K. *Chem. Mater.* **23,** 1263-1272, (2011).
20. Ozaydin-Ince, G. & Gleason, K. K. *J. Vac. Sci. Technol., A* **27,** 1135-1143, (2009).
21. Martin, T. P., Kooi, S. E., Chang, S. H., Sedransk, K. L. & Gleason, K. K. *Biomaterials* **28,** 909-915, (2007).
22. Alf, M. E. *et al. Adv. Mat.* **22,** 1993-2027, (2010).
23. Tenhaeff, W. E. & Gleason, K. K. *Adv. Funct. Mat.* **18,** 979-992, (2008).
24. Wichterlová, J., Wichterle, K. & Michálek, J. *Polymer* **46,** 9974-9986, (2005).
25. Deen, W. M. *Analysis of Transport Phenomena.* (Oxford University Press, USA, 1998).
26. Lin- Vien, D. C., N. B.; Fateley, W. G.; Grasselli, J. G. *The Handbook of Infrared and Raman Characteristic Frequencies of Organic Molecules.* (Academic Press, New York, 1991).
27. Beamson, G. & Briggs, D. *High resolution XPS of organic polymers: the Scienta ESCA300 data base.* (John Wiley & Sons, New York, 1992).
28. Moulder, J., F., Stickle, W., F., Sobol, P., E. & Bomben, K., D. *Handbook of X-ray photoelectron spectroscopy.* (Perkin-Elmer Corporation, Minnesota, MN, 1992).
29. Spanos, C. G., Badyal, J. P. S., Goodwin, A. J. & Merlin, P. J. *Polymer* **46,** 8908-8912, (2005).
30. Jansen, R. J. J. & van Bekkum, H. *Carbon* **33,** 1021-1027, (1995).
31. Chakraborty, A. K., Bischoff, K. B., Astarita, G. & Damewood, J. R. *JACS* **110,** 6947-6954, (1988).
32. Quéré, D. *Annu. Rev. Mater. Res.* **38,** 71-99, (2008).
33. Baxamusa, S. H. & Gleason, K. K. *Adv. Funct. Mat.* **19,** 3489-3496, (2009).
34. Baxamusa, S. H. I., S. G.; Gleason, K. K. *Phys. Chem. Chem. Phys.* **11,** 5227-5240, (2009).
35. Lau, K. K. S. & Gleason, K. K. *Adv. Mater.* **18,** 1972-1977, (2006).
36. Ozaydin-Ince, G. & Gleason, K. K. *Chem. Vap. Deposition* **16,** 100-105, (2010).

37. Sauerbrey, G. *Zeitschrift Für Physi* **155,** 206-222, (1959).
38. Höök, F., Rodahl, M., Kasemo, B. & Brzezinski, P. *Proc. Natl. Acad. Sci. U. S. A.* **95,** 12271-12276, (1998).
39. Asatekin, A. *et al. J. Membr. Sci.* **285,** 81-89, (2006).
40. Ishihara, K. *et al. J. Biomed. Mater. Res.* **26,** 1543-1552, (1992).
41. Coclite, A. M., Shi, Y. & Gleason, K. K. *Advanced Functional Materials* **22,** 2167-2176, (2012).
42. Montero, L., Baxamusa, S. H., Borros, S. & Gleason, K. K. *Chem. Mater.* **21,** 399-403, (2008).

CHAPTER FOUR

Control of interfacial adhesion via iCVD chemistry

Reproduced with permission from Yang R., Buonassisi T., and Gleason K. K., *Advanced Materials* **2013**, 25, 2078.

4.1 Abstract

In this chapter, a new method of creating surface passivation has been demonstrated on silicon by using a vapor phase treatment, initiated Chemical Vapor Deposition (iCVD). iCVD passivation offers several advantages over previous techniques including a largely simplified reaction scheme, inexpensive reactants, mild reaction conditions, fast kinetics, and excellent long-term stability. In addition, the iCVD passivation technique allows for the fabrication of a large variety of surface functionalities with desirable surface coverage and adhesion properties on Si (100) surface. Here we directly synthesize organic layers grafted to silicon from an olefin monomer 1,9-decadiene. The surface recombination velocity after the iCVD passivation remains less than 10 cm s^{-1}, over 200 hours of air contact.

4.2 Introduction

Passivation to reduce the surface recombination of minority carriers is of key importance for improving photovoltaic efficiency,[1-3] especially for thin devices. High quality electronic passivation (**Table 4-1**) is achieved for surface recombination velocities (SRV) $\leq$ 10 cm s^{-1}.[4]

Table 4-1| SRV of various passivation techniques

surface chemistry	*SRV [cm s^{-1}]*	*stability in ambient air*	*fabrication conditions*	*typical thickness [nm]*
untreated SiO_x [5]	~10^5	√	N.A.	20– 120
SiN_x [6]	10-10^3	√	PECVD with $T_{substrate}$~375°C	65– 150
Si-H [7]	<1	X	HF etching	Monolayer
ultra-thin SiO_x [8]	~3	√	controlled oxidization and annealing at $T_{substrtae}$ ~1050°C	N.A.
Si-OCH_2CH_3 [7]	~10	X	HF etching-I_2/EtOH	Monolayer
Si-CH_3 [9]	<25	√	solution fabrication under stringent limitation of ambient air and water	Monolayer
iCVD method	≤10	√	HF-iCVD	200 – 700

Chemical vapor deposition (CVD) is currently used in industry to deposit 65-150 nm thick SiN_x, which also acts as an anti-reflective coating (ARC).[6] [10] The high temperature of the SiN_x degrades the quality of the bulk Si and raises operational costs.[11] Thus, lower temperature passivation methods are desired. Additionally, low temperature processing retains organic functionalities, enabling the fabrication of hybrid or multi-functional devices.[10,12] Protocols for organic passivation typically start with chemical etching of the native silicon oxide to obtain H-terminated Si surfaces. The Si-H bonds are subsequently activated by various solution methods.[4] Most organic passivations rely on monolayer coverage rather than on producing layers with nano-scale thickness, as is the case for SiN_x passivation. A two-step chlorination/alkylation scheme produces the lowest air-stable SRV among organic passivations;[4,9] however, the time-consuming process and stringent limitations on ambient water and oxygen contents hindered its industrial application. Ethanol-iodine (E-I) passivation produces SRV~10 cm s^{-1},[7] but this value increases to 10^3 cm s^{-1} within minutes in air. E-I still serves as a good reference for high-quality passivation due to its ease of preparation. In this chapter, we seek a rapid, simple and cost-effective method for forming an air-stable organic passivation layer. Our approach utilizes a variant of initiated CVD (iCVD),[13] which operates under dry conditions for depositing organic layers, and represents a low temperature analog to the CVD utilized for SiN_x passivation. The degradation of the passivation layer caused by solvents is thus prevented. The iCVD method also creates layers of nano-scale thickness which serve other functions in the device, such as ARC. The scale-up of the iCVD process has been demonstrated in a roll-to-roll system,[14,15] which is compatible with the existing infrastructures in semiconductor industries. The iCVD passivation layer, even after 200 hours of air exposure, provides superior passivation performance with a SRV~10 cm s^{-1}.

4.3 Experimental Section

Fabrication process. All initiated Chemical Vapor Deposition (iCVD) passivation and polymerization processes were carried out in a custom built vacuum reactor (Sharon Vacuum), as previously described[16].

All the chemicals were used as purchased without further purification. Passivation and polymerization were performed on typically 1-10Ωcm p-type silicon with the (100) orientation. During Process A, tert-butyl peroxide (TBPO, Aldrich, 97%) initiator and the nitrogen patch flow were fed to the reactor at room temperature through mass flow controllers (1479 MFC, MKS Instruments) at 3 sccm and 1 sccm respectively with the total pressure of 800 mTorr and filament temperature of 312°C for 60 minutes. The chamber is then pumped down to base pressure (~3 mTorr) for ~10 min. 1,9-decadiene (DD, Aldrich, 96%) was heated up to 45 °C in glass jar and delivered into the reactor using needle valves with the total pressure of 800 mTorr and without filament heating for 20 minutes. The TBPO-pump-DD-pump cycle was then repeated for 5 times but with shorter cycle lenghts: TBPO (10 min)-pump (2 min)-DD (10 min)-pump (2min). The silicon wafer is kept at 20°C throughout the process.

During process B, TBPO and ethylene glycol diacrylate (EGDA, Aldrich, 98%) were introduced into the chamber simultaneously as reported previously[17]. Films were deposited at a filament temperature of 250 °C and a stage temperature of 20 °C. Total pressure in the vacuum chamber was maintained at 0.215 torr for all depositions. In situ interferometry with a 633 nm HeNe laser source (JDS Uniphase) was used to monitor the film growth and deposit desired thicknesses on Si substrates. A more accurate film thickness on the Si wafer substrates was measured post-deposition using a J.A. Woollam M-2000 Variable Angle Spectroscopic Ellipsometry (VASE) at three different incidence angles (65°, 70°, 75°) using 190 wavelengths from 315 to 718 nm. The data were fit using a Cauchy-Urbach model.

Characterization methods. The X-ray photoelectron spectroscopy (XPS) spectra were obtained on a Kratos Axis Ultra spectrometer with a monochromatized Al KR source, operated at 150 Watts. The pass energy and step size was 20 eV and 100 eV. The nano-scratching was performed on Nanovea Ergonomic Workstation and the scratching procedure was designed based on ASTM C1624, ASTM D7027 & ASTM G171. The scanning electron microscope (SEM) images were obtained by JEOL J5M-6700F with acceleration voltage of 10 kV. The lifetime measurements were conducted based on Quasi-Steady State Photoconductance (QSSPC) technique with Sinton WCT-120 apparatus. The Spatially resolved photoluminescence images were obtained by exciting the Si with an 822 nm laser while recording a 20 second exposure image with a charge-couple device (CCD) camera. A 1000 nm longpass filter was used to select the band-edge emission of Si. The surface roughness was measured using atomic force microscope (AFM, Veeco, Nanoscope V with Dimension 3100). Tapping mode was employed to prevent damage to the surface morphology.

4.4 Results and Discussion

The passivation procedure is shown as Process A in Fig. 4-1a. Following the HF etching of the native silicon oxide to obtain surface hydride, the iCVD passivation is carried out in a single vacuum chamber at modest vacuum (~0.1 to 1 Torr) and low substrate temperatures (20 °C), with two types of vapor phase reactants: (i) the initiator *tert*-butyl peroxide (TBPO) and (ii) a vinyl monomer 1,9-decadiene (DD).

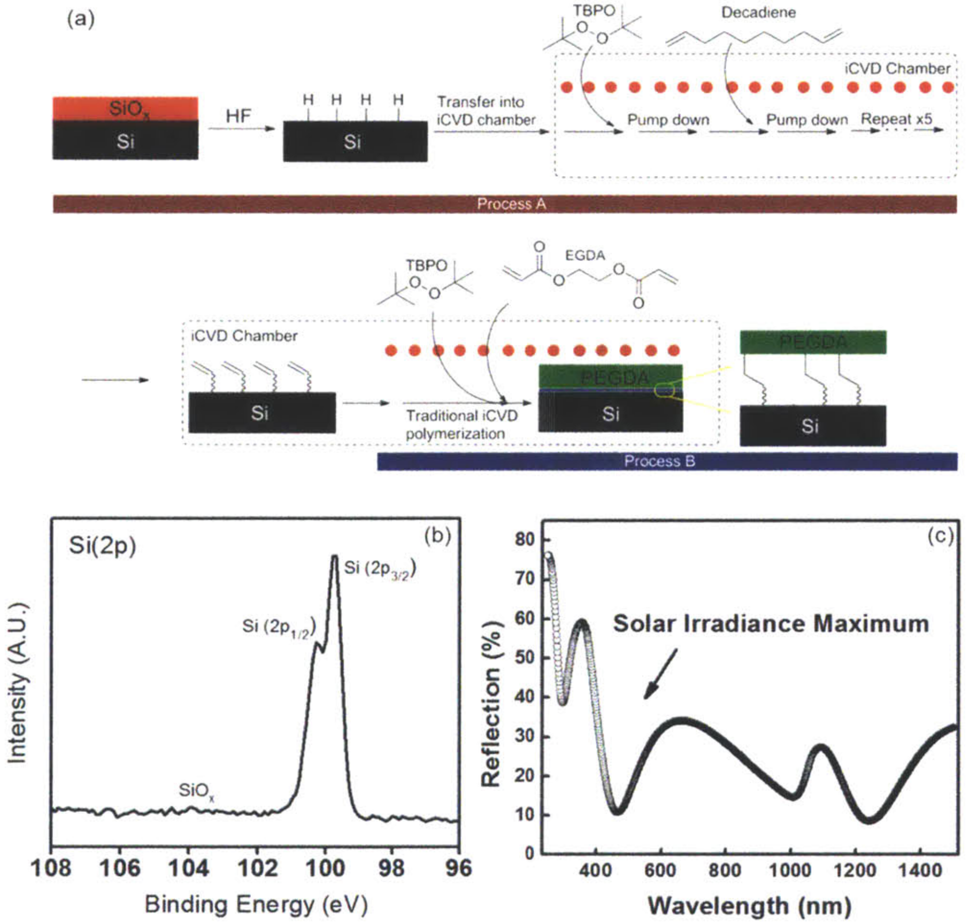

Figure 4-1 | (a) The wafer is transferred into iCVD chamber within 3min after HF etching is completed. TBPO and DD are introduced separately to prevent the formation of polymer. A vapor mixture of TBPO and EGDA is used in Process B, which results in iCVD polymerization. With the surface vinyl groups generated during Process A, the polymer is grafted onto the Si substrate; otherwise only dispersion forces present between the polymer film and the substrate. (b) Si (2p) XPS spectrum of the surface resulted from Process A. The samples have been exposed to air prior to XPS measurements, but the growth of oxide is inhibited by the iCVD passivation. (c) Reflection spectrum of the surface resulted from Process B. The 200 nm ARC is grafted on Si via iCVD passivation layer. The reflection at the wavelength with maximum solar irradiance is suppressed.

Traditional iCVD process delivers the molecules simultaneously to obtain a polymeric layer via free-radical polymerization,[13] however, the novelty of the current work focuses on promoting a reaction between the surface hydride and the vinyl groups of the vapor-delivered monomers. The first layer of iCVD polymer formation is undesirable because it will simply cover the surface hydride groups without reacting, slow down or even stop the monomers from accessing the hydride groups. To prevent polymerization during Process A, TBPO and DD were fed into the chamber sequentially, and the chamber was pumped down to 3 mTorr between the initiator and monomer cycles to minimize the simultaneous presence of the two reactants.

The TBPO vapors were exposed to heated filaments to produce free radicals. Previously, two types of radicals were observed upon the thermal decomposition of TBPO in an iCVD reactor.[18] The dominant free radical species is *tert*-butoxide (TBO) at the filament temperature T_f >150°C; while at T_f >270°C, TBO undergoes β-scission to produce methyl radicals.[18] Interestingly, we note that all samples exhibiting high-quality and air-stable passivation behavior required exposing the silicon wafer to TBPO pyrolyzed at filament temperatures greater than 300 °C as the first step. Prolonged exposure to vinyl monomers alone or simultaneous delivery of TBPO and vinyl monomers with the filament heating does not result in good passivation. This can be explained by the greater reactivity of methyl radicals,[18] which can possibly "activate" Si-H moieties by H-abstraction.[4] It is worth noting that the filament is heated resistively with a typical current value of 1-2 Amp for a total power of 0.0086-0.0343 Watts cm^{-2}. The Si wafer is kept at 20 °C throughout the passivation process, which ensures low energy consumption.

iCVD can utilize essentially any monomer that can be activated by a free radical. The traditional iCVD polymerization process has been used to fabricate functionalized surfaces with a wide variety of useful moieties,[13] such as amine,[16,19] hydroxyl[20] and vinyl.[21] This study focuses on a vinyl functionalized surface, which is a versatile platform for subsequent functionalization via free radical polymerization. The non-branched di-vinyl monomer, DD has linear structure, which minimizes the steric hindrance and improves the coverage on surface Si atoms. DD is chosen among other terminal dienes, because it has the appropriate volatility and can be vaporized and delivered into the iCVD chamber at a moderate temperature. Although the relatively low reactivity (k_p~10 L mol^{-1} s^{-1},[22] greater details in the supplemental materials) and high sensitivity to contaminants of DD requires exceptional cleanliness throughout the process, the lowest minority carrier SRV reported to date has been obtained with iCVD DD passivation among the air-stable organic passivations. The initiator-monomer cycles are repeated for 5 times to obtain higher surface coverage.

The oxidation of the silicon substrate has been an issue for many organic passivation methods.[4,23] A low-quality passivation leaves unreacted surface dangling bonds that are susceptible to oxidation; unstable passivation layers, such as Si-O-R, are replaced by the native silicon oxide layer upon exposing to air. To determine the protection against oxidation by the iCVD passivation method, we used XPS and focused on the high resolution Si (2*p*) scan for the presence of oxide peaks on the samples treated with Process A. The film thickness at the end of Process A was estimated to be less than 6 nm based on the information depth in the XPS measurements (~63% of electrons collected are from < 2nm depth into the film; ~30% from 2-4 nm and ~5% from 4-6nm). The representative XPS Si (2*p*) high-resolution scan on the passivated samples after exposure to air is shown in Fig. 1b. The binding energy of SiO_x is ~ 104 eV, while that of non-oxidized silicon is around 100 eV. No significant silicon oxide peak is observed on the iCVD-passivated silicon samples. The double peak around 100 eV is due to the spin orbit splitting of the covalent Si 2*p* (3/2 and 1/2), confirming that the vinyl-functionalized passivation layer is thin enough to permit detection of the silicon wafer substrate.

Following the process A, a poly(ethylene glycol diacrylate) (PEGDA) layer with the thickness of 200 – 700 nm was deposited *in situ* via traditional iCVD polymerization[21] on DD-passivated silicon wafers (denoted as "Process B" in Fig. 4-1a). The roughness of 200 nm-PEGDA coating is ~0.3 nm (Fig. 4-2). The smoothness of the film allows one to control the reflectivity and a passivation-ARC is thus achievable by this simple scheme. The reflection spectra of 200nm PEGDA coatings on passivated Si are shown in Fig. 4-1c, where the reflection is suppressed effectively at the wavelength with the maximum solar irradiance.

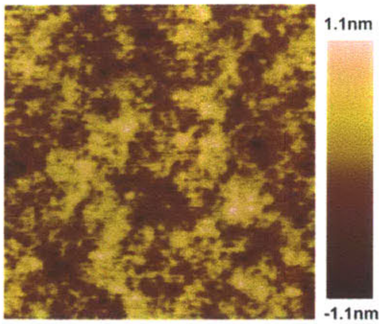

Figure 4-2| AFM image of 200 nm PEGDA film grafted on silicon substrate via iCVD 1,9-decadiene passivation. The RMS roughness is 0.28 ± 0.04 nm.

The PEGDA film is covalently grafted to the silicon substrate through the surface vinyl groups generated by Process A; and nano-scratching tests provide a qualitative evaluation of the strength of this adhesion. We performed a ramping load scratch from 0.01 to 0.5 mN on 660 nm PEGDA-coated samples to observe the possible delamination events. Fig. 4-3a is an image of multiple delamination events that occurred on a non-passivated sample, for which the ARC was grown onto a clean wafer via Process B (i.e., traditional iCVD) in absence of Process A, with only dispersion forces present between the polymer film and the substrate.[13]

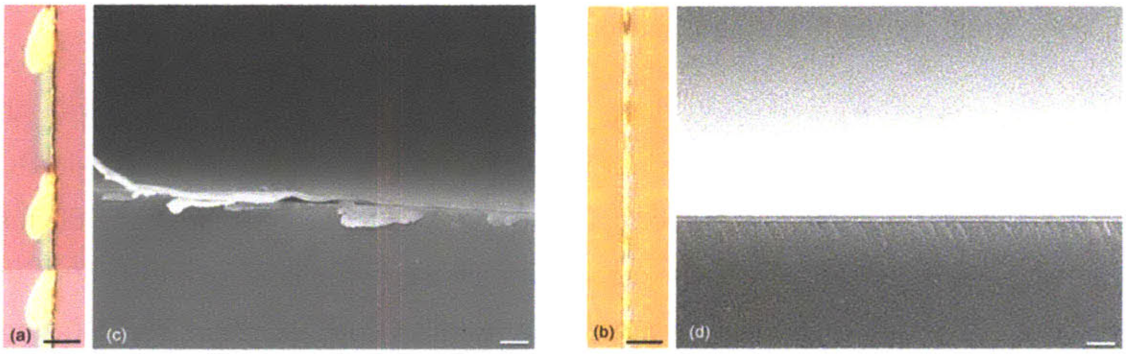

Figure 4-3| (a)-(b) Nano-scratching images and (c)-(d) cross-sectional SEM images of ARC, which is deposited by Process B alone (i.e., traditional iCVD polymerization) in (a) and (c) and a combination of Process A and B in (b) and (d). The spalling of ARC in (a) is due to lack of adhesion to the Si substrate, which is not present in (b), suggesting good adhesion resulted from the passivation interlayer, which is also observed in the cross-sectional SEM images. The scale bars represent 7 μm in (a) and (b) and 1 μm in (c) and (d).

The spiral patterns are indications of poor adhesion to the substrate and delamination of the coating. In the same load range, the scratches on the samples treated with both Process A and B are shown in Fig. 4-3b, where no delamination events were observed. This is an indication of the high coverage and good uniformity of the passivation produced in Process A. The adhesion of the passivation-ARC is also verified by the scanning electron microscope (SEM) imaging (Fig. 4-3c and 4-3d) on the sample cross-section. Delamination of the polymer coating as shown in Fig. 4-3c is common due to the mechanical stretching and tearing during the SEM sample preparation. For the passivated samples, such delamination was not observed (Fig. 4-3d) because the coating was covalently bounded to the substrate.

In addition to the promoting adhesion and protecting devices against oxidation, a high-quality electronic passivation should also reduce the number and cross section of the surface minority charge carrier recombination sites. The rate of the minority carriers' surface recombination is quantified by SRV, which can be calculated from minority carrier lifetime (MCL) measurements using the Quasi-Steady State Photoconductance (QSSPC) technique with Sinton WCT-120 apparatus.[24] The current configuration of the iCVD passivation tool enables only single-sided coating. Thus, to allow the measurement of the MCL at the Si-polymer interface, the back side of each wafer was passivated with a thick (~700 nm) layer of PECVD-grown SiN_x.[6] Therefore, the effective (measured) lifetime is affected by minority carrier recombination at both the back and front surfaces, and the two are decoupled using a common-reference method described forthwith. Following the deposition of the SiN_x coating on one side of the wafer, the wafer was etched with 1% HF solution without removing the SiN_x layer, and treated with 0.1 M E-I solution.[7] The minority carrier lifetime of the E-I passivation was measured instantly. This process captures the bulk and back-surface recombination, which can later be subtracted to extract the effect of the iCVD passivation using the following relation:[7]

$$\frac{1}{\tau_{iCVD}}=\frac{1}{\tau_{I-E}}+\frac{2(S_{iCVD}-S_{I-E})}{d} \tag{4-1}$$

where τ_{iCVD} (or τ_{I-E}) is the effective (measured) lifetime of the iCVD (or E-I) passivation; S is the SRV; and d is the thickness of the wafer. After the measurement, the E-I solution was cleaned off by standard RCA and HF etching procedure. The wafer was transferred into the iCVD chamber within 3 minutes to be treated with Process A followed by Process B.

The average injection-dependent lifetimes for the iCVD passivation and E-I passivation are plotted in Fig. 4-4a. The instant lifetimes after the iCVD passivation are superior to those observed after the E-I passivation at all injection levels, indicating that the iCVD DD passivation is able to achieve <10 cm s^{-1} surface recombination velocities. This is equivalent to, if not better than, the best results for organic passivation of silicon.[9]

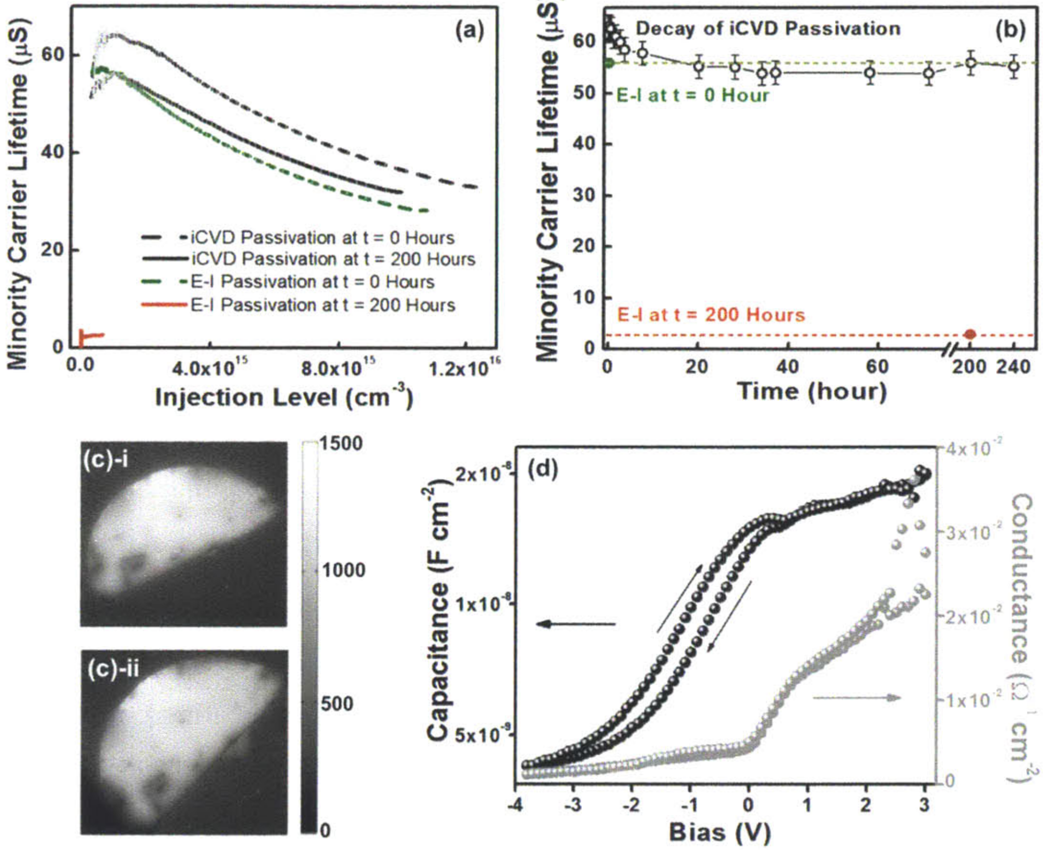

Figure 4-4| (a) Injection-dependent minority carrier lifetimes, and (b) time-dependent decay of lifetimes at the injection level of $\Delta n = 1.0\times10^{15}$ cm^{-3}, of iCVD and E-I passivation. The effective (measured) lifetimes achieved with the iCVD process are superior to those of the E-I treatment. After 200 hours in air, E-I passivation is nonexistent, while the iCVD sample lifetime decays only slightly. (c) Photoluminescence images of (c)-i, as-passivated sample by iCVD method, and (c)-ii, the same sample after 200 hours in lab ambient. The passivation is uniform, and robust in air, indicated by the consistency of both overall signal magnitude and spatial features between two images. (d) Capacitance and conductance of an Al/iCVD PEGDA/n-Si/InGa stack as a function of bias voltage, taken at 30 kHz. The ability to switch the interface state indicates a low defect density (no Fermi level pinning).

The error bars in Fig. 4-4a indicate the standard deviations between two iCVD passivation runs. The passivated samples were kept in the lab ambient for more than 200 hours and a slight decrease in the minority carrier lifetime is observed (Fig. 4-4a and 4-4b). After 200 hours of storage, the lifetimes of iCVD passivation at all injection levels are better than or comparable to the E-I passivation at t = 0 hour. Fig. 4-4b demonstrates the time-dependent decay of lifetimes at the injection level of Δn = 1.0×10^{15} cm^{-3} for both passivation methods. After ~15 hours, the lifetime of the iCVD passivations stablized around 56 μs, which is comparable to the E-I control at t = 0 hour (dotted line in Fig. 4-4b), implying that the surface recombination velocity remains around 10 cm s^{-1}. However, the E-I passivation has un-detectable lifetime after t = 200 hours at the injection level of Δn = 1.0×10^{15} cm^{-3}. The lifetime at the injection level of Δn = 0.7×10^{15} cm^{-3} is plotted in Fig. 4-4b instead, which is around ~3 μs. This observation suggests an excellent quality and stability of the iCVD passivation method.

Camera-based photoluminescence imaging (PLI) [25] evaluates the minority carrier lifetime distribution across the wafer, revealing the surface passivation uniformity. PLI measurements were obtained via s standard measurement practice (see supplemental materials for details).[25] The images (Fig.4-4c-i and -ii) show relatively uniform luminescence across the entire wafer piece, indicating good passivation uniformity. After 200 hours of air exposure, the qualitative features of the PLI measurement as well as the overall intensity remain largely unchanged, further indicating the robustness of the surface passivation.

Finally, one of the many possible applications of the silicon-polymer thin film structure was demonstrated. Parts of a field-effect transistor (FET) device were fabricated using iCVD passivation and tested via capacitance-voltage (C-V) measurements. After Process A and B, 0.28 mm^2 Al pads were evaporated onto the surface of the polymeric layer using a shadow mask. The nitride layer was scratched and an InGa eutectic was used to make a back contact. The capacitance-voltage curve (Fig. 4-4d) shows the characteristic behavior of a Metal-Insulator-Semiconductor (MIS) capacitor structure that can be driven from accumulation to depletion.[26] This indicates the absence of a large density of interfacial states that may pin the Fermi level to a position in the mid-gap of silicon. When the structure is driven into accumulation (positive bias), the Si bands bend downward at the Si-polymer interface, accumulating electrons near it. The measured capacitance is that of the polymer film alone, and conductance is controlled by leakage of electrons through it. When the structure is driven into depletion, the capacitance measured is that of the polymer film and the depletion region. Here, the conductance is further limited by the transport of electrons through the depletion layer, which lengthens with increased bias. A small but noticeable hysteresis is observed, possibly suggesting the presence of a small concentration of charged interface states; perhaps these are the same states that give rise to a finite SRV.

4.5 Conclusion

In conclusion, we demonstrate a strategy of using an iCVD method to passivate a silicon hydride surface and to grow robust organic surface films with several hundred nanometers thickness. Our estimates of the SRV obtained using iCVD-grafted DD are at or below 10 cm s^{-1}, which is comparable to if not lower than the best air-stable organic passivations of Si. Atop this functionalized silicon surface, organic films can be grown to several hundred nanometers thick and exhibit robust adhesion to the silicon surface; iCVD-deposited PEGDA films resist spalling in nano-scratch tests. Preliminary observations suggest air-stable surface passivation up to 200 hours. The simple reaction, commercially available and inexpensive reactants, and relatively mild reaction conditions render it feasible to be incorporated into the existing semiconductor fabrication infrastructure. Our method therefore offers a practical solution to the various problems existing in the fast-developing organic electronics and PV industry. Functionalities other than the vinyl moiety are possible via the iCVD passivation method. No modifications to the passivation procedure should be required for other monomers. Future work will focus on improving the reproducibility, obtaining dual-side iCVD-deposited wafers, conducting strenuous stability tests, and identifying the nature of the molecular layer and the reaction mechanism of the passivation process.

ACKNOWLEDGMENT. This work was supported by Eni S.p.A. under the Eni-MIT Alliance Solar Frontiers Program. We thank Dr. Yaron Segal for his help with XPS, QSSPC, PL and CV measurements.

References

1. Aberle, A. G. *Prog. Photovolt. Res. Appl.* **8,** 473-487, (2000).
2. Shpaisman, H. *et al. Adv. Funct. Mater.* **20,** 2181-2188, (2010).
3. Richards, B. S., Cotter, J. E. & Honsberg, C. B. *Applied Physics Letters* **80,** 1123-1125, (2002).
4. Ciampi, S., Harper, J. B. & Gooding, J. J. *Chem. Soc. Rev.* **39,** 2158-2183, (2010).
5. Cuevas, A., Basore, P. A., Giroult-Matlakowski, G. & Dubois, C. *J. Appl. Phys.* **80,** 3370-3375, (1996).
6. Lauinger, T., Schmidt, J., Aberle, A. G. & Hezel, R. *Appl. Phys. Lett.* **68,** 1232-1234, (1996).
7. Stephens, A. W. & Green, M. A. *Sol. Energ. Mat. Sol. C.* **45,** 255-265, (1997).
8. Kerr, M., J. & Cuevas, A. *Semicond. Sci. Tech.* **17,** 35, (2002).
9. Royea, W. J., Juang, A. & Lewis, N. S. *Appl. Phys. Lett.* **77,** 1988-1990, (2000).
10. Lopinski, G. P., Wayner, D. D. M. & Wolkow, R. A. *Nature* **406,** 48-51, (2000).
11. Koyama, K., Ohdaira, K. & Matsumura, H. *Appl. Phys. Lett.* **97,** 082108-082103, (2010).
12. Spee, D., van der Werf, K., Rath, J. & Schropp, R. *physica status solidi (RRL) – Rapid Research Letters* **6,** 151-153, (2012).
13. Alf, M. E. *et al. Adv. Mat.* **22,** 1993-2027, (2010).
14. Gupta, M. & Gleason, K. K. *Thin Solid Films* **515,** 1579-1584, (2006).
15. Pryce Lewis, H. G., Bansal, N. P., White, A. J. & Handy, E. S. *Thin Solid Films* **517,** 3551-3554, (2009).
16. Yang, R., Xu, J., Ozaydin-Ince, G., Wong, S. Y. & Gleason, K. K. *Chem. Mater.* **23,** 1263-1272, (2011).
17. Yague, J. L. & Gleason, K. K. *Soft Matter* **8,** 2890-2894, (2012).
18. Ozaydin-Ince, G. & Gleason, K. K. *J. Vac. Sci. Technol., A* **27,** 1135-1143, (2009).
19. Xu, J., Asatekin, A. & Gleason, K. K. *Adv. Mater.* **24,** 3692-3696, (2012).
20. Haller, P. D., Frank-Finney, R. J. & Gupta, M. *Macromolecules* **44,** 2653-2659, (2011).
21. Yin, J., Yagüe, J. L., Eggenspieler, D., Gleason, K. K. & Boyce, M. C. *Adv. Mater.*, n/a-n/a, (2012).
22. Brandrup, J., Immergut, E. H. & Grulke, E. A. *Polymer Handbook.* 4 edn, (Wiley-Interscience, New York, 1999).
23. Vilan, A. *et al. Adv. Mater.* **22,** 140-159, (2010).
24. Sinton, R. A. & Cuevas, A. *Appl. Phys. Lett.* **69,** 2510-2512, (1996).
25. Trupke, T., Bardos, R. A., Schubert, M. C. & Warta, W. *Appl. Phys. Lett.* **89,** 044107-044103, (2006).
26. Sze, S., M. & Ng, K., K. *Physics of Semiconductor Devices.* (John Wiley and Sons, New Jersey, 2007).

CHAPTER FIVE

Chlorine-resistant zwitterionic chemistry via iCVD

Reproduced with permission from Petruczok C. D., Yang R., and Gleason K. K., *Macromolecules* **2013**, 46, 1832.

5.1 Abstract

We report the single-step preparation of controllably cross-linked poly(divinylbenzene) (PDVB) and poly(4-vinylpyridine -*co*-divinylbenzene) thin films using initiated Chemical Vapor Deposition (iCVD). Fourier Transform Infrared spectroscopy-based methods for quantifying film composition and degree of cross-linking are elucidated; the validity of these methods is assessed using x-ray photoelectron spectroscopy and nanoindentation, respectively. The extent of reaction of divinylbenzene (DVB) pendant vinyl bonds in homo- and copolymer films is unaffected by changes in initiator concentration, suggesting that bond reactivity, rather than radical concentration, is the limiting factor. Analysis of film step coverage (S) over high aspect ratio (AR) features and sticking probability calculations lend insight into the reactivity of both monomers and explain the extreme conformality of PDVB films ($S = 0.87 \pm 0.02$ at $AR = 4.7$). In addition, the incorporation and cross-linking of DVB moieties in the copolymer is extremely reproducible and can be used to tune the elastic moduli of the films from 3.4 to 5.8 GPa.

5.2 Introduction

Cross-linked polymer networks are used in a variety of essential applications. Cross-linked hydrogels can be used as sensors,[1] cell immobilization platforms,[2] and components in microfluidic devices.[3] Porous cross-linked polymers form catalyst frameworks[4] and capillary columns for separation processes,[5] while cross-linked polymer films have been used as barrier coatings,[6] electroactive layers in organic light-emitting diodes,[7] and stimuli-responsive materials for sensors and other devices.[8] Control of the amount of cross-linker and degree of cross-linking are critical, as they lead to tunable material properties, including glass transition temperature,[9] swelling behavior,[10] and modulus.[11] Unfortunately, cross-linking renders polymeric materials insoluble or intractable, making characterization difficult.[12] Processing--in particular, the preparation of cross-linked thin films—is also challenging. Common techniques for preparing films include post-treating non-cross-linked layers or using confined solution-phase polymerization; these processes are time-consuming and complex, however, and the resulting films often contain residual solvent that can be difficult to fully remove.[13] These solution-based methods also make coating of micro- and nano-scale features difficult, as surface tension effects render the films extremely non-uniform.[14]

These difficulties can be eliminated by using a vapor-phase coating method, such as initiated Chemical Vapor Deposition (iCVD). In this one-step process, vinyl monomer(s) and thermally labile initiator flow into a vacuum chamber (Fig. 5-1). For cross-linked films, at least one monomer possessing two or more vinyl bonds is employed. The reactants pass through an array of heated filaments, and initiator radicals are formed. The filament temperature is controlled such that the vapor-phase monomers remain intact. The initiator radicals and the monomer(s) adsorb onto the substrate, and free radical polymerization and thin film formation occur. iCVD is a low-energy technique; as a result, complete retention of polymer functionality is observed. Since the process is solvent-free, surface tension and de-wetting effects are absent, and the iCVD films conform to the geometry of the underlying substrate. Consequently, substrates that are typically incompatible with solution-based processing methods, including fabric, paper, nanotubes, microparticles, and trenches, have been uniformly coated with iCVD thin films.[14] The absence of solvent also facilitates synthesis of insoluble thin films—including highly cross-linked materials—and copolymers.[14,16]

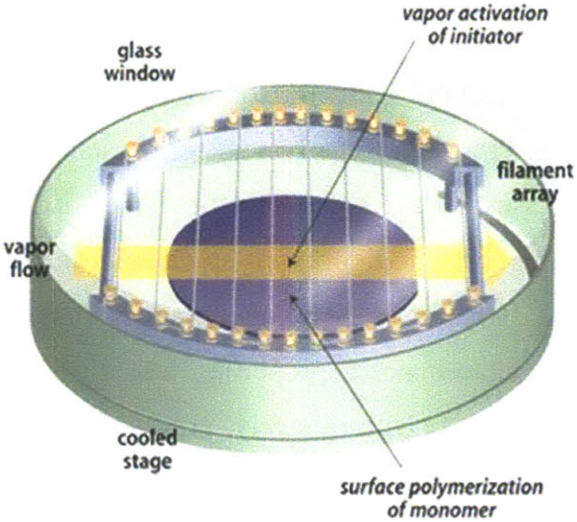

Figure 5-1| Schematic of an iCVD reactor. Monomer(s) and an initiator species pass through a heated filament array, which breaks thermally labile bonds in the initiator. Initiator radicals and monomer adsorb onto the cooled substrate and free radical polymerization occurs.

iCVD has previously been used to create controllably cross-linked films. The deflection of microcantilever sensors coated with poly(maleic anhydride) cross-linked with di(ethylene glycol) divinyl ether was tuned by adjusting the cross-link density of the polymer film.[17] Additionally, the permeability and stability of reverse osmosis membranes functionalized with an antifouling coating were tuned by changing the concentration of cross-linker in the coating.[18] Yagüe and Gleason demonstrated systematic control of mesh size in poly(2-hydroxyethyl methacrylate) hydrogels cross-linked with ethylene glycol diacrylate.[19] Cross-linked iCVD thin films have also been used for a variety of controlled-release applications.[20] In addition, the iCVD process has been used to deposit highly cross-linked organosilicon polymer films useful as biopassive coatings[21] and low-k dielectric materials for the semiconductor industry.[22]

This work reports the first detailed analysis of divinylbenzene (DVB) as an iCVD cross-linker. DVB is an ideal monomer for vapor-phase deposition due to its high volatility and low cost. Plasma-Enhanced Chemical Vapor Deposition (PECVD) has been used to deposit films of poly(divinylbenzene) (PDVB) homopolymer;[23] however, PECVD is an extremely high-energy process in which organic functional groups are often destroyed through side reactions.[14] The energy density of the iCVD process is an order of magnitude lower than that of PECVD.[24] Previously, Asatekin and Gleason used iCVD PDVB to uniformly narrow the pores of high (400-4000) aspect ratio track-etched membranes.[25] This work suggested that iCVD PDVB forms extremely conformal coatings. Here, we perform additional work to characterize the conformality of iCVD PDVB. Additionally, we elucidate a Fourier Transform Infrared (FTIR) spectroscopy-based method that can be used to quantify the degree of cross-linking. DVB has been controllably and quantifiably incorporated into a PDVB homopolymer and a copolymer with 4-vinylpyridine (P(4VP-*co*-DVB)). P(4VP-*co*-DVB) is a common industrial polymer, most notably used as an ion exchange resin,[26] and significant for its insolublity, infusibility, and thermal and chemical stability in a variety of harsh solvents.[27] Tuning of material properties is demonstrated by observing the effect of changes in the degree of cross-linking on the elastic modulus of the copolymer.

5.3 Experimental Section

Synthesis of polymer thin films. Polymer thin films were deposited on 100 mm-diameter silicon wafers (Wafer World, Inc) and silicon wafers with etched trench structures (Analog Devices) using a CVD reactor described elsewhere.[16b] The temperature of the Chromaloy O (Goodfellow) filament array was 205°C for all depositions. The operating pressure was maintained at 800 mTorr using a throttling butterfly valve, and the substrate temperature was 20 °C. Film growth was monitored via *in situ* interferometry with a 633-nm HeNe laser (JDS

Uniphase). All reactants were purchased from Sigma-Aldrich and used as received. Divinylbenzene monomer (DVB) was heated to 65 °C and delivered to the reactor through a needle valve. The certificate of analysis indicated that this monomer consisted of 56.0 mol% *m*-DVB, 25.0 mol% *p*-DVB, and 18.9 mol% ethylvinylbenzene.[28] 4-vinylpyridine (4VP, 95 mol%) and *tert*-butyl peroxide initiator (TBPO, 98 mol%) were delivered using mass flow controllers (MKS Instruments, 1152C and 1479) at 55 °C and ambient temperature, respectively.

Detailed experimental conditions are included in Table 5-1. Depositions of PDVB homopolymer films are referred to as the "H" series. For these depositions, the amount of DVB was held constant, and the flow rate of TBPO varied from 1 to 6 sccm. To ensure the residence time in the reactor was kept constant, a patch flow of Ar was used to maintain a total reactant flow rate of 15 sccm for all depositions. P/P_{sat} is the ratio of the partial pressure of a reactant to its saturation pressure at the substrate temperature and is indicative of surface concentration.[15] The "C" series refers to depositions of P(4VP-*co*-DVB) copolymer with an increasing flow rate of DVB compared to 4VP. C_0 conditions refer to P4VP homopolymer. For the "I" copolymer series, the flow rates of 4VP and DVB were held constant and the amount of TBPO was varied from 1 to 3 sccm.

Table 5-1| Reaction conditions for the PDVB homopolymer and copolymer P(4VP-*co*-DVB)[a]

	4VP		**DVB**		**TBPO**		**Ar**
sample	P/P_{sat}	*flow rate (sccm)*	P/P_{sat}	*flow rate (sccm)*	P/P_{sat}	*flow rate (sccm)*	*flow rate (sccm)*
H series							
H_1	-	-	4.2×10^{-1}	3	2.8×10^{-3}	1	11
H_2	-	-	4.2×10^{-1}	3	8.4×10^{-3}	3	9
H_3	-	-	4.2×10^{-1}	3	1.7×10^{-2}	6	6
C series							
C_0	5.2×10^{-1}	9	-	-	8.4×10^{-3}	3	3
C_1	5.2×10^{-1}	9	7.1×10^{-2}	0.5	8.4×10^{-3}	3	2.5
C_2[b]	5.2×10^{-1}	9	1.4×10^{-1}	1	8.4×10^{-3}	3	2
C_3	5.2×10^{-1}	9	2.1×10^{-1}	1.5	8.4×10^{-3}	3	1.5
I series							
I_1	5.2×10^{-1}	9	1.4×10^{-1}	1	2.8×10^{-3}	1	4
I_2	5.2×10^{-1}	9	1.4×10^{-1}	1	5.6×10^{-3}	2	3
I_3	5.2×10^{-1}	9	1.4×10^{-1}	1	8.4×10^{-3}	3	2

[a] $T_{substrate} = 20°C$, $T_{filament} = 205°C$, and P = 800 mTorr for all depositions.

[b] Note that I_3 and C_2 conditions are the same.

Chemical characterization. Thicknesses of polymer thin films were obtained using a JA Woollam M-2000 variable angle spectroscopic ellipsometer at incident angles of 65, 70, and 75°; data were fit to a Cauchy-Urbach isotropic model using WVASE32 modeling software (JA Woollam). The homogeneity of the films was assessed by using ellipsometry to measure the film thickness at five positions on coated 100 mm-diameter silicon wafers. For both PDVB homopolymer and P(4VP-*co*-DVB), the standard deviation of the measurements was within 6.8% of the mean. The thickness of each 1 cm^2 sample used for FTIR analysis was measured prior to obtaining its spectrum. The average thicknesses of these series of films have been included in the Supporting Information. FTIR spectra were obtained using a Thermo Nicolet Nexus 870 spectrometer operated in transmission mode with a deuterated triglycine sulfate KBr detector. Baseline-corrected spectra were collected over 400-4000 cm^{-1} at 4 cm^{-1} resolution and averaged over 256 scans. Spectra were processed using the OMNIC software package (Thermo Scientific). X-ray photoelectron spectroscopy (XPS) survey scans were obtained using a Kratos Axis Ultra spectrometer equipped with a monochromatic Al Kα source and operated at 150 W. The pass energy and step size for the survey scans were 160 eV and 1 eV, respectively. Samples were stored under vacuum for approximately 12 hours before analysis. Pressure during analysis was maintained under 2×10^{-8} Torr, and the analysis areas were 400×750 μm. The spectra were analyzed using the CasaXPS software package.

Conformality of polymer thin films. The conformality of the thin films was assessed by depositing 350 nm-thick films on silicon wafers with etched trench structures of different aspect ratios. The films were imaged using JEOL 6060 and Hitachi TM-3000 scanning electron microscopes. Film thicknesses at the top and bottom of the trenches were measured for three trenches of each aspect ratio using MeasureIT software (ResAlta).

Nanoindentation. A TI-900 TriboIndenter (Hysitron) was used for the nanoindentation experiments. The indentation axis calibration was performed in air with a triangular load function (10 s time segments, 700 μN peak load). Seven indents were made in the shape of an "H" on a standard aluminum sample to determine the offset between the optics and the indenter probe (H calibration). For the iCVD film samples, the load function for the H calibration was adopted from Lee.[29] A conical diamond indenter tip (Young's modulus = 1140 GPa, Poisson's ratio = 0.07) with a radius of 10 μm was used during all indentations. The area function of the diamond tip can change over time and, thus, was determined experimentally by indenting a fused silica standard sample with a Young's modulus of 72 GPa and Poisson's ratio of 0.17 (reduced modulus = 69.6 GPa). The area function was fitted with a polynomial model.

The polymer films used in the nanoindentation experiments were approximately 1 μm thick, and a maximum indentation depth of 90 nm was used to eliminate the possibility of substrate effects.[30] A 7×7 grid was used during the indentation of iCVD polymer films, with 6 μm separation in both directions between indentations. Therefore, 49 indentations were performed on each sample and an area of 1296 μm^2 was probed. 8192 values of indentation depth were used and the corresponding indent forces were measured during each indentation. The load function for iCVD film samples contained 3 segments with segment times of 10 s, 5 s, and 10 s and a peak depth of 90 nm.

5.4 Results and Discussion

5.4.1 Characterization of poly(divinylbenzene)

Structures of the DVB isomers and possible types of DVB repeat units in the homopolymer are included in Fig. 5-2a and 5-2b, respectively. FTIR spectra of the DVB monomer and iCVD PDVB are shown in Fig. 5-3a.

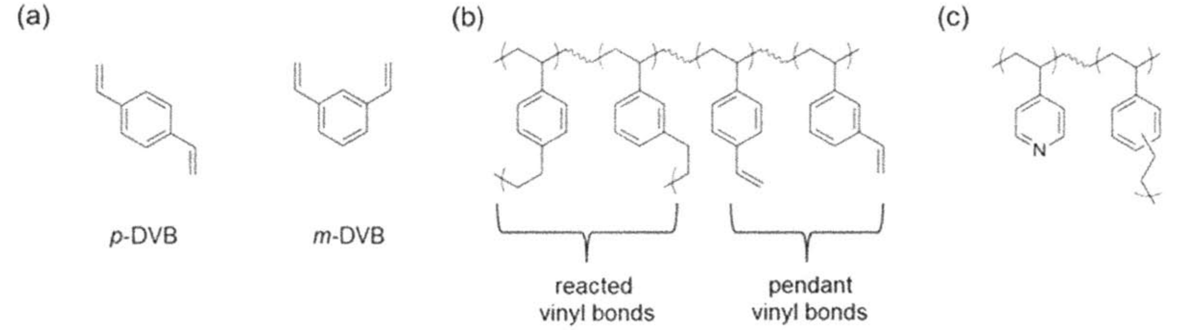

Figure 5-2| Structures of (a) DVB monomers, (b) possible types of DVB repeat units, and (c) P(4VP-*co*-DVB).

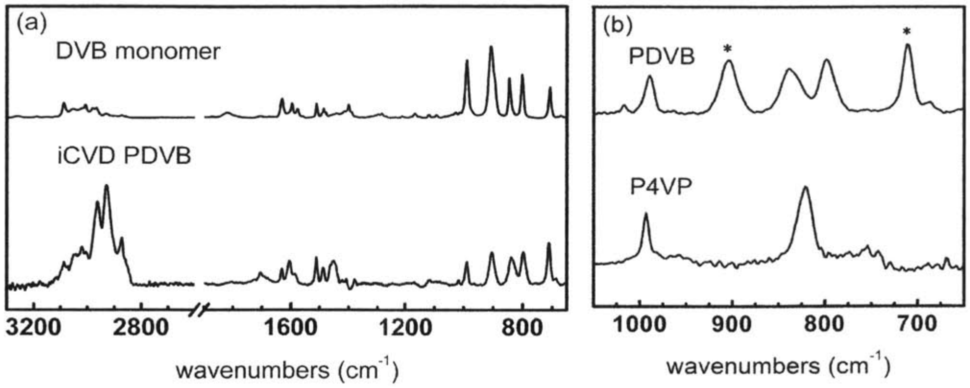

Figure 5-3| (a) FTIR spectra of the DVB monomer and iCVD PDVB confirms polymerization has occurred. (b) FTIR spectra of PDVB and P4VP homopolymers show convolution of peaks commonly used to quantify pendant vinyl bonds. Peaks at 710 and 903 cm^{-1} used in this analysis are marked with asterisks.

Successful polymerization of the homopolymer is confirmed by the reduction of the peak at 903 cm^{-1} in the PDVB spectrum. This peak results from CH_2 out-of-plane deformation in unreacted vinyl groups; its post-polymerization existence is due to the presence of pendant vinyl bonds.[31] Strong peaks at 2870, 2930, and 2960 cm^{-1} are also observed in the PDVB spectrum and are due to symmetric sp^3 CH_3, asymmetric sp^3 CH_2, and asymmetric sp^3 CH_3 stretching in the backbone of the newly-formed polymer chain.[32] Excellent agreement is observed between spectra of iCVD and solution-polymerized PDVB,[33] indicating that the non-vinyl organic functionality in the monomer is retained in the iCVD film. This confirms that the monomer is not altered by the heated filaments during the vapor deposition process. For this work, samples of various thicknesses (150 nm to 1 μm) were prepared; given processing time and measurement considerations, reasonable bounds on PDVB film thickness are 15 nm to 5 μm.

5.4.2 Degree of cross-linking in poly(divinylbenzene) homopolymer

FTIR spectra were used to quantify the percentage of DVB repeat units whose vinyl bonds have reacted to form cross-links--that is, those without pendant vinyl bonds (Fig. 5-2b)--as well as the mole fraction of 4VP incorporated into the copolymers. From these quantities, the degree of cross-linking can be obtained. Existing techniques for quantifying pendant vinyl bonds in PDVB have utilized vinyl bond peaks at 1630 and 990 cm^{-1}, as well as peaks at 1510 and 795 cm^{-1} resulting from *p*- and *m*-substituted aromatic rings.[34] The vinyl peak at 903 cm^{-1} and the *p*-substituted aromatic peak at 837 cm^{-1} have also been used.[11a, 31b, 35] These existing methods are not easily applied to P(DVB-*co*-P4VP), as characteristic DVB peaks are often obscured by those of 4VP (Fig. 5-3b). The vinyl peak at 990 cm^{-1} in the PDVB spectrum is convoluted by the peak at 993 cm^{-1} in the P4VP spectrum, caused by stretching of the pyridine rings.[36] Quantification of the peaks at 795 and 837 cm^{-1} in the PDVB spectrum is also made difficult by the presence of a strong peak at 820 cm^{-1} in the P4VP spectrum resulting from out-of-plane deformation of the pyridine rings.[37]

To quantify the degree of cross-linking in PDVB samples, the area under the peak at 903 cm^{-1} was measured and compared to the area under the peak at 710 cm^{-1} (Fig. 5-3b). The peak at 903 cm^{-1} is indicative of the number of pendant vinyl bonds, while the peak at 710 cm^{-1}, resulting from C-C vibration in the phenyl moieties, is a measure of the number of *m*-substituted aromatic rings.[38] In order to analyze the PDVB samples, the presence of a small quantity (18.9 mol%) of ethylvinylbenzene (EVB) in the commercial monomer mixture must be considered. By temporarily considering the PDVB homopolymer as a "copolymer" of DVB and EVB impurity and using the Fineman-Ross copolymerization equation (adapted for polymerization on surfaces), we find that the amount of EVB impurity incorporated into the PDVB homopolymer samples is equivalent to the amount present in the monomer. Details of this analysis are included in the Supporting Information.

The Beer-Lambert equation relates absorbance, A, to absorptivity, a, pathlength, b, and concentration, c:[39]

$$A = abc \qquad (5\text{-}1)$$

Absorptivity can be described as a proportionality constant between absorbance and concentration and is a physical property for a specific molecule and wavenumber.[39] For known concentrations and absorbance of *m*- and *p*-substituted aromatic rings, a ratio of absorptivities, a_m/a_p, can be determined using the following equation:

$$\frac{a_m}{a_p} = \left(\frac{c_p A_m}{c_m A_p}\right)_{monomer} = \frac{x_p}{x_m}\left(\frac{A_m}{A_p}\right)_{monomer} = \left(\frac{x_{p,DVB}+x_{p,EVB}}{x_{m,DVB}+x_{m,EVB}}\right)\left(\frac{A_m}{A_p}\right)_{monomer} \qquad (5\text{-}2)$$

Here, A_m and A_p signify the absorbance of *m*- and *p*-substituted aromatic rings, which are obtained by measuring the areas under the peaks at 710 and 1510 cm^{-1}, respectively, in the monomer spectrum.[39] x_p and x_m are the mole fractions of *p*- and *m*-substituted aromatic rings in the monomer, and have contributions from both DVB and EVB repeat units ($x_{m,DVB}$,, $x_{p,DVB}$, $x_{m,EVB}$, and $x_{p,EVB}$). Pathlength has been canceled from the equation because components being considered are part of the same sample. $x_{m,DVB}$ and $x_{p,DVB}$ were provided by Sigma-Aldrich, as noted in the Experimental Section. The ratio of *m*- to *p*-EVB in the monomer was assumed to be identical to the ratio of *m*- to *p*-DVB based on the similarity of the molecular structures. Substituting in the mole fractions ($x_{m,DVB} = 0.560$, $x_{p,DVB} = 0.250$, $x_{m,EVB} = 0.106$, and $x_{p,EVB} = 0.047$), and the value of 3.46 measured for $(A_m/A_p)_{monomer}$, we calculate a value of 1.54 for a_m/a_p. The ratios of *m*- and *p*-substituted repeat units in the H series of samples were calculated using the following equation (for a set of reaction conditions, H_n, n=1-3):

$$\left(\frac{y_m}{y_p}\right)_{H_n} = \left(\frac{a_p}{a_m}\right)\left(\frac{A_m}{A_p}\right)_{H_n} = \frac{1}{1.54}\left(\frac{A_m}{A_p}\right)_{H_n} \qquad (5\text{-}3)$$

Here, y_m and y_p are the mole fractions of *m*- and *p*-substituted repeat units in the polymer film. A_m and A_p are the areas under the 710 and 1510 cm^{-1} peaks in the FTIR spectrum of the polymer sample. Values of y_m/y_p for the H series of polymer films (average=1.75) were consistently less than x_m/x_p for the monomer (2.24); this implies lower reactivity of the major component, *m*-DVB, compared to the other major component, *p*-DVB, in agreement with previous results.[34, 40]

The mole fraction of *m*-substituted DVB in the H series of polymer films, $y_{m,DVB}$, can be calculated using:

$$\left(y_{m,DVB}\right)_{H_n} = \left(\frac{y_{m,DVB}}{y_{m,DVB}+y_{p,DVB}}\right)_{H_n}\left(x_{m,DVB}+x_{p,DVB}\right) = \left(1 - \frac{1}{\frac{1}{1.54}\left(\frac{A_m}{A_p}\right)_{H_n}+1}\right)\left(x_{m,DVB}+x_{p,DVB}\right) \qquad (5\text{-}4)$$

We note that this equation uses A_m and A_p, which are obtained by measuring the areas under the peaks at 710 and 1510 cm^{-1}. These values contain small contributions from EVB since the peaks corresponding to the aromatic rings of DVB and EVB are not easily differentiable. The ratio of *m*- to *p*-EVB in the film is assumed to be comparable to the ratio of *m*- to *p*-DVB; this assumption is reasonable because EVB is a minority component, and the propagation rate constants of the isomeric species do not differ dramatically.[40b]

Once the percentage of *m*-substituted DVB in the homopolymer has been accounted for, the percentage of DVB pendant vinyl bonds that have reacted to form cross-links, $\%_R$, is calculated:

$$(\%_R)_{H_n} = \left(1 - \frac{(y_v)_{H_n}}{x_{DVB}}\right) \times 100 = \left[1 - \left(\frac{2\left(\frac{A_v}{A_m}\right)_{H_n}}{\left(\frac{A_v}{A_m}\right)_{monomer}} \frac{(y_{m,DVB})_{H_n}}{x_{m,DVB}}\right)\right] \times 100 \qquad (5\text{-}5)$$

Here, A_v is the area under the vinyl bond peak at 903 cm^{-1}. The DVB monomer was used as an internal standard for rings with two pendant vinyl bonds; the pre-factor of 2 used in eq 5-5 accounts for the fact that DVB repeat units incorporated into the homopolymer have, at most, one pendant vinyl bond. A linear decrease in the area under the 903 cm^{-1} peak upon reaction of the second vinyl bond in each DVB repeat unit is assumed, in accordance with eq 5-1. Finally, the degree of cross-linking, $\%_X$, can be defined as:

$$\%_X = \frac{N_r}{N_{total}} \times 100 \qquad (5\text{-}6)$$

where N_r is the number of DVB repeat units without a pendant vinyl bond and N_{total} is the total number of repeat units. For "pure" PDVB homopolymer samples, $\%_X$ should be equivalent to $\%_R$. However, due to the presence of EVB, $\%_X = (\%_R)\,(y_{DVB})$. Results for the degree of cross-linking in the H series are included in Fig. 5-4 (in parentheses).

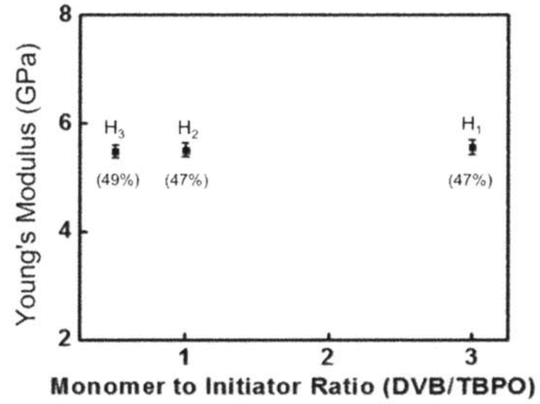

Figure 5-4| The elastic moduli of samples H_1-H_3 are the same, indicating a similar degree of cross-linking for all samples, despite the different initiator concentrations used. The degree of cross-linking is calculated using FTIR spectra of the monomer and homopolymer samples; these results, shown in parentheses, also have limited variability.

The calculated values for $\%_X$ indicate that the degree of cross-linking does not change with initiator concentration in the range of flow rates used. This suggests that the ability to polymerize the pendant vinyl bonds is not limited by radical concentration but by bond reactivity. An estimation of the time required for initiator radicals to diffuse through the polymer film further supports this conclusion.

We note that the values reported in Fig. 5-4 were calculated using eq 5-5. The pre-factor of 2 used in this equation assumes that each molecule present in the commercial DVB monomer contains two vinyl bonds; this neglects the presence of EVB. The Fineman-Ross analysis used to investigate the concentration of EVB in the H series of films can be used to calculate the extent to which EVB incorporation lowers the value of this pre-factor. Based on this analysis, we find the average absolute error on the $\%_R$ calculations in PDVB as a result of neglecting the effect of EVB on the pre-factor is approximately 3.9%.

To further verify the degrees of cross-linking in the H series, we used nanoindentation to measure the elastic moduli, which are typically proportional to $\%_X$. A 10 μm conical diamond tip was used to indent the iCVD films and the area function of the tip was determined experimentally by indenting a standard fused silica sample with known mechanical properties. The reduced moduli were calculated from the load-displacement curves with the following equation:[41]

$$E_r = \frac{U\sqrt{\pi}}{2\sqrt{A(h_c)}} \tag{5-7}$$

where U is the initial unloading contact stiffness (the slope of the initial portion of the unloading curve), and $A(h_c)$ is the projected contact area at a contact depth of h_c. The reduced moduli (eq 5-7) relate to the elastic moduli of the tested samples, E, through the following equation:[41]

$$\frac{1}{E_r} = \left(\frac{1-\nu^2}{E}\right)_{sample} + \left(\frac{1-\nu^2}{E}\right)_{indenter} \tag{5-8}$$

where ν is the Poisson's ratio. For a standard diamond indenter probe, $E_{indenter}$ is 1140 GPa and $\nu_{indenter}$ is 0.07.[42] We used a value of $\nu = 0.5$ for the sample films, which is commonly accepted for polymeric materials.[43] The elastic modulus of the sample can be calculated from eqs 5-7 and 5-8 and the load-displacement curve. The elastic moduli of the samples from H series (Fig. 5-4) are identical within experimental error, supporting the validity of the FTIR method used to quantify extent of reaction of the DVB pendant vinyl bonds.

5.4.3 Poly(divinylbenzene) content and degree of cross-linking in copolymers.

The structure of P(4VP-*co*-DVB) is included in Chart 1c; the DVB repeat units can take the form of any of the structures shown in Fig. 5-2b. Successful copolymerization was confirmed by comparing FTIR spectra of films before and after treatment with ethanol, which is a good solvent for P4VP homopolymer (Fig. 5-5).

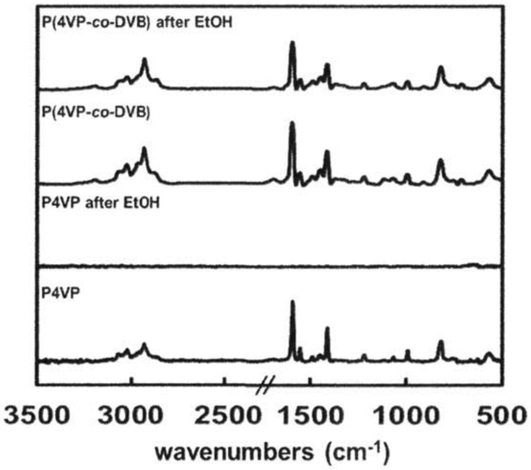

Figure 5-5| FTIR spectra of iCVD P4VP and P(4VP-*co*-DVB) before and after soaking in ethanol (EtOH). The homopolymer film is fully soluble in EtOH, as indicated by the absence of representative peaks. The spectra of the as-deposited and EtOH-soaked copolymer samples are virtually identical. Peaks corresponding to sp^3 CH$_2$ stretching in the polymer backbone are unchanged, as are peaks at 1597, 1557, 1493, 1453, and 1415 cm^{-1}, assigned to vibration of the pyridine rings.[9,10] The lack of change observed in the spectrum of the solvent-treated P(4VP-*co*-DVB) sample indicates that successful copolymerization has occurred.

The overall degree of cross-linking, $\%_X$, was calculated for the copolymer films by multiplying the mole fraction of DVB in the copolymer, y_{DVB}, by the percentage of the DVB pendant vinyl bonds that have reacted, $\%_R$. For the C series, $\%_R$ was calculated using eq 5-5. For these calculations, $y_{m,DVB}/x_{m,DVB}$ of the copolymer was assumed to be the same as that of the homopolymer, where $y_{m,DVB}$ represents the mole fraction of *m*-DVB in the copolymer and $x_{m,DVB}$ represents the mole fraction of *m*-DVB in the vapor phase monomers, including 4VP, DVB and EVB; the average value derived from the H series results is used here.

The mole fraction of 4VP in the C series of copolymer samples, y_{4VP}, was calculated using eq 5-9:

$$(y_{4VP})_{C_n} = \left(1 - \left(y_m + y_p\right)_{C_n}\right) = \left(1 - \frac{(y_m)_{C_n}}{(y_m)_{H_n}}\right) = \left(1 - \frac{(A_m)_{C_n}}{(A_m)_{H_n}}\right) \tag{5-9}$$

Here, $(A_m)_{C_n}$ is the area under the peak at 710 cm^{-1} for each set of conditions in the C series (n=1-3). $(A_m)_{H_n}$ is the average area under the peak at 710 cm^{-1} for the H series of homopolymer. $\%_X$ is then calculated as:

$$(\%_X)_{C_n} = [\%_R \cdot (1 - y_{4VP})]_{C_n}\left(1 - (x_{EVB})_{H_n}\right) \tag{5-10}$$

assuming the amount of EVB relative to DVB in the copolymer is comparable to that in the homopolymer. The resulting values for $\%_R$, y_{4VP}, and $\%_X$ are shown in Table 5-2.

Table 5-2| Results for 4VP incorporation and degree of cross-linking in the C series of P(4VP-*co*-DVB)

	y_{4VP}[a]	$\%_R$[a]	$\%_X$[a]	y_{4VP} (XPS)[b]
C_1	0.912 ± 0.016	78.9 ± 6.8	5.6 ± 0.6	0.929 ± 0.023
C_2	0.836 ± 0.005	69.1 ± 4.8	9.2 ± 0.9	0.815 ± 0.023
C_3	0.740 ± 0.040	53.4 ± 1.3	11.3 ± 2.0	0.693 ± 0.023

[a] Results calculated from FTIR spectroscopy-based method; reported error is standard deviation.

[b] Results calculated from XPS survey scans; reported error is obtained by varying the borders of the fitting regions and calculating the absolute area changes when different endpoints were selected.

As expected, 4VP content in the copolymer decreases as the flow rate of DVB increases. This trend is observable in the FTIR spectra of the C series (Fig. 5-6a). Peaks due to vinyl bonds (903 cm^{-1}) and *m*-substituted aromatic rings (710 cm^{-1}) are undetectable in the spectrum of the P4VP homopolymer (C_0), and increase in intensity as the flow rate of DVB monomer is increased from 0 to 1.5 sccm. The results for y_{4VP} calculated using the FTIR spectroscopy-based method were reproducible over multiple trials and are in excellent agreement with results determined using XPS. Sample XPS survey scans and high resolution C (1s) and N (1s) scans are included in the Supporting Information, as are details of the composition calculations. The agreement of the results validates the use of the FTIR spectroscopy-based method. As the DVB flow rate--and consequently, the amount of DVB incorporated into the copolymer--increase, $\%_R$ decreases. This can be attributed to the difference in reactivity between the available monomeric vinyl bonds and the pendant vinyl bonds of DVB.[44] Fig. 5-6b shows the increase in degree of cross-linking with increasing feed concentration of DVB monomer.

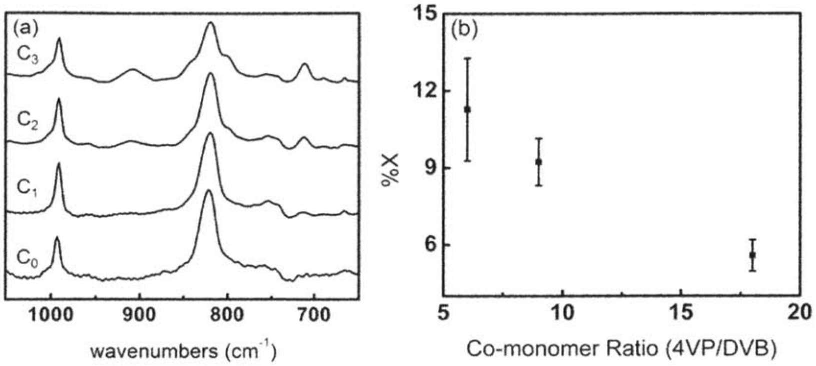

Figure 5-6| (a) FTIR spectra of C series of P(4VP-*co*-DVB). Peaks at 710 and 903 cm^{-1} increase with DVB monomer flow rate. (b) Degree of cross-linking, $\%_X$, as a function of co-monomer ratio.

The results for the I series of copolymer were calculated using the same method as the C series. Results for y_{4VP}, $\%_R$, and $\%_X$ are shown below in Table 5-3.

Table 5-3| Results for 4VP incorporation and degree of cross-linking in the I series of P(4VP-*co*-DVB)

	$y_{4VP}{}^a$	$\%_R{}^a$	$\%_X{}^a$	y_{4VP} *(XPS)*
I_1	0.835	63.9	8.6	0.815
I_2	0.825	68.0	9.7	0.815
I_3	0.825	65.4	9.3	0.793

[a] Results calculated from FTIR spectroscopy-based method.

The amount of DVB incorporated into the copolymer does not change with initiator concentration for the range of flow rates tested. As for the C series, the results obtained using the FTIR spectroscopy analysis agree well with XPS results. As a further check, we note that the results for the I_3 and C_2 series are in good agreement; this is to be expected since the reaction conditions are the same (Table 5-1). The similarity of the results for $\%_R$ and $\%_X$ across the range of conditions suggests that as for the H series, the lower reactivity of the second vinyl bond, not radical concentration, is the limiting factor in creating cross-links.

5.4.4 Sticking probability calculations

The reactivity of the DVB and 4VP monomers can be further assessed by calculating the sticking probability of each monomer. For iCVD polymerization, the sticking probability is the probability that an initiator radical chemisorbs to an adsorbed monomer on the surface and reacts to form a polymer chain. This probability is directly related to the monomer surface concentration. The conformality of the deposition is also correlated with the sticking probability, in that a lower sticking probability will result in a more conformal coating. For a detailed discussion of sticking probability calculations for iCVD films, the reader is directed to the work by Baxamusa and Gleason.[45] In short, sticking probability, Γ, is calculated using the following equation:

$$\ln(S) = -0.48\Gamma\left(\frac{L}{w}\right)^2 \tag{5-11}$$

in which L and w are the length and width, respectively, of a high-aspect ratio (AR) feature such as a trench. S is the step coverage of the polymer film over this feature, here measured as the thickness of the iCVD film at the bottom of the trench divided by the thickness of the film at the top of the trench. Excellent step coverage was observed for both the homo- and copolymer films. For depositions of PDVB homopolymer (H_2 conditions), the average S in trenches of AR=4.7 was 0.87 ± 0.02. For P4VP homopolymer (C_0), S = 0.84 ± 0.02 (AR=3.4), and for P(4VP-*co*-DVB) (C_2), S = 0.73 ± 0.03 (AR=4.4). Fig. 5-7a shows average results used to calculate sticking probability for depositions of these films on trenches of three different aspect ratios (Fig. 5-7b through d). Results for sticking probability are shown in Table 5-4.

Table 5-4| Sticking probability, total P_m/P_{sat}, and reactivity factor for PDVB, P4VP, and P(4VP-*co*-DVB) depositions

	Γ^a	$P_m/P_{sat}{}^b$	R
H_2	0.009 ± 0.006	0.42	0.021
C_0	0.018 ± 0.003	0.52	0.035
C_2	0.022 ± 0.009	0.66	0.033

[a] Error represents 95% confidence interval.

[b] Sum of P_m/P_{sat} for 4VP and DVB.

In order to compare the reactivity of the DVB and 4VP monomers, a linear relationship may be assumed between the total P_m/P_{sat} and sticking probability, based on the results of Baxamusa and Gleason.[46] A reactivity factor, R, can be defined as the calculated sticking probability divided by the total P_m/P_{sat} of the co-monomers. These values, included in Table 5-4, indicate that the DVB monomer is less reactive than 4VP. This conclusion is supported with kinetic data from solution free-radical polymerization; the propagation rate constant (k_p) of 4VP (12 L/mol·s at 25 °C)[47] is approximately twice that of DVB (~6.5 L/mol·s at 25 °C),[48] assuming that the pre-exponential factor for DVB is similar to that of styrene.[49] The low sticking probability and reactivity factor observed for DVB support the extreme conformality of PDVB coatings noted by Asatekin and Gleason.[25] The *R* observed for the copolymer deposition is understandably closer to that of 4VP, which is the majority component and the more reactive monomer.

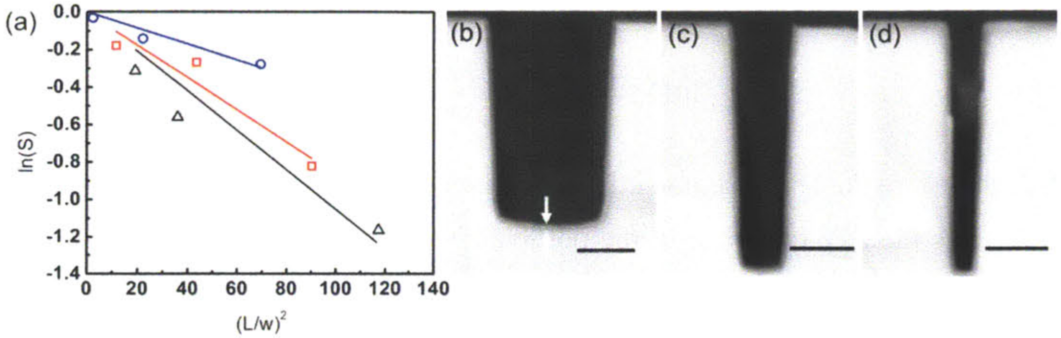

Figure 5-7| (a) Step coverage versus aspect ratio data for (○) PDVB, H_2 conditions; (□) P4VP, C_0 conditions; and (Δ) P(4VP-*co*-DVB), C_2 conditions used to calculate sticking probability and evaluate reactivity. (b)-(d) Trenches of three different aspect ratios coated with H_2 PDVB. Scale bars represent 2 μm; arrows in (b) indicate the thickness of the coating on the bottom of the trench.

5.4.5 Tuning mechanical properties via degree of cross-linking

The results of the FTIR spectroscopy and sticking probability analyses were used to investigate the correlation between the film composition and elastic modulus. Fig. 5-8a illustrates the change in elastic modulus as the transition is made from P4VP homopolymer (co-monomer ratio=∞) to PDVB homopolymer (co-monomer ratio=0).

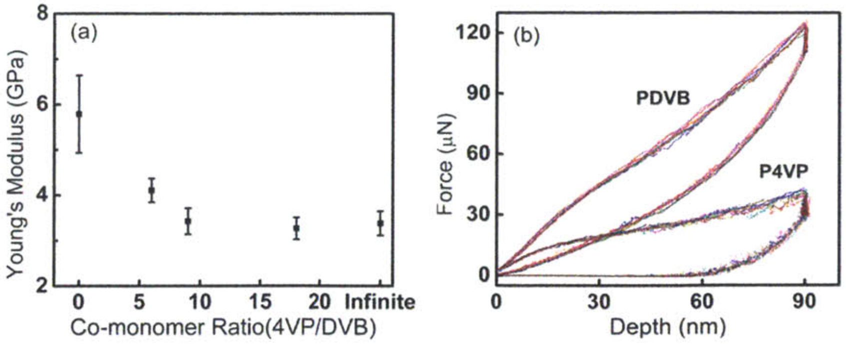

Figure 5-8| (a) Nanoindentation data indicate that the elastic modulus of P(4VP-*co*-DVB) increases with increasing DVB concentration. (b) Force-depth curves indicate that P4VP is more plastic than PDVB.

The modulus of the PDVB homopolymer is greater than that of the copolymer samples. This can be attributed to the fact that the degree of cross-linking is also much higher for the homopolymer (Fig. 5-4); the comparatively low degrees of cross-linking observed in the copolymer samples (Tables 5-2, 5-3) are the result of the presence of large amounts of more reactive 4VP monomer in the feed. This monomer contains no cross-linking functionality. By increasing the amount of DVB in the feed, it is possible to adjust the modulus of the copolymer between 3.4 (P4VP) and 5.8 GPa (PDVB) simply by tuning the flow rates of the monomers.

Fig. 5-8b lends insight into the differences in mechanical properties for P4VP and PDVB films. During the nanoindentation experiments, 49 indentations were generated on each sample to ensure the elastic moduli were statistically representative, and, therefore, 49 load-displacement curves were obtained for each polymer sample. Eight out of the 49 curves are shown as examples in Fig. 5-8b for P4VP and PDVB. From Fig. 5-8b it can be concluded that the elastic moduli are extremely reproducible as the load-displacement curves overlap within each sample. It is worth noting that P4VP is more plastic than PDVB, which is evidenced by the unloading segments of the load-displacement curves. For PDVB, the force decreases to 0 μN only when the indentation depth becomes 0 nm. This indicates there is no detectable plastic deformation. Conversely, for P4VP, the force reduces to 0 μN at indentation depths between 44 nm to 57 nm, implying significant plastic deformation occurs during indentation. The modulus of iCVD P4VP agrees well with the modulus of poly(4-vinylpyridine) polymerized using solution methods.[50] The modulus of iCVD PDVB is higher than published results for solution-polymerized PDVB; this can be attributed to the high degree of cross-linking observed in the vapor-deposited films.[11,31,51]

5.5 Conclusion

iCVD was used to deposit highly conformal thin films of cross-linked PDVB. Degree of cross-linking was quantified via a FTIR spectroscopy-based method and empirically confirmed by measuring the elastic moduli of the films. The degree of cross-linking did not change with initiator concentration, suggesting that the reactivity of DVB pendant vinyl bonds, rather than initiator radical concentration, is the limiting factor. FTIR spectroscopy was also used to quantify 4VP content and degree of cross-linking in P(4VP-*co*-DVB) films. The 4VP content in the copolymer decreased as DVB monomer feed rate increased and was verified by XPS. The percentage of reacted pendant vinyl bonds decreased with increasing DVB feed rate; however, the degree of cross-linking in the film increased due to the higher DVB content. Initiator feed rate had no effect on degree of cross-linking in the range tested. Sticking probability calculations indicated that the DVB monomer is less reactive than 4VP; these results support prior work demonstrating the extreme conformality of PDVB coatings. Finally, we note that DVB incorporation and cross-linking were reproducible and could be used to tune the modulus of the copolymer. Deposition parameters and quantification methodology detailed in this work can be used to extend the use of DVB as an iCVD cross-linking molecule and will be used to synthesize custom thin films for a variety of applications.

ACKNOWLEDGMENT. The authors thank Dr. Ed Gleason of Analog Devices for providing the trench structures and Dr. Ayse Asatekin for helpful discussions. We thank Jonathan Shu from Cornell Center for Materials Research (CCMR) for assistance with XPS measurements, and Ernesto Martinez for his help acquiring ellipsometry measurements and FTIR spectra. This work was supported in part by the MIT Institute for Solider Nanotechnologies (ISN) under Contract DAAD-19-02D-002 with the U.S. Army Research Office, and in part by a National Science Foundation Graduate Research Fellowship (to CDP). The authors would also like to thank the King Fahd University of Petroleum and Minerals (KFUPM) in Dhahran, Saudi Arabia, for funding support through the Center for Clean Water and Clean Energy at MIT and KFUPM.

References

1. Richter, A.; Paschew, G.; Klatt, S.; Lienig, J.; Arndt, K.-F.; Adler, H.-J. *Sensors* **2008**, *8*, 561-581.
2. Jen, A. C.; Wake, M. C.; Mikos, A. G. *Biotechnol. Bioeng.* **1996**, *50*, 357-364.
3. (a) Seong, G. H.; Zhan, W.; Crooks, R. M. *Anal. Chem.* **2002,** *74*, 3372-3377. (b) Hatch, A.; Hansmann, G.; Murthy, S. K. *Langmuir* **2011,** *27*, 4257-4264.
4. Xie, Z.; Wang, C.; de Krafft, K. E.; Lin, W. *J. Am. Chem. Soc.* **2011,** *133*, 2056-2059.
5. Nischang, I.; Teasdale, I.; Brüggemann, O. *Anal. Bioanal. Chem.* **2011,** *400*, 2289-2304.
6. (a) Xu, J.; Asatekin, A.; Gleason, K. K. *Adv. Mater.* **2012,** *24*, 3692-3696. (b) Riche, C. T.; Marin, B. C.; Malmstadt, N.; Gupta, M. *Lab Chip* **2011,** *11*, 3049-3052.
7. (a) Gu, C.; Fei, T.; Lv, Y.; Feng, T.; Xue, S.; Lu, D.; Ma, Y. *Adv. Mater.* **2010,** *22*, 2702-2705. (b) Zuniga, C. A.; Barlow, S.; Marder, S. R. *Chem. Mater.* **2010,** *23*, 658-681.
8. Tokarev, I.; Motornov, M.; Minko, S. *J. Mater. Chem.* **2009,** *19*, 6932-6948.
9. (a) Roland, C. M. *Macromolecules* **1994,** *27*, 4242-4247. (b) Shefer, A.; Gottlieb, M. *Macromolecules* **1992,** *25*, 4036-4042.
10. (a) Eichenbaum, G. M.; Kiser, P. F.; Dobrynin, A. V.; Simon, S. A.; Needham, D. *Macromolecules* **1999,** *32*, 4867-4878. (b) Oh, K. S.; Oh, J. S.; Choi, H. S.; Bae, Y. C. *Macromolecules* **1998,** *31*, 7328-7335.
11. (a) Rackley, F. A.; Turner, H. S.; Wall, W. F. *Nature* **1973,** *241*, 524-525. (b) Schneider, A.; Francius, G.; Obeid, R.; Schwinté, P.; Hemmerlé, J.; Frisch, B.; Schaaf, P.; Voegel, J.-C.; Senger, B.; Picart, C. *Langmuir* **2005,** *22*, 1193-1200.
12. Cormack, P. A. G.; Elorza, A. Z. *J. Chromatogr. B* **2004,** *804*, 173-182.
13. Chan, K.; Gleason, K. K. *Langmuir* **2005,** *21*, 8930-8939.
14. Alf, M. E.; Asatekin, A.; Barr, M. C.; Baxamusa, S. H.; Chelawat, H.; Ozaydin-Ince, G.; Petruczok, C. D.; Sreenivasan, R.; Tenhaeff, W. E.; Trujillo, N. J.; Vaddiraju, S.; Xu, J.; Gleason, K. K. *Adv. Mater.* **2010,** *22*, 1993-2027.
15. Lau, K. K. S.; Gleason, K. K. *Macromolecules* **2006,** *39*, 3688-3694.
16. (a) Lau, K. K. S.; Gleason, K. K. *Thin Solid Films* **2008,** *516*, 678-680. (b) Tenhaeff, W. E.; Gleason, K. K. *Langmuir* **2007,** *23*, 6624-6630. (c) O'Shaughnessy, W. S.; Marí-Buyé, N.; Borrós, S.; Gleason, K. K. *Macromol. Rapid Commun.* **2007,** *28*, 1877-1882.
17. Arora, W. J.; Tenhaeff, W. E.; Gleason, K. K.; Barbastathis, G. *J. Microelectromech. Syst.* **2009,** *18*, 97-102.
18. Yang, R.; Xu, J.; Ozaydin-Ince, G.; Wong, S. Y.; Gleason, K. K. *Chem. Mater.* **2011,** *23*, 1263-1272.
19. Yagüe, J. L.; Gleason, K. K. *Soft Matter* **2012,** *23*, 2890-2894.
20. (a) Bose, R. K.; Heming, A. M.; Lau, K. K. S. *Macromol Rapid Commum.* **2012**, *33*, 1375-1380. (b) Lau, K. K. S.; Gleason, K. K. *Macromol. Biosci.* **2007,** *7*, 429-434. (c) Ozaydin-Ince, G.; Gleason, K. K.; Demirel, M. C. *Soft Matter* **2011,** *7*, 638-643.
21. (a) O'Shaughnessy, W. S.; Gao, M.; Gleason, K. K. *Langmuir* **2006,** *22*, 7021-7026. (b) O'Shaughnessy, W. S.; Murthy, S. K.; Edell, D. J.; Gleason, K. K. *Biomacromolecules* **2007,** *8*, 2564-2570.
22. Trujillo, N. J.; Wu, Q.; Gleason, K. K. *Adv. Funct. Mater.* **2010,** *20*, 607-616.
23. Connell, R. A.; Gregor, L. V. *J. Electrochem. Soc.* **1965,** *112*, 1198-2000.
24. Trujillo, N. J.; Baxamusa, S. H.; Gleason, K. K. *Chem.Mater.* **2009,** *21*, 742-750.
25. Asatekin, A.; Gleason, K. K. *Nano Lett.* **2010,** *11*, 677-686.
26. (a) Mizutani, Y. *Bull. Chem. Soc. Jap.* **1969,** *42*, 2459-2463. (b) Coutinho, F. M. B.; Carvalho, D. L.; La Torre Aponte, M. L.; Barbosa, C. C. R. *Polymer* **2001,** *42*, 43-48. (c) Kawabata, N.; Yoshida, J.-i.; Tanigawa, Y. *Ind. Eng. Chem. Prod. Res. Dev.* **1981,** *20*, 386-390.

27. (a) Montoneri, E.; Orlandoni, A. M.; Modica, G.; Maffi, S.; Pappalardo, G. C., *J. Appl. Polym. Sci.* **1987,** *34*, 2079-2091. (b) Modica, G.; Giuffrè, L.; Montoneri, E.; Wendt, H.; Hofmann, H. *Polymer* **1984,** *25*, 1513-1522.
28. Sigma-Aldrich Co. LLC. *Certificate of Analysis, Divinylbenzene, Technical Grade, 80%, Lot MKBC4100.* http://www.sigmaaldrich.com/catalog/CertOfAnalysisPage.do?symbol=414565&LotNo=MKBC4100&brandTest=ALDRICH (accessed July 2012).
29. Lee, L. H.; Gleason, K. K. *J. Electrochem. Soc.* **2008,** *155*, G78-G86.
30. Oliver, W. C.; Pharr, G. M. *J. Mater. Res.* **1992,** *7*, 1564-1583.
31. (a) Lin-Vien, D.; Colthup, N. B.; Fateley, W. G.; Grasselli, J. G., In *The Handbook of Infrared and Raman Characteristic Frequencies of Organic Molecules*, 1st ed.; Academic Press: San Diego, 1991; p 74. (b) Rackley, F. A.; Turner, H. S.; Wall, W. F.; Haward, R. N. *J. Polym. Sci. Polym. Phys. Ed.* **1974,** *12*, 1355-1370. (c) Stuurman, H.; Köhler, J.; Jansson, S.; Litzén, A. *Chromatographia* **1987,** *23*, 341-349.
32. (a) Chen, C.; Loch, C. L.; Wang, J.; Chen, Z. *The Journal of Physical Chemistry B* **2003,** *107*, 10440-10445. (b) McNamara, K. M.; Williams, B. E.; Gleason, K. K.; Scruggs, B. E. *J. Appl. Phys.* **1994,** *76*, 2466-2472. (c) Wiberley, S. E.; Bunce, S. C.; Bauer, W. H. *Anal. Chem.* **1960,** *32*, 217-221.
33. Goldmann, A. S.; Walther, A.; Nebhani, L.; Joso, R.; Ernst, D.; Loos, K.; Barner-Kowollik, C.; Barner, L.; Müller, A. H. E., *Macromolecules* **2009,** *42*, 3707-3714.
34. Hubbard, K. L.; Finch, J. A.; Darling, G. D. *React. Funct. Polym.* **1998,** *36*, 17-30.
35. Nyhus, A. K.; Hagen, S.; Berge, A. *J. Appl. Polym. Sci.* **2000,** *76*, 152-169.
36. Cesteros, L. C.; Velada, J. L.; Katime, I. *Polymer* **1995,** *36*, 3183-3189.
37. Panov, V. P.; Kazarin, L. A.; Dubrovin, V. I.; Gusev, V. V.; Kirsh, Y. É. *J. Appl. Spectrosc.* **1974,** *21*, 1504-1510.
38. (a) Christy, A. A.; Nyhus, A. K.; Kvalheim, B. G. O. M.; Hagen, S.; Schanche, J. S., *Appl. Spectrosc.* **1998,** *52*, 1230-1239. (b) Coppi, S.; Betti, A.; Bighi, C.; Cartoni, G. P.; Coccioli, F. *J. Chromatogr. A.* **1988,** *442*, 97-103.
39. Smith, B. C., In *Fundamentals of Fourier Transform Infrared Spectroscopy*, 1st ed.; CRC Press: Boca Raton, FL, 1996; p 4.
40. (a) Walczynski, B.; Kolarz, B. N.; Galina, H. *Polym. Commun.* **1985,** *26*, 276-280. (b) Li, W. H.; Li, K.; Stöver, H. D. H.; Hamielec, A. E. *J. Polym. Sci., Part A : Polym. Chem.* **1994,** *32*, 2023-2027.
41. VanLandingham, M. R. *J. Res. Natl. Inst. Stand. Technol.* **2003**, *108*, 249-265.
42. Li, X. D.; Bhushan, B. *Mater. Charact.* **2002**, *48*, 11-36.
43. Newman, S.; Strella, S. *J. Appl. Polym. Sci.* **1965**, *9*, 2297-2310.
44. (a) Okasha, R.; Hild, G.; Rempp, P. *Eur. Polym. J.* **1979,** *15*, 975-982. (b) Xie, T.; Hamielec, A. E. *Macromol. Theory Simul.* **1993,** *2*, 777-803. (c) Elliott, J. E.; Bowman, C. N. *Macromolecules* **1999,** *32*, 8621-8628.
45. Baxamusa, S. H.; Gleason, K. K. *Chem. Vap. Deposition* **2008,** *14*, 313-318.
46. Baxamusa, S. H.; Gleason, K. K. *Thin Solid Films* **2009,** *517*, 3536-3538.
47. Onyon, P. F. *Trans. Faraday Soc.* **1955,** *51*, 400-412.
48. Vivaldo-Lima, E.; Hamielec, A. E.; Wood, P. E. *Polym. React. Eng.* **1994,** *2*, 87.
49. Matheson, M. S.; Auer, E. E.; Bevilacqua, E. B.; Hart, E. J. *J. Am. Chem. Soc.* **1951,** *73*, 1700-1706.
50. Grozea, C. M.; Gunari, N.; Finlay, J. A.; Grozea, D.; Callow, M. E.; Callow, J. A.; Lu, Z.-H.; Walker, G. C. *Biomacromolecules* **2009,** *10*, 1004-1012.
51. Okubo, M.; Minami, H.; Morikawa, K. *Colloid Polym. Sci.* **2003,** *281*, 214-219.

CHAPTER SIX

Synergistic prevention of biofouling by zwitterionic surfaces and low-level chlorination

Reproduced with permission from Yang R., Jang H., Stocker R., and Gleason K. K., *Advanced Materials* **2014**, 26, 1711.

6.1 Abstract

Biofouling – the attachment of organic molecules and microorganisms to submerged surfaces such as membranes – is the bottleneck for seawater desalination that is currently without an effective solution. Biofouling reduces water flux and compromises salt rejection, lowering the productivity and increasing the price of freshwater obtained by seawater desalination. Here, we demonstrate a new approach to anti-biofouling of desalination membranes, based on the application of pyridine-based zwitterionic surfaces synthesized via a low-temperature, solvent-free method. This approach results in smooth, durable, ultrathin layers (30 nm) that are directly deposited onto commercial reverse osmosis membranes without damaging them. Accelerated testing against marine bacteria in multichannel microfluidic devices shows ~100-fold reduction in biofouling compared to bare glass. The unique resistance of the pyridine-based films against degradation by chlorine allows a new synergistic approach to antifouling, based on coupling surface modification and low-level chlorination (5 ppm) in the feed. This combination approach substantially enhances longer-term fouling prevention compared to either surface modification or chlorination alone, and has the potential to reduce or eliminate pretreatment of seawater, the most energy- and chemical-intensive step in desalination plants, and thus to reduce the cost of freshwater production and its collateral toxicity to marine biota.

6.2 Introduction

Water scarcity affects one in three people in the world.[1] With nearly 98% of the world's available water supply being seawater or brackish water, desalination has become an important means to address the scarcity of freshwater resources. Thin film composite (TFC) reverse osmosis (RO) membranes enable the removal of salt ions from seawater at room temperature by applying pressure to the seawater feed. TFC-RO has quickly become the dominating desalination method since its commercialization in the 1980s and is now used in nearly all RO desalination plants.[2] TFC-RO is considered to have the greatest water permeability with high salt rejection rate.[2] The bottleneck of TFC-RO to produce freshwater via seawater desalination at a comparable price to natural freshwater is severe membrane fouling, which impairs water permeation and salt rejection and thus reduces freshwater yield. Currently, marine biota and in particular bacteria are removed from the feed by pretreatment, the most energy-intensive (responsible for >36% of total plant energy consumption) and chemical-intensive step in a desalination plant and one that poses environmental risks to marine organisms when treated water is discharged back into the ocean.[2] Fouling-resistant RO membranes would bring major improvements in energy usage, process reliability and lower the environmental impact of seawater desalination.

Zwitterions are a type of molecular structures with ultra-low fouling properties, demonstrated in applications ranging from bio-assays to artificial tissues,[3,4] originating from the extreme hydrophilicity induced by electrostatic interaction with water molecules,[5,6] which makes the replacement of surface-bound water molecules by foulants enthalpically unfavorable. However, the zwitterionic coatings fabricated so far are not sufficient in long-term antifouling applications due to the limited stability in real-world environments.[7]

The major challenge in the surface modification of TFC-RO membranes is to implement antifouling chemistries without compromising salt rejection and high water flux.[2] The limiting step for the transport of water and salt across membranes is the extremely thin (~100 to 200 nm) polyamide selective layer (Fig. 6-1a). Pin-holes or defects in the polyamide layer are routes for non-selective salt transport and thus quench the salt rejection performance of the membranes. Surface modification methods involving solvents or exposure to high temperatures (Table 6-1) can generate or enlarge the undesirable pin-hole defects.[8] Surface modification layers produce an additional resistance to water permeability and thicknesses >100 nm are undesirable because they cause >40% reduction in the water flux.[9]

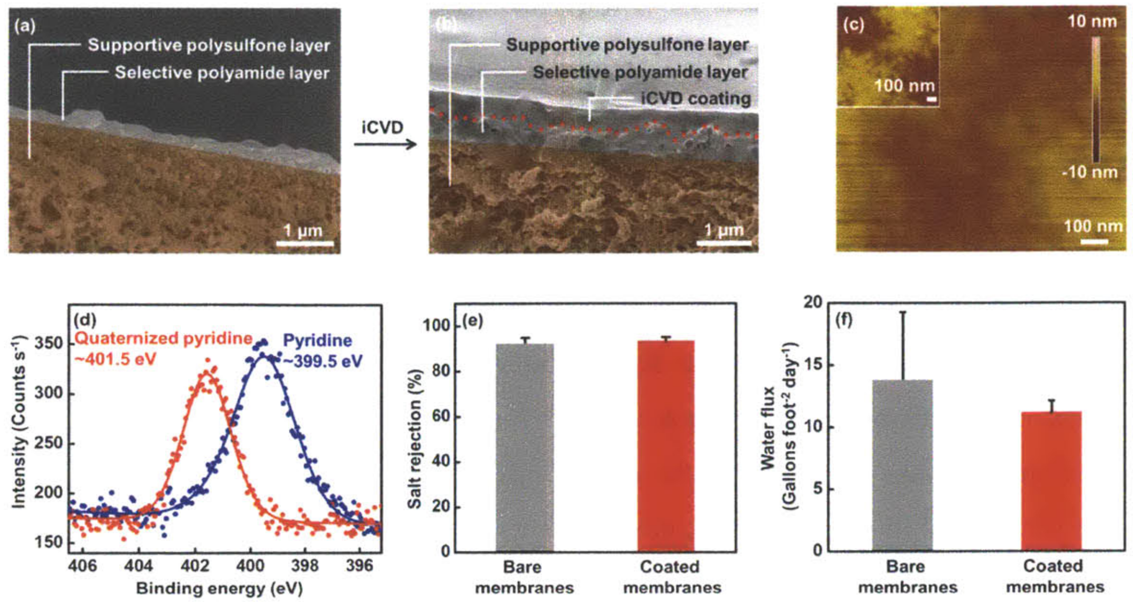

Figure 6-1 | Antifouling zwitterionic coatings applied onto commercial RO membranes via iCVD. a,b, Cross-sectional SEM image of (**a**) bare and (**b**) iCVD coated RO membrane. Panel (**a**) shows the porous supportive polysulfone layer (colored in orange) beneath the nonporous, 200-nm-thick, selective polyamide layer of the RO membrane. In (**b**), the smooth top layer is the iCVD zwitterionic coating, which is grafted to the selective layer. **c**, AFM scan of coated membrane and (inset) bare membrane. Both surfaces are exceptionally smooth, with ~1 nm RMS roughness. **d**, N(1s) XPS high resolution scan of the iCVD P4VP as-deposited (blue) and post-functionalized by PS (red), demonstrating full conversion of pyridine to zwitterion. **e**, Salt rejection of bare and coated membranes. The comparable values of salt rejection indicate that the coating leaves the thin selective layer of the delicate RO membranes intact. **f**, Water flux through bare and coated membranes. Membranes coated with 30-nm functionalized copolymer 1 maintain 86% of the original water flux. Error bars (**e,f**) represent the standard deviations obtained with 3 parallel tests.

Table 6-1| Comparison of the important characteristics of surface modification techniques for zwitterionic antifouling chemistries

methods	*SAMs*[10]	*atom-transfer radical-polymerization*[11]	*bulk solution polymerization*[4]	*layer-by-layer*[12]	*iCVD*
all-dry processing	X	X	X	X	V
substrate-independence	X	X	V	X	V
synthesis speed [nm min^{-1}]	10^{-3}	10^{-2}	$\sim 10^{3}$	~1	~10
small post-treatment roughness	V	V	X	X	V
conformal coating	V	V	X	V	V
ultra-thin coating	V	V	X	V	V
high surface concentration of zwitterionic groups	V	V	X	V	V

In CHAPTER TWO AND CHAPTER THREE, we showed that anti-biofouling coatings of various compositions can be grafted and directly deposited on commercial TFC-RO membranes via an all-dry process, called initiated chemical vapor deposition (iCVD).[9,13,14] The low-temperature, solvent-free processing leaves the delicate polyamide intact and thus maintains the high salt rejection. Water flux is maintained by utilizing ultrathin (30 nm) iCVD layers. However, these acrylate-based films do not resist the degradation by chlorine, the most prevalent disinfection reagent in water treatment.[15]

In this chapter, a novel pyridine-based zwitterionic surface chemistry will be introduced, which displays significantly improved resistance against a variety of molecular foulants and improved tolerance to chlorine exposure as compared to acrylate-based analogs. The chlorine-resistant surface provides a new perspective for achieving long-term antifouling. The pyridine-based zwitterionic surfaces demonstrate a synergy with drinking-water-level chlorination (5 ppm), resulting in exceedingly high antifouling performance. The chlorine-resistant antifouling surfaces are derived from ultrathin iCVD poly(4-vinylpyridine) (P4VP) and its copolymers.[16,17] The vapor deposition allows the synthesis of insoluble cross-linked coatings as thin films directly on a surface in a single step. Enhanced durability results from cross-linking co-monomers and *in situ* grafting. The *in situ* reaction with 1,3-propanesultone (PS) vapors produces pyridine-based sulfobetaine zwitterionic functional groups, having a balanced surface charge. The iCVD synthesis is carried out at low surface temperature (20 °C) to produce robustly adhered, smooth, ultrathin layers (30 nm) directly on even delicate substrates, such as TFC-RO membranes without damaging them. Accelerated testing against marine bacteria in multichannel microfluidic devices shows ~100-fold reduction in biofouling on the coated surface compared to bare glass. The unique resistance of the pyridine-based films against degradation by chlorine allows a new synergistic approach to antifouling, which substantially enhances longer-term fouling prevention compared to either surface modification or chlorination alone, and has the potential to reduce or eliminate pretreatment of seawater, the most energy- and chemical-intensive step in desalination plants, and thus to reduce the cost of freshwater production and its collateral toxicity to marine biota. This approach can facilitate the rational design of the next generation of RO membranes[18-20] and of antifouling strategies in desalination plants, and find additional utility on the hulls of ships and for submerged marine structures.[21]

6.3 Experimental Section

Film deposition and derivatization. All iCVD films were deposited in a custom built vacuum reactor (Sharon Vacuum), as previously described.[9,13] All the chemicals were used as purchased without further purification. Silicon (Si) wafers (Wafer World, test grade) were coated with P4VP or the copolymer of 4VP and DVB without pre-treatment. Prior to deposition, commercial RO membranes (Koch Membrane System, TFC-HR) were cleaned with filtered nitrogen, and then treated with oxygen plasma for 1 minute and then placed in the reactor chamber. The glass slides were treated with trichlorovinylsilane (Aldrich, 97%), as described previously.[22] During iCVD depositions, 4VP (Aldrich, 95%) and DVB (Aldrich, 80%) monomers were heated up to 50 °C and 65 °C in glass jars, respectively and delivered into the reactor using mass flow controllers (1150 MFC, MKS Instruments). Argon patch flow was metered into the reactor through a mass flow controller (1479 MFC, MKS Instruments) and the flow rate was varied to keep the residence time constant. Systematic variation of the flow rate ratios of the two monomers was performed to yield high-zwitterionic-percentage, yet chlorine-resistant films of poly(4-vinylpyridine-co-divinylbenzene) (PVD). Films were deposited at a filament temperature of 250 °C and a stage temperature of 20 °C. Total pressure in the vacuum chamber was maintained at 0.8 Torr for all depositions.

In situ interferometry with a 633 nm HeNe laser source (JDS Uniphase) was used to monitor the film growth and deposit desired thicknesses on Si substrates. A more accurate film thickness on the Si wafer substrates was measured post-deposition using a J.A. Woollam M-2000 spectroscopic ellipsometry at three different incidence angles (65°, 70°, 75°) using 190 wavelengths from 315 to 718 nm. The data were fit using a Cauchy-Urbach model. After deposition, the PVD-coated substrates were derivatized as reported previously.[9,13] FTIR, XPS and contact angle measurements were performed as described previously.[9,13]

Permeation tests. Tests of the coated/bare membranes were performed using a commercial dead-end membrane filtration unit (Sterlitech Corp., HP4750) with a nitrogen cylinder to supply feed pressure, which was kept at 700 psi for all tests. The flow rates of the permeate were determined using a 100 ml metered flask. For the salt rejection calculations, a conductivity meter (CDH-152, Omega Engineering Inc.) was used.

Chlorine resistance tests. Samples subject to chlorine resistance tests were soaked in deionized water for 2 hours, to remove the surface absorbed PS molecules and loosely attached oligomers of 4VP. Samples were dried with nitrogen gas and soaked in aqueous solution of sodium hypochlorite with the concentration of 1000 ppm for various treatment durations. FTIR spectra and dynamic contact angle measurements were taken before and after treating with chlorine solutions.

Bacterial adhesion tests. *V. cyclitrophicus* was used as the model microorganism. Bacteria cells from freezer stocks were inoculated and grown overnight in artificial seawater at 30 °C to an optical density (OD_{600}) of 1 while agitated on a shaker (150 rpm). Cells were suspended in fresh artificial seawater and incubated at 37 °C on a shaker (180 rpm) until the optical density reached 0.2. The bacterial solution was then injected into the microfluidic channels at a constant flow rate of 2 $\mu l\ min^{-1}$, which corresponds to an average flow velocity of 560 $\mu m\ s^{-1}$. During the combination treatment, chlorine was directly added to the vessel containing the media with bacteria to a final concentration of 5 ppm. Note that in this case the images acquired at a certain time (*t* hours) captured bacteria that have been exposed to chlorine for *t* hours.

6.4 Results and Discussion

Ultrathin (30 to 300 nm) iCVD coatings are successfully grafted and deposited directly onto commercial TFC-RO membranes (Fig. 6-1b), followed by the vapor phase derivatization (Fig. 6-2).

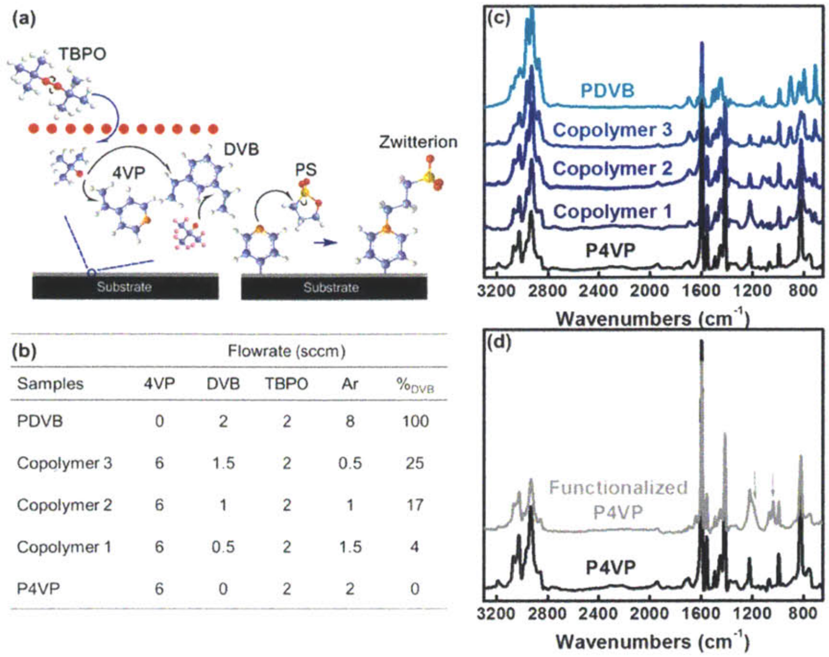

(b)

	Flowrate (sccm)				
Samples	4VP	DVB	TBPO	Ar	$\%_{DVB}$
PDVB	0	2	2	8	100
Copolymer 3	6	1.5	2	0.5	25
Copolymer 2	6	1	2	1	17
Copolymer 1	6	0.5	2	1.5	4
P4VP	6	0	2	2	0

Figure 6-2 | Synthesis of antifouling zwitterionic coatings via iCVD. a, Processing and reactions during the synthesis of iCVD zwitterionic coatings. Initiator *tert*-butyl peroxide (TBPO) is radicalized by heated filaments (●) kept at around 250 °C. *Tert*-butyl oxide radicals react with vinyl bonds in 4-vinylpyridine (4VP) and divinylbenzene (DVB) to form cross-linked copolymer, which then react with 1,3-propanesultone (PS) to form zwitterions. **b, c,** Reaction conditions (**b**) and FTIR spectra (**c**) for homopolymers PDVB (cyan) and 4VP (black) and copolymers 1 (dark blue), 2 (blue) and 3 (light blue). Increasing the flow rate of DVB in the reactor feed while keeping the overall flow rate constant results in more incorporation of DVB repeat units (**b**). Areas under peaks at 710 cm^{-1} (**c**), corresponding to pendant vinyl bonds in DVB repeat unit, decrease readily from PDVB to copolymers, and to P4VP, indicating compositional difference. The 710 cm^{-1} peak is used to calculate composition of copolymers.[16] **d,** FTIR spectra of the iCVD P4VP as-deposited (black) and post-functionalized by PS (grey), demonstrating conversion of pyridine to zwitterion by the emergence of peaks around 1199 and 1036 cm^{-1}(grey arrows), attributed to the asymmetric and symmetric stretching vibrations of SO_3^-.

The all-dry-processed coating conforms to the geometry of the underlying substrate (Fig. 6-1b,c), because surface tension and de-wetting are avoided. The root-mean-square (RMS) roughness of bare and coated RO membranes is 1.3±0.3 nm (Fig. 6-1c, inset) and 0.8±0.1 nm (Fig. 6-1c), respectively. This exceptional smoothness is critical to the fouling resistance of the membrane surface,[2] because larger surface areas and more binding sites are available for foulants to attach on a rougher surface. In addition, nano- and micro-scale roughness can entrap proteins and bacteria, respectively, and provide a "shield" to attached foulants from shear forces.[23] The benign reaction conditions allow retention of the zwitterionic groups, as evidenced by the N(1s) high-resolution scan by X-ray photoelectron spectroscopy (Fig. 6-1d). The binding energy of the pyridine nitrogen species from the as-deposited iCVD layer is ~399.5 eV[24] with a small tail around 402 eV that is attributed to the inevitable post-treatment adsorption of atmospheric CO_2.[25] The binding energy of quaternized pyridine nitrogen is ~401.5 eV[25] and the symmetric peak profile indicates complete quaternization by the PS post-treatment.

The salt rejection of the surface-modified RO membranes is unaltered, confirming the benign nature of the solvent-free process (Fig. 6-1e). This substrate-independent method allows simultaneous deposition on multiple substrates. This feature is used to simultaneously deposit on RO membranes and on a silicon wafer in order to achieve precise control of coating thickness, which is critical because thin coatings are essential to maintaining the high water flux across RO membranes.[2] The coating thickness on RO membranes is compared to that on a silicon wafer,[9] which is monitored via *in situ* interferometry. With the 30-nm coating thickness achieved with this method, the water flux is reduced only by ~14% compared to untreated RO membranes (Fig. 6-1f). This high water flux is achieved with an amount of the cross-linker (4%; copolymer 1; Fig. 6-2), divinylbenzene (DVB), sufficiently high to ensure the stability of the coating and sufficiently low to effect a minimal reduction in water flux. As expected, water flux is reduced (by 72%; Fig. 6-3) for higher DVB content (17%; copolymer 2) and also (by 84%) for the homopolymer PDVB, owing to its high cross-linking density.

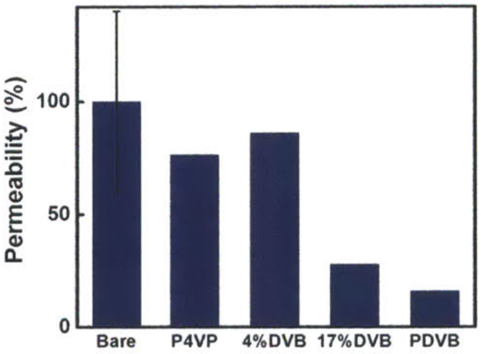

Figure 6-3 | Relative water permeability of unmodified and surface-coated reverse osmosis (RO) membranes. Water permeability was measured with a dead-end stir cell with 700 psi feed pressure. No salt was added to the feed. All permeability results are normalized by that of unmodified RO membrane (Bare). Coatings of functionalized P4VP and copolymer 1 (4% DVB repeat units) do not lower the permeability significantly (less than 20% reduction); while functionalized copolymer 2 (17% DVB) drastically decreases the permeability, indicating that additional cross-linking density increases resistance of water transport across membranes. Homopolymer of PDVB can achieve only 16% of the permeability of bare RO membranes.

It is worth noting that copolymer 1, despite the higher cross-linking density, has similar water flux as homopolymer P4VP (Fig. 6-2 and 6-3). This is likely a result of surface chain reorganization of copolymer 1 upon contacting water. Therefore, copolymer 1 is chosen as providing the optimal trade-off between coating stability and water flux. Taken together, these results show that the proposed approach can overcome the major challenge in the field of surface modification for desalination, by implementing antifouling chemistry without compromising water flux and salt rejection of the resulting membranes.

To reveal the chemistry of the antifouling coatings, the retention of functional groups and compositions of as-deposited and functionalized iCVD polymers are analyzed using Fourier transform infrared (FTIR). Excellent agreement is observed between the spectra of iCVD- and solution-polymerized PDVB and P4VP,[26,27] indicating that the non-vinyl organic functionalities in the monomers are retained in the iCVD films. Successful polymerization of DVB (Fig. 6-4b) is evidenced by the reduction of the 903 cm^{-1} peak in the PDVB spectrum (Fig. 6-4a, black), which results from the out-of-plane CH_2 deformation in vinyl groups. The existence of this peak in the PDVB spectrum is due to the presence of unreacted pendant vinyl bonds.[16,28]

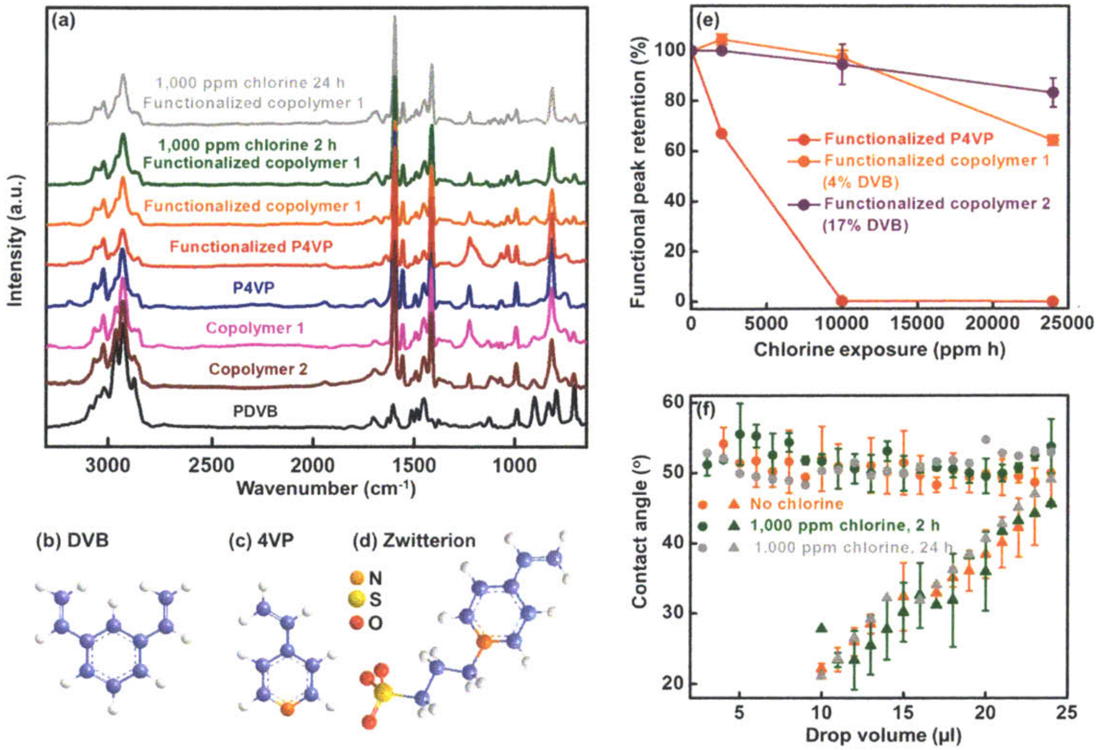

Figure 6-4 | Chlorine-resistant zwitterionic chemistry. a, FTIR spectra of homopolymers and copolymers as-deposited, after PS functionalization, and after chlorine exposure. Copolymer 1 and 2 contain 4% and 17% DVB repeat units, respectively. The spectra of functionalized P4VP and copolymer 1 display a peak corresponding to the zwitterionic moiety (1036 cm^{-1}). Copolymer 1 shows unchanged spectra after 1000 ppm chlorine treatment for 2 hours and 24 hours, demonstrating excellent chlorine resistance. Spectra are offset vertically for clarity. **b-d**, Molecular structure of the cross-linker DVB, 4VP and the zwitterionic moiety obtained after functionalization. **e**, The polymers' chlorine resistance, quantified as the area under the 1600 cm^{-1} peak (corresponding to the pyridine ring). Functionalized homopolymer P4VP does not resist the oxidative damage of chlorine, whereas functionalized copolymer 1, containing merely 4% cross-linker repeat units, resists chlorine considerably better. Increasing cross-linker repeat units beyond 4% improves chlorine resistance only slightly. **f**, Advancing (●) and receding (▲) contact angles of the functionalized copolymer 1 before and after chlorine treatment. The drop volume is the volume of the water droplet used to measure the contact angle. Contact angles are unchanged by chlorine treatment, confirming the chlorine resistance observed via FTIR (panel **a**).

For the iCVD polymers PDVB (black), copolymer 2 (wine), copolymer 1 (magenta) and P4VP (blue), there is a decreasing trend in the area under the 710 cm^{-1} peak, a measure of the number of *m*-substituted aromatic rings in the DVB repeat units (Fig. 6-4a). This is utilized to calculate compositions of the iCVD copolymers,[16] which are confirmed by X-ray photoelectron spectroscopy (XPS) survey scans. The composition of the copolymers can be tuned simply by varying the flow rate ratios of 4VP and DVB monomers (Fig. 6-2). In the spectra of P4VP and copolymers, the strong peak at 1600 cm^{-1} is attributed to the C-C and C-N stretching vibrations in the pyridine ring (Fig. 6-4c),[16,28] whose intensity increases with more P4VP repeat units (Fig. 6-2). FTIR spectra collected after the PS derivatization (Figs. 6-4a and 6-2) confirms the formation of the pyridine-based sulfobetaine (Fig. 6-4d) via ring-opening of PS, as evident by the appearance of a peak at 1036 cm^{-1} in the spectra of functionalized P4VP (red) and copolymer 1 (orange) (Fig. 6-4a). This peak is attributed to the symmetric stretching of the SO_3^- group.[28] Therefore, pyridine-based zwitterionic structures designed to resist oxidative damages are successfully synthesized using the solvent-free scheme.

To evaluate the chlorine resistance of the iCVD films, we subject the functionalized homopolymer P4VP, copolymer 1 and copolymer 2 to treatment with a 1000 ppm solution of sodium hypochlorite and we acquire FTIR spectra after different treatment durations. From the spectra, we measure the areas under the 1600 cm^{-1} peak (Fig. 6-4a,e) to quantify the functional retention of the zwitterionic structure; the strong peak intensity renders the quantification more accurate. The excellent chlorine resistance of copolymer 1 (4% DVB) is evident from the negligible changes in its spectrum after 2 (green) and 24 (grey) hours of chlorine treatment (Fig. 6-4a). In contrast, homopolymer P4VP is rendered soluble by a 10-hour exposure, as shown by the absence of functional peaks in the FTIR spectrum (Fig. 6-5).

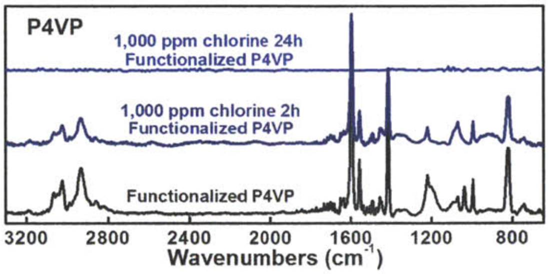

Figure 6-5 | FTIR spectra of functionalized iCVD P4VP homopolymer before and after treatments with 1000 ppm chlorine solution. The coating was first soaked in DI water for 2 hours to remove the surface absorbed PS molecules and loosely attached oligomers of 4VP. The sample was then treated with 1000 ppm chlorine for 2 hours. The SO_3^- peaks around 1199 and 1036 cm^{-1} have significantly smaller peak areas, indicating the dissolution of uncross-linked iCVD zwitterionic coating. After 24 hours in 1000ppm chlorine solution, the coating becomes completely soluble in water the no peaks remain in the FTIR spectrum.

Importantly, the addition of 4% DVB cross-linker produces a major increase in the resistance to chlorine, whereas additions beyond 4% result in minor additional resistance (Fig. 6-4e): after 10000 ppm h exposure to chlorine, ~94% and ~99% pyridine functionalities remain in functionalized copolymers 1 (4% DVB) and 2 (17% DVB), respectively. Functionalized copolymer 1 is thus most desirable because it resists chlorine very effectively while leaving the water flux nearly intact (Fig. 6-3).

These observations are corroborated by dynamic contact angle measurements on functionalized P4VP and copolymer 1 before and after chlorine treatment, which yields a comprehensive evaluation of the effects of chlorine on the coatings, because the dynamic contact angles of coated surfaces are affected by coating chemistry, surface roughness, swelling, and surface chain reorganization.[29] For the functionalized P4VP before chlorine treatment we measure advancing and receding contact angles of 31° and 20°, whereas after 2000 ppm h chlorine exposure these values become 48° and 18°, respectively (Fig. 6-6).

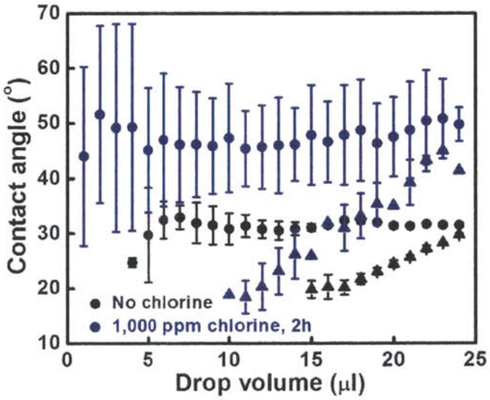

Figure 6-6 | Dynamic contact angles of functionalized iCVD P4VP homopolymer before and after treatments with 1000 ppm chlorine solution. After 2 hours in 1000 ppm chlorine solution, the advancing contact angles of functionalized homopolymer P4VP (●) increase significantly, indicating the damage to the film by chlorine. Larger error bars are signs of inhomogeneity of the chlorine-treated film. Dynamic contact angles of the film after 24 hours chlorine exposure are not shown here because the film dissolves in water. It is worth noting that the incorporation of cross-linker DVB in copolymer 1 (Fig. 6-4f, ●) renders the advancing contact angle 20° higher than P4VP (●), but with minimal effects on the receding contact angle (Figs. 6-4f, ▲ and 6-6 ▲), indicating the surface chain reorganization. When the functionalized copolymer 1 is in contact with water, hydrophilic segments tend to migrate toward the surface by thermodynamic driving force to minimize the interfacial free energy. This phenomenon, in part corroborates the similar water flux obtained with functionalized homopolymer P4VP and copolymer 1 films (Fig. 6-3). It also ensures the high concentration of zwitterionic moieties on the submerged iCVD coating surface, precisely where the antifouling properties are exploited.

These considerable changes in dynamic contact angles reflect the poor chlorine resistance of the functionalized P4VP films. In contrast, the advancing and receding contact angles of the functionalized copolymer 1 are 51° and 24°, respectively. In spite of the higher cross-linking density, copolymer 1 has similar receding contact angle as P4VP. This is a sign of surface chain reorganization[29] and corroborates the comparable water flux obtained with functionalized P4VP and copolymer 1 films. The dynamic contact angles remain unchanged after as much as 24000 ppm h chlorine treatment (Fig. 6-4f), confirming the excellent chlorine resistance of the functionalized copolymer 1 films: the coating chemistry, surface roughness, swelling, and surface chain reorganization all remain essentially unaltered even upon prolonged exposure to chlorine.

We demonstrate the anti-biofouling properties of the new surface treatment both with dissolved foulants and with marine bacteria. Quantification of the surface adsorption of 1 mg ml^{-1} bovine serum albumin (BSA) in phosphate-buffered saline (PBS) is conducted via quartz crystal microbalance with dissipation monitoring (QCM-D). BSA is a widely used test protein for antifouling studies.[30,31] Analogous tests are carried out with a representative polysaccharide, 1 mg ml^{-1} sodium alginate, the major component of extracellular materials that lead to membrane biofouling.[32] QCM-D tests reveal no adsorption of either foulant over 200 minutes on the functionalized copolymer 1 surface (Fig. 6-7).

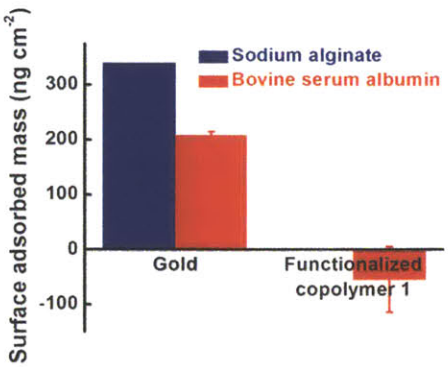

Figure 6-7 | Surface adsorption of sodium alginate and bovine serum albumin (BSA) on gold and functionalized copolymer 1 surfaces. 1mg ml^{-1} solutions were introduced into the chamber of quartz-crystal micro-balance with dissipation monitoring (QCM-D), where the gold or coated QCM-D sensors were placed. The solutions of foulants were fed continuously for 2 h, and changes in the dissipation and frequency were recorded *in situ*. The dissipation changes are negligible for all cases and thus frequency changes are converted to surface adsorbed masses using the Sauerbrey equation. Gold surface adsorbs sodium alginate (blue) very strongly, and the surface mass reaches ~340 ng cm^{-2} after 2 h. The adsorption of BSA (red) on gold is ~208 ng cm^{-2}. Functionalized copolymer 1 resists the adsorption and the surface adsorbed mass remains around 0 ng cm^{-2} for both foulants, demonstrating the fouling resistance of iCVD zwitterionic coatings.

The successful antifouling against dissolved chemicals leads us to test the surfaces against fouling by marine bacteria. We use natural seawater samples and a culture of *Vibrio cyclitrophicus*, a species broadly representative of bacteria prevalent in coastal waters, from where seawater for desalination typically originates. The dynamics of bacterial attachment are studied in a microfluidic flow system and imaged with an inverted microscope equipped with a CCD camera.[33] Images are extracted from full movies and quantified by image analysis. Microchannels of 600 × 100 μm rectangular cross-section are fabricated out of polydimethylsiloxane (PDMS) using standard soft lithography techniques[33] and mounted on a microscope glass slide that has been coated with a ~300-nm-thick film of functionalized copolymer 1. Fresh seawater is harvested and used on the same day as the feed solution for the microfluidic fouling tests, without any pretreatment, through continuous injection at a rate of 2 μl min^{-1} (corresponding to a mean flow velocity of ~560 μm s^{-1}). Fabrication of multiple (2-4) microchannels on the same chip allows parallel, simultaneous experiments and thus a direct comparison of different treatments and the minimization of confounding factors. Because experiments lasting up to 100 hours reveal no discernible surface attachment (Fig. 6-8), irrespective of surface conditions, we run accelerated fouling experiments with concentrated cultures of *V. cyclitrophicus*, grown overnight in artificial seawater and concentrated to an optical density ($OD_{600} = 0.2$; ~2×10^8 cells ml^{-1}) corresponding to early exponential phase. This bacterial concentration is ~200 times that of typical seawater.

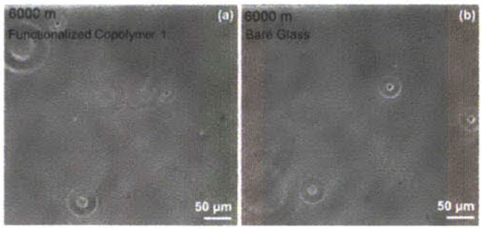

Figure 6-8 | Surfaces after 100 h in natural seawater. Both (**a**) functionalized copolymer 1 surface and (**b**) bare glass surface remain clean after exposure to flowing seawater for 100 h. Therefore, accelerated fouling experiments are conducted with concentrated cultures of *Vibrio cyclitrophicus*.

In the accelerated tests, the iCVD zwitterionic coatings show much greater resistance to bacterial attachment than bare glass (Fig. 6-9a,b,e,f; Fig. 6-10).

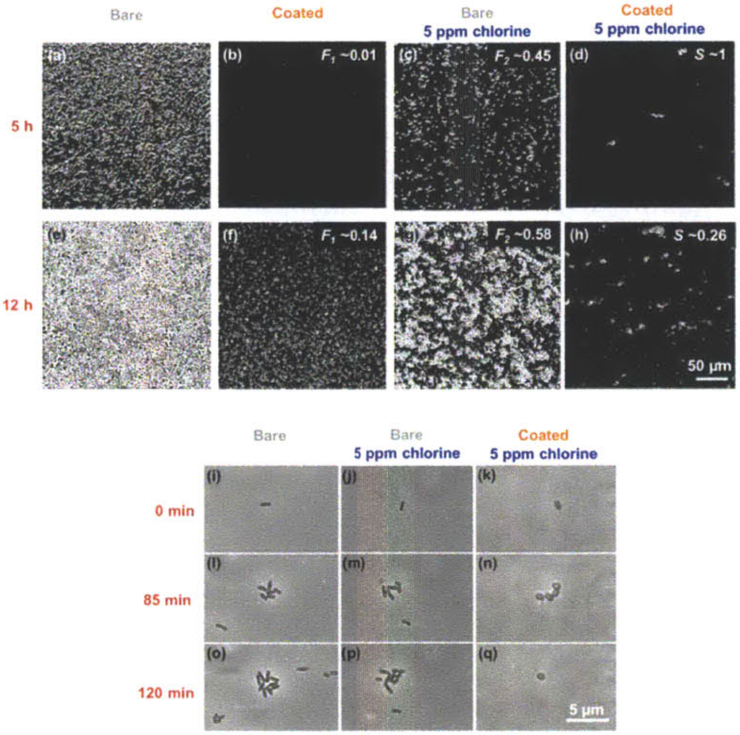

Figure 6-9 | Enhanced fouling resistance by zwitterionic surfaces and low-level chlorination. a-h, Attachment of concentrated suspensions of the marine bacteria *V. cyclitrophicus* to glass surfaces with (**a,e**) no treatment; (**b,f**) the zwitterionic coating (functionalized copolymer 1); (**c,g**) chlorination (5 ppm); and (**d,h**) the zwitterionic coating plus chlorination, after 5 hours (**a-d**) and 12 hours (**e-h**). The zwitterionic coating shows no signs of fouling after 5 hours under accelerated biofouling tests conditions (**b**), whereas after the same amount of time the bare surface has significant surface coverage by bacteria (**a**). After 12 hours, neither the coating alone (**f**) nor chlorination alone (**g**) is effective at resisting biofouling, whereas the combined treatment exhibits dramatically increased fouling resistance and maintains a clean surface (**h**). Relative fouling indices, F_1 (**b,f**) – the fraction of surface coverage for the coated surface compared to the bare glass control – and F_2 (**c,g**) – the fraction of surface coverage in the presence of chlorination, compared to that in the absence of chlorination for a bare glass surface – are used to quantify the effects of coating and chlorination, respectively. The synergistic fouling prevention is quantified by the synergistic index, S (**d,h**), where $S < 1$ indicates synergy between the coating and chlorination. See also Supplementary Movies 3 and 4. Images in (**a-h**) are captured with the same magnification and the scale bar represents 50 µm. **i-q**, Comparison of the attachment and proliferation of a *V. cyclitrophicus* bacterium on (**i,l,o**) a bare surface, (**j,m,p**) a bare surface with chlorination, and (**k,n,q**) a coated surface with chlorination. The 5 ppm chlorine addition did not prevent bacterial proliferation on the surface (**m,n,p**). The zwitterionic chemistry is critical for the synergistic fouling resistance, as bacteria are readily removed from the zwitterion-coated surface by even laminar flow (Reynolds number ~0.1) (**q**). See also Supplementary Movie 5. The scale bar represents 5 μm.

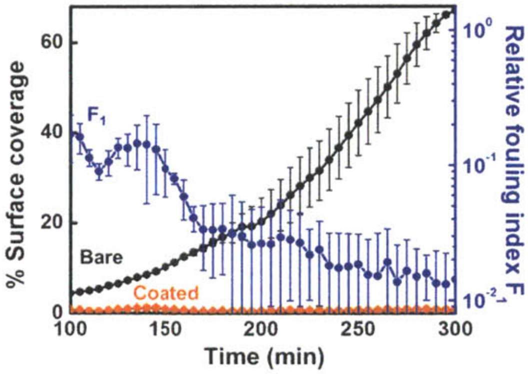

Figure 6-10 | Surface coverage by *V. cyclitrophicus* on bare glass and iCVD zwitterionic surfaces and relative fouling index F_1. *V. cyclitrophicus* attaches readily on the bare glass surface (black), for which the surface coverage reaches ~65% after 300 minutes. After the same amount of time, the functionalized copolymer 1 surface (orange) remains clean, with 0% surface coverage. The relative fouling index F_1(blue), defined as the fraction of surface coverage for the coated surface compared to the bare glass control, decreases steadily over the course of the test. After 300 minutes, F_1 reaches ~10^{-2}, corresponding to ~100 times better fouling resistance of the functionalized copolymer 1 surface compared to the bare glass surface.

Fouling is quantified by time-lapse imaging of the surface, followed by image analysis to determine the number of attached cells and the percent surface coverage by bacteria. Despite the intrinsic fouling resistance of glass surfaces,[30] the number of attached cells on bare glass increases steadily over time, and exponentially after 50 minutes. After 5 hours, the cell count over a 0.16-mm^2 area of the bare glass surface reaches ~7500, (Fig. 6-9a), whereas it remains close to zero on the coated surface (Fig. 3-9b). Defining a relative fouling index, F_1, as the fraction of surface coverage for the coated surface compared to the bare glass control, we find that F_1 decreases drastically over time for functionalized copolymer 1 and drops to ~0.01 after 5 hours (Fig. 6-10). This result demonstrates the exceptional fouling resistance of iCVD zwitterionic coatings, in particular in view of the fact that smooth, bare glass is already a rather good antifouling surface.[30]

The surfaces' antifouling effects are further boosted by low-level chlorination, resulting in a new synergistic approach against fouling made possible by functionalized copolymer 1's good resistance to chlorine (Fig. 6-4a,e,f). We run additional, accelerated microfluidic tests where the suspension of *V. cyclitrophicus* is amended with 5 ppm of sodium hypochlorite (Fig. 6-9c,d,g,h), a concentration comparable to the residual chlorine level in the USA national drinking water standards.[34] To quantify the effect of chlorination we define a second fouling index, F_2, computed as the fraction of surface coverage in the presence of chlorination, compared to that in the absence of chlorination, for the case of a bare glass surface. Although chlorination overall reduces surface fouling, signs of fouling on bare glass in the presence of 5 ppm chlorine emerge after 5 hours (F_2 ~0.45; Fig. 6-9c) and after 12 hours fouling is severe (F_2 ~0.58; Fig. 6-9g). Therefore, chlorination at a level of 5 ppm is less effective than the zwitterionic coating in preventing bacterial attachment. However, the synergistic effect of the zwitterionic coating and chlorination dramatically increases fouling resistance over each treatment in isolation (Fig. 6-9d,h). After 12-hour exposure to the *V. cyclitrophicus* suspension, the surface coverage is 35.3±1.7% on bare glass in the presence of 5 ppm chlorine, 14.1±3.4% on the coated surface without chlorine, and only 1.5±0.4% on the coated surface in the presence of 5 ppm chlorine. The percent surface coverage in the synergistic treatment is 0.02 of that of a bare glass surface without chlorine, four-fold smaller than the prediction ($F_1 \times F_2$) obtained if the effect was simply multiplicative.

To quantify the synergistic effect of the two antifouling strategies, we compute an antifouling synergistic index, S (Fig. 6-11a, inset). Synergistic indices have been used among others to describe the effects of multi-strategy anti-tumor treatments, where $S < 1$ indicates a synergistic effect in killing tumor cells by the different strategies in the treatment.[35,36] Here we define S as

$$S = \frac{\%\text{Surface coverage}_{\text{combination treatment,observed}}}{\%\text{Surface converage}_{\text{combination treatment,expected}}} = \frac{\%\text{Surface converage}_{\text{combination treatment,observed}}}{F_1 \times F_2 \times \%\text{Surface converage}_{\text{bare glass}}} \qquad (6\text{-}1)$$

The temporal dynamics of S (Fig. 6-11a, inset) reveal values of $S < 1$ after ~400 minutes, and a subsequent steady decrease to ~0.1 after 900 minutes. No signs of saturation in the decrease are observed, demonstrating the long-term nature of the synergy. The values of S within the first 5 hours are not shown because the surface chemistry alone reduces fouling to non-detectable levels (i.e., $F_1 \sim 0$) during this time and thus a quantification of S is not meaningful.

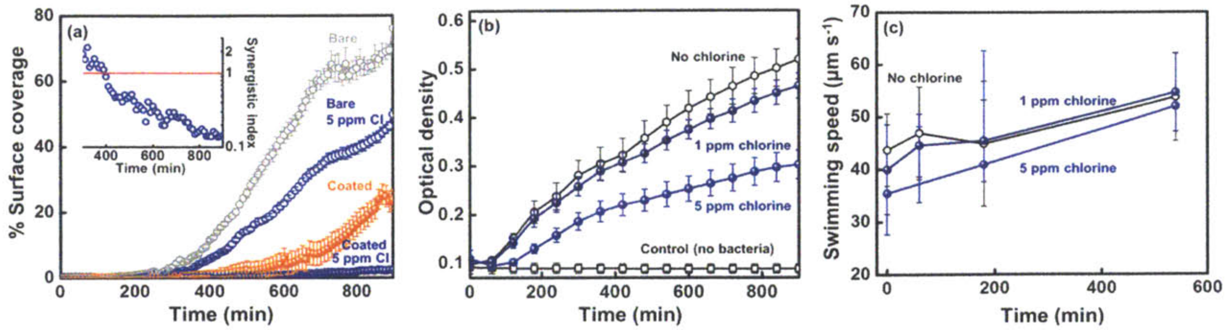

Figure 6-11 | Synergistic prevention of bacterial fouling by the combination treatment. a, Surface coverage by *V. cyclitrophicus* bacteria under different conditions. The synergistic treatment – integrating iCVD zwitterionic coating with low-level (5 ppm) chlorination – shows exceptional long-term antifouling activity even under accelerated biofouling conditions (i.e., dense bacterial suspensions), when each method in isolation begins to fail. **Inset,** Time series of the synergistic index (*S*), quantifying synergistic effect of the two antifouling strategies. Values of $S < 1$ indicate a positive synergy between the two treatments. The monotonic decrease of *S*, with no signs of saturation over 15 hours, demonstrates the importance of synergistic effect on long-term fouling resistance. **b,** Viability of *V. cyclitrophicus* upon addition of chlorine at different concentrations. 1 ppm chlorine does not significantly impact bacterial growth, whereas 5 ppm chlorine reduces the optical density by 42%, but does not kill bacteria. Killing by chlorine is thus not the dominant factor in the success of the synergistic treatment. **c,** Mean swimming speed of *V. cyclitrophicus*, obtained by tracking of individual cells. Addition of up to 5 ppm chlorine does not significantly change the bacteria's swimming speed, suggesting that prevention of attachment is not due to a reduction of encounter rates with surfaces.

In the attempt to reveal the mechanism underpinning the synergistic effect, the cell-surface interaction is investigated by observing a single bacterium for its proliferation and motility on the surface for the different treatments (Fig. 6-9i-q). After 85 minutes, replication has occurred under all conditions (Fig. 6-9l-n), at a mildly lower rate in the presence of 5 ppm chlorine (Fig. 6-9m,n), suggesting that the low dose of chlorine has only small effects on cell growth. This hypothesis is supported by direct viability tests (Fig. 6-11b), showing that the growth of *V. cyclitrophicus* (measured as the optical density of cell cultures) is negligibly affected by addition of 1 ppm chlorine and exhibits a 42% reduction with 5 ppm chlorine addition. Furthermore, tracking of individual cells shows that motility is not significantly affected by 1 ppm or 5 ppm chlorination (Fig. 6-11c). Although growth in batch culture might differ from growth on a microchannel surface, taken together these results (Figs. 6-11b and 6-9l-n) demonstrate that the observed antifouling and synergistic effect of chlorine are not based on killing of the bacteria.

Instead, the primary difference among the three single-cell cases (Fig. 6-9i-q) resides in the dependence of cell removal from the surface on the surface chemistry (Fig. 6-9o-q): whereas bacteria remain largely attached to the bare glass surface, they are easily removed from the coated surface by ambient fluid flow, independent of the presence of chlorine. In particular, bacterial removal from the iCVD zwitterionic coating occurs readily even under the low, laminar flow conditions within the microchannel (Reynolds number ~0.1).

6.5 Conclusion

We have demonstrated the ability of ultrathin, chlorine-resistant iCVD zwitterionic copolymers to act as antifouling coatings and, based on their resistance to chlorine, we have proposed a novel, multi-strategy approach to antifouling, which hinges on the synergy between surface chemistry and chlorination. The zwitterionic coating prevents the attachment of *V. cyclitrophicus* almost 100 times more effectively than glass after 5 hours (Figs. 6-9a,b, 6-11a and Fig. 6-10), while chlorination, with concentrations as low as the regulated chlorine residue in drinking water, is able to enhance the long-term fouling resistance of the zwitterionic coating by 9.4-fold after 12 hours (Figs. 6-9d,h and 6-11a), with no signs of saturation.

A key advantage of the zwitterionic coatings reported here is the substrate-independence of the vapor application process, which makes these coatings easily applicable to a broad range of surfaces. In particular, these coatings may be applied on the latest salt-rejecting layers,[18-20] which resist exposure to chlorine, providing a path towards solving the desalination industry's bottleneck of the susceptibility of TFC-RO membranes to oxidative damage by chlorine. The surface treatment is benign, easily scalable[37] and compatible with the infrastructure in membrane industry,[2] which gives rise to a stable, non-toxic and inexpensive ultrathin coating. The good fouling resistance and chlorine resistance of this coating can help eliminate the most energy- and chemical-intensive step (pretreatment of seawater) in a RO desalination plant,[2] and reduce the environmental impacts of brine discharge. This approach therefore promises to lower the price of freshwater in water-scarce countries, where desalination may serve as the only viable means to provide the water supply necessary to sustain agriculture, support personal consumption, and promote economic development.

References

1. WHO. *Book 10 facts about water scarcity*, <http://www.who.int/features/factfiles/water/en/> (2009).
2. Elimelech, M. & Phillip, W. A. *Science* **333,** 712-717, (2011).
3. Jiang, S. & Cao, Z. *Adv. Mat.* **22,** 920-932, (2010).
4. Zhang, L. *et al. Nature Biotechnology* **31,** 553-556, (2013).
5. Chen, S., Zheng, J., Li, L. & Jiang, S. *J Am Chem Soc* **127,** 14473-14478, (2005).
6. Kitano, H. *et al. Macromol. Biosci.* **5,** 314-321, (2005).
7. Yang, R., Jang, H., Stocker, R. & Gleason, K. K. *Advanced Materials* **26,** 1711-1718, (2014).
8. Yamasaki, A. *et al. Colloids Surf., B* **28,** 53-62, (2003).
9. Yang, R., Xu, J., Ozaydin-Ince, G., Wong, S. Y. & Gleason, K. K. *Chem. Mater.* **23,** 1263-1272, (2011).
10. Holmlin, R. E., Chen, X. X., Chapman, R. G., Takayama, S. & Whitesides, G. M. *Langmuir* **17,** 2841-2850, (2001).
11. Li, Q. & Elimelech, M. *Environ. Sci. Technol.* **38,** 4683-4693, (2004).
12. Ishihara, K. *et al. J. Biomed. Mater. Res.* **26,** 1543-1552, (1992).
13. Yang, R. & Gleason, K. K. *Langmuir* **28,** 12266-12274, (2012).
14. Höök, F., Rodahl, M., Kasemo, B. & Brzezinski, P. *Proc. Natl. Acad. Sci. U. S. A.* **95,** 12271-12276, (1998).
15. Park, H. B., Freeman, B. D., Zhang, Z.-B., Sankir, M. & McGrath, J. E. *Angewandte Chemie International Edition* **47,** 6019-6024, (2008).
16. Petruczok, C. D., Yang, R. & Gleason, K. K. *Macromolecules* **46,** 1832-1840, (2013).
17. Alf, M. E. *et al. Adv. Mat.* **22,** 1993-2027, (2010).
18. Olenych, S. G., Moussallem, M. D., Salloum, D. S., Schlenoff, J. B. & Keller, T. C. S. *Biomacromolecules* **6,** 3252-3258, (2005).
19. Salloum, D. S., Olenych, S. G., Keller, T. C. S. & Schlenoff, J. B. *Biomacromolecules* **6,** 161-167, (2004).
20. Holt, J. K. *et al. Science* **312,** 1034-1037, (2006).
21. Sauerbrey, G. *Zeitschrift Für Physi* **155,** 206-222, (1959).
22. Trujillo, N. J., Baxamusa, S. H. & Gleason, K. K. *Chem. Mater.* **21,** 742-750, (2009).
23. Lau, K. K. S. & Gleason, K. K. *Adv. Mater.* **18,** 1972-1977, (2006).
24. Beamson, G. & Briggs, D. *High resolution XPS of organic polymers: the Scienta ESCA300 data base*. (John Wiley & Sons, New York, 1992).
25. Spanos, C. G., Badyal, J. P. S., Goodwin, A. J. & Merlin, P. J. *Polymer* **46,** 8908-8912, (2005).
26. Ozaydin-Ince, G. & Gleason, K. K. *J. Vac. Sci. Technol., A* **27,** 1135-1143, (2009).
27. Martin, T. P., Kooi, S. E., Chang, S. H., Sedransk, K. L. & Gleason, K. K. *Biomaterials* **28,** 909-915, (2007).
28. Chen, S. F., Zheng, J., Li, L. Y. & Jiang, S. Y. *JACS* **127,** 14473-14478, (2005).
29. Lin- Vien, D. C., N. B.; Fateley, W. G.; Grasselli, J. G. *The Handbook of Infrared and Raman Characteristic Frequencies of Organic Molecules*. (Academic Press, New York, 1991).
30. Chakraborty, A. K., Bischoff, K. B., Astarita, G. & Damewood, J. R. *JACS* **110,** 6947-6954, (1988).
31. Baxamusa, S. H. & Gleason, K. K. *Adv. Funct. Mat.* **19,** 3489-3496, (2009).
32. Asatekin, A. *et al. J. Membr. Sci.* **285,** 81-89, (2006).
33. Nguyen, A. T., Baggerman, J., Paulusse, J. M. J., van Rijn, C. J. M. & Zuilhof, H. *Langmuir* **27,** 2587-2594, (2011).
34. Baxamusa, S. H. I., S. G.; Gleason, K. K. *Phys. Chem. Chem. Phys.* **11,** 5227-5240, (2009).
35. Shaffer, D. L. *et al. Environmental Science & Technology* **47,** 9569-9583, (2013).
36. Natalio, F. *et al. Nat Nano* **7,** 530-535, (2012).
37. Gupta, M. & Gleason, K. K. *Thin Solid Films* **515,** 1579-1584, (2006).

CHAPTER SEVEN

Molecular fouling resistance of zwitterionic and amphiphilic antifouling thin films

Reproduced with permission from Yang R., Xu J., Ozaydin-Ince G., Wong S. Y. and Gleason K. K., *Chemistry of Materials* **2011**, 23, 1263.

7.1 Abstract

Prevention of fouling is critical in various applications ranging from water purification to implantable biomedical devices. Recent development in surface modification has created a rich library of antifouling surface chemistries, many of which can be categorized into one of two groups: hydrophilic surfaces or amphiphilic surfaces. The straightforward preparation of an antifouling thin film coating in both categories via initiated chemical vapor deposition (iCVD) is reported. A molecular force spectroscopy-based method is demonstrated as a rapid and quantitative assessment tool for comparing the differences in antifouling characteristics. The fouling propensity is assessed by using both amine-functionalized and bovine serum albumin-functionalized AFM cantilevers. The molecular force spectroscopy-based method is able to distinguish differences in antifouling capability that is not resolvable by traditional static protein adsorption tests. To lend further insight into the intrinsic fouling resistance of zwitterionic and amphiphilic surface chemistries, Fourier transform infrared spectroscopy, X-ray photoelectron spectroscopy, advancing and receding water contact angles and atomic force microscopy (AFM) are used to elucidate the film properties that are relevant to their antifouling capabilities.

7.2 Introduction

Fouling, the undesirable attachment of organic matters and micro-organisms on submerged surface, has garnered increasing attention due to its prevalence in water purification,[1] marine transportation,[2] medication, and healthcare.[3] Surface modification with organic functional groups that resist non-specific surface attachment has been one of the most environmentally friendly and effective strategies in combatting fouling.

A variety of functionalities that resist protein attachment have been developed, including derivatives of oligo(sarcosine), N-acetylpiperazine, permethylated sorbitol groups, chimeric peptoids (oligomers of peptide structures made of non-natural amino acids) and zwitterionic moieties.[4] These hydrophilic surface chemistries all demonstrated fouling resistance close to polyethylene glycol (PEG), an FDA-approved biopolymer that is often considered as the gold standard in protein resistance.[5] Amphiphilic surfaces represent another interesting category of antifouling chemistry that does not rely on hydrophilicity.[2,6] Their compositional heterogeneities at a molecular-length scale (amphiphilic nanodomains) create a degree of chemical ambiguity, which may lower both the entropic and enthalpic driving forces for protein adsorption.[6,7]

With the very rich and highly diverse library of antifouling surface chemistries, comes the need for a rapid and quantitative assessment tool to compare and evaluate the efficacy of various chemistries.[1,2,8,9] The most accurate way to achieve this goal is to subject the modified surfaces to long-term performance tests in real-world environments. However, it is very time consuming and sometimes not realistic considering the rapid rate at which new antifouling materials are invented.[2,9,10] Single-component fouling tests, such as protein adsorption and bacterial adhesion, are broadly accepted and commonly used as antifouling performance tests.[2,5,11] However, it is tedious and time-consuming to test an antifouling surface against all the possible molecules and organisms that might present in the targeted environment such as seawater or whole blood. Therefore, an efficient and effective fouling test that can reveal the fouling resistance against a wide range of foulants is highly desirable. Such a standardized test can also shed light on the underpinning fouling mechanism of specific foulants. Fast screening for new and more effective antifouling surface characteristics is also possible with such a method.

In this chapter, a reductionist approach was taken to tackle this problem. Instead of sampling numerous foulants, the fundamental building blocks of fouling species (i.e., specific functional moieties that lead to fouling), were used during a molecular force spectroscopy measurement. For example, fouling by humic acid, a natural organic matter that causes severe fouling in water purification, has been attributed to carboxylic acid groups,[12] which were used to decorate an AFM cantilever for the investigation of molecular fouling. Similar experiments were carried out using amine functional groups, a representative moiety of proteins, and also for the model protein, bovine serum albumin (BSA). This methodology represents a quantitative and reproducible way to access fouling resistance against a large library of foulants and screen a collection of antifouling surface chemistries rapidly.

Four types of surfaces were characterized using this method, among which two have been known as antifouling surfaces (amphiphilic and zwitterionic surfaces). Gold and glass surfaces, which are commonly used controls in laboratory testing, were also examined. The amphiphilic and zwitterionic surfaces were synthesized with the same polymerization technique, namely initiated chemical vapor deposition (iCVD, Fig. 7-1).[4,12]

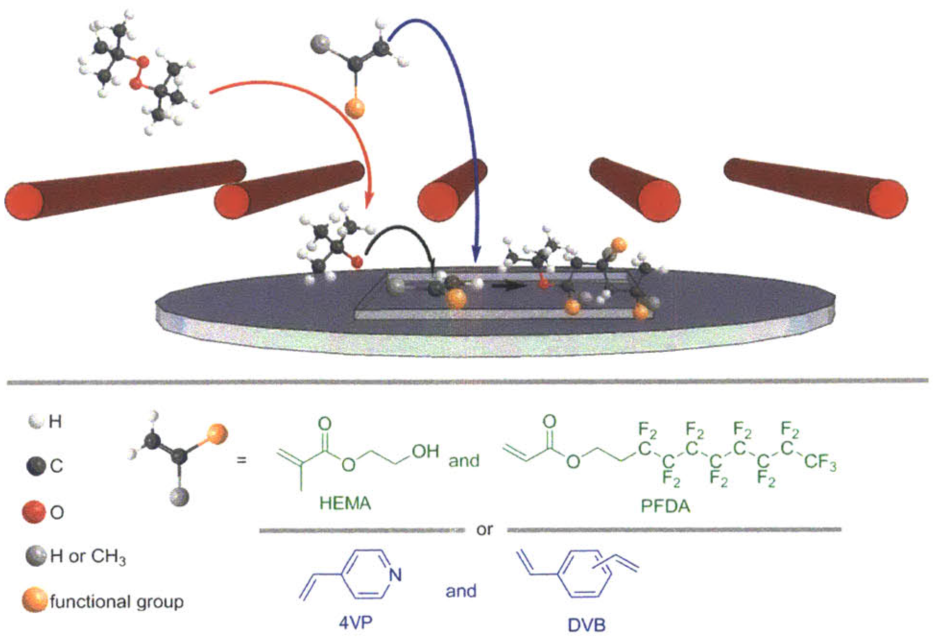

Figure 7-1 | iCVD reaction scheme and monomers used in this chapter. Free radical polymerization is initiated by *tert*-butoxide radical, which is created by decomposing *tert*-butyl peroxide via passing it through resistively heated filaments. Substrates to be modified are placed on a cooled stage. All monomer and initiator species are delivered into the vacuum chamber in the vapor phase.

iCVD is a facile method to carry out free radical polymerization in the vapor phase, enabling the synthesis of insoluble and infusible polymers in a single step. For instance, amphiphilic polymers, which are challenging to synthesize using solution phase methods due to the lack of a common solvent for two comonomers with contrasting solubility, are easily obtained via iCVD with flexible compositional tunability.[6] Zwitterionic polymers with surface-concentrated zwitterionic moieties have been synthesized using iCVD via a two-step scheme.[13-15] The use of the same synthesis method for both types of antifouling surfaces ensures comparable film thickness and morphology. Therefore, differences in fouling resistance can be attributed to film chemistries. Attractive forces on all four surfaces measured by molecular force probe (MFP) correlate very well with their reported short-term and long-term fouling resistance, demonstrating the validity of using MPF as a rapid and quantitative fouling assessment tool.

7.3 Experimental Section

Synthesis of antifouling thin films. All iCVD films were deposited in a custom-built vacuum reactor (Sharon Vacuum), as previously described [14,15]. All the chemicals were used as purchased without further purification. 100 mm-diameter silicon (Si) wafers (Wafer World, test grade) were coated with poly(2-hydroxyethyl methacrylate) (PHEMA), poly(1H,1H,2H,2H-perfluorodecyl acrylate) (PPFDA), poly(HEMA-*co*-PFDA), poly(4-vinylpyridine) (P4VP), poly(divinylbenzene) (PDVB), or poly(4VP-*co*-DVB) without pre-treatment. During iCVD depositions, HEMA (Aldrich, ≥99 mol%), PFDA (Aldrich, 97 mol%), 4VP (Aldrich, 95 mol%) and DVB (Aldrich; the certificate of analysis indicated that this monomer consisted of 56.0 mol% m-DVB, 25.0 mol% p-DVB, and 18.9 mol% ethylvinylbenzene[28]) monomers were heated up to 70 °C, 85 °C, 50 °C and 65 °C in glass jars, respectively and delivered into the reactor using mass flow controllers (1150 MFC, MKS Instruments). *Tert*-butyl peroxide initiator (TBPO; Aldrich, 98 mol%) was delivered using mass flow controllers (MKS Instruments, 1152C) at ambient temperature. Argon patch flow was metered into the reactor through a mass flow controller (1479 MFC, MKS Instruments) and the flow rate was varied to keep the residence time constant.

Films were deposited at a filament (Chromaloy O, Goodfellow) temperature of 250 °C and a stage temperature of 20 °C and 30 °C for zwitterionic and amphiphilic copolymers respectively. Total pressure in the vacuum chamber was maintained at 0.121 Torr for PHEMA, PPFDA, and P(HEMA-*co*-PFDA) and 0.8 Torr for P4VP, PDVB, and P(4VP-*co*-DVB) using a throttling butterfly valve for all depositions. Detailed experimental conditions are included in Table 7-1.

Table 7-1 | Reaction conditions for the copolymers P(4VP-*co*-DVB) and P(HEMA-*co*-PFDA).

P(4VP-co-DVB)	*flow rate [sccm]*	P/P_{sat}	*P(HEMA-co-PFDA)*	*flow rate [sccm]*	P/P_{sat}
4VP	6.3	0.39	*HEMA*	0.45	0.13
DVB	1.4	0.23	*PFDA*	0.03	0.03
TBPO	2.1	0.007	*TBPO*	1.50	0.003
Ar	0.8	0	*Ar*	1.10	0
%DVB	25		*%PFDA*	40	

P/P_{sat} is the ratio of the partial pressure of a reactant to its saturation pressure at the substrate temperature and is indicative of surface concentration.[16,17] After the iCVD deposition, the copolymer P(4VP-*co*-DVB) was derivatized with 1,3-propanesultone (PS; Aldrich, 98 mol%) as described previously to obtain the zwitterionic functionalities.[14,15]

In situ interferometry with a 633 nm HeNe laser source (JDS Uniphase) was used to monitor the film growth and deposit desired thicknesses on Si substrates. A more accurate film thickness on the Si wafer substrates was measured post-deposition using a J.A. Woollam M-2000 variable angle spectroscopic ellipsometry at three different incidence angles (65, 70, and 75°) using 190 wavelengths from 315 to 718 nm. The data were fit using a Cauchy-Urbach isotropic model using WVASE32 modeling software (JA Woollam).

Chemical characterization. FTIR, XPS and contact angle measurements were performed as described previously.[14,15] The thickness of each 1 cm^2 sample used for FTIR analysis was measured prior to obtaining its spectrum. FTIR spectra were obtained using a Thermo Nicolet Nexus 870 spectrometer operated in transmission mode with a deuterated triglycine sulfate KBr detector. Baseline-corrected spectra were collected over 400-4000 cm^{-1} at 4 cm^{-1} resolution and averaged over 256 scans to improve the signal-to-noise ratio and smoothed by averaging 17 adjacent points. Spectra were processed using the OMNIC software package (Thermo Scientific). X-ray photoelectron spectroscopy (XPS) survey scans were obtained using a Kratos Axis Ultra spectrometer equipped with a monochromatic Al $K\alpha$ source and operated at 150 W. The pass energy and step size for the survey scans were 160 eV and 1 eV, respectively. Samples were stored under vacuum for approximately 12 hours before analysis. Pressure during analysis was maintained under 2×10^{-8} Torr, and the analysis areas were 400×750 μm. The spectra were analyzed using the CasaXPS software package. The surface roughness and surface morphology in ambient conditions were characterized using atomic force microscopy (AFM, Veeco, Nanoscope V with Dimension 3100). Tapping mode was employed to prevent damage to the soft materials. The surface roughness and morphology changes when submerged in aqueous environment were measured with 3D Molecular Force Probe (MFP-3D, Asylum Research, Santa Barbara, CA) in phosphate buffered saline (PBS) solution. Special silicon nitride cantilevers (AC40, Bruker, Camarillo, CA) with a spring constant around 0.1 N/m were used, which are designed for liquid imaging.

Fouling resistance of the iCVD thin films and other surfaces. The inertness of the iCVD antifouling coatings was determined using protein adsorption tests and AFM-based force spectroscopy. Uncoated gold and glass surfaces, as well as iCVD amphiphilic and zwitterionic films were incubated in 0.1 g/L fluorescently labelled BSA (BSA-fluorescein isothiocyanate) solutions (PBS-buffered). After two hours, the samples were retrieved and rinsed thoroughly with deionized water. Fluorescent micrographs were obtained with Olympus CX-41 optical microscope.

Attractive forces were measured between amphiphilic, zwitterionic, gold or glass surfaces, and AFM cantilevers that were end-functionalized with spherical SiO_2 colloids coated with 2 nm Cr and 50 nm Au (with colloid end radius R~300 nm, and cantilever nominal spring constant k of 0.06 N/m; Novascan, Ames, IA). The colloidal tips were functionalized with self-assembled monolayers (SAMs) bearing carboxylic acid (-COOH), or amine ($-NH_2$), or BSA. Colloidal force spectroscopy measurement was carried out using a MFP-3D, where a functionalized AFM tip approached an iCVD film or an unmodified surface at a constant AFM piezo displacement rate of 1 $\mu m\ s^{-1}$ in PBS. This process continued until approximately 40 nN compression force was reached. For certain tip-surface pairs, the tip was then held still for a period of 0-10 seconds, namely dwell time, before the tip was retracted from the surface at the same displacement rate as mentioned previously. The maximum adhesion force measured from the retraction portion of the force–distance curves was defined as attractive force between the cantilever and the surface. The measurement was repeated for at least 64 times at different locations for each tip-surface pair.

7.4 Results and Discussion

7.4.1 Synthesis and chemical characterization of iCVD antifouling films

Precursor polymer films containing comonomer pairs of HEMA and PFDA, or 4VP and DVB are deposited using iCVD as the first step of polymer coating synthesis (Fig. 7-1). During a deposition, the two monomer species adsorb onto the surfaces of substrates, which can be described by the Brunauer–Emmett–Teller (BET) isotherm. Therefore, substrates are placed on a temperature-controlled stage that is maintained at room temperature to enhance the monomer adsorption. This cooled stage also protects delicate substrates, particularly the ones with limited thermal stability such as reverse osmosis (RO) membranes, from the heat of filaments suspended above the cooled stage. Filament array is heated during a deposition to break down initiator TBPO and form free radicals and initiate polymerization reactions. A random copolymer is obtained at the end of an iCVD process due to the free radical polymerization mechanism.

Random copolymerization of HEMA and PFDA creates nano-domains of contrasting surface energy (i.e., hydrophilic HEMA domains and hydrophobic PFDA domains),[18] disrupting the adsorption of proteins,[6] bacteria,[19] zoospores and green alga *Ulva*.[2] Successful copolymerization of HEMA and PFDA is evidenced by FTIR spectroscopy (Fig. 7-2a).

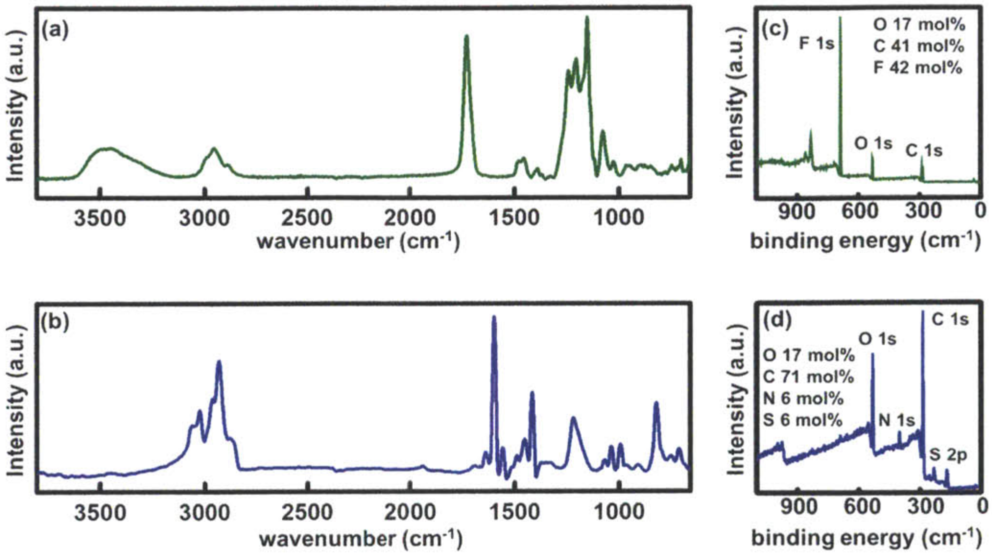

Figure 7-2 | Spectroscopic characterization of iCVD antifouling coatings. a) FTIR spectrum of iCVD amphiphilic copolymer P(HEMA-*co*-PFDA). b) FTIR spectrum of iCVD zwitterionic copolymer P(4VP-*co*-DVB). c) XPS spectrum of P(HEMA-*co*-PFDA). d) XPS spectrum of P(4VP-*co*-DVB).

The peaks at 1152, 1205 and 1241 cm^{-1} are attributed to the symmetric and asymmetric stretches associated with the fluoroalkyl side chains. For detailed peak assignments for this copolymer, the reader is directed to reference 6.[6] It is worth noting that homopolymers of PHEMA and PPFDA have their carbonyl peaks at 1727 and 1731 cm^{-1} respectively; whereas for the copolymer, a single carbonyl peak appears at 1729 cm^{-1} (Fig. 7-2a). This indicates that there is only one carbonyl bonding environment. Therefore, the comonomers truly copolymerized instead of forming a physical blend of homopolymers, which would give rise to two distinct carbonyl peaks. This nature of the copolymer P(HEMA-*co*-PFDA) is also confirmed by the water contact angle measurements in section 7.4.2.

Bulk composition of the amphiphilic copolymer (40 mol% PFDA repeat unit) is quantified by measuring the index of refraction via spectroscopic ellipsometry, as reported previously.[6,20] Specifically, the indices of refraction are measured to be ~1.51 and 1.35 respectively for homopolymers PHEMA and PPFDA. Assuming the index of refraction for the copolymer correlates linearly with the composition of the copolymer, the composition can be calculated with equation (7-1),

$$mol\%_{PFDA} = \frac{1.51 - n_{copolymer}}{0.16} \tag{7-1}$$

where $n_{copolymer}$ represents the index of refraction of the copolymer as measure by ellipsometry; 0.16 is the difference of indices of refraction between PHEMA and PPFDA. The copolymer with 40 mol% PFDA is adopted for further characterization because it has demonstrated the best fouling resistance.[6]

Pyridine-based iCVD zwitterionic coatings have demonstrated excellent fouling resistance and long-term stability. The incorporation of cross-linker DVB is necessary to render the zwitterionic films water-insoluble and stable in strong oxidative conditions.[13] The copolymer P(4VP-*co*-DVB) is functionalized with PS to obtain zwitterionic functionalities, which is evidenced by the FTIR spectrum (Fig. 7-2b). The peaks at 1199 and 1036 cm^{-1} appear after the functionalization, which are attributed to the asymmetric and symmetric stretching of the SO_3^- group in the sulfobetaine moiety. For detailed peak assignments and analysis of the FTIR spectra for this copolymer, the reader is directed to reference 13.[13] The bulk composition of the iCVD zwitterionic copolymer (19 mol% DVB) is calculated from the FTIR spectrum using a method reported previously,[21] with detailed calculations included in Table 7-2. The copolymer with 19 mol% DVB is selected here because it has demonstrated good fouling resistance as well as excellent long-term stability.[13]

Table 7-2 | Calculation of copolymer composition

iCVD films	A_m
homopolymer PDVB	0.040
copolymer P(4VP-co-DVB)	0.0078
$mol\%_{DVB} = (A_m)_{copolymer}/(A_m)_{homopolymer} = 0.0078/0.04 = 0.19$	

7.4.2 Surface characterization of iCVD antifouling films

The copolymer surface composition (top 7 nm) in vacuum (65 $mol\%_{PFDA}$) is probed via XPS (Fig. 7-2c). Despite the thinness (30 nm) of the iCVD amphiphilic coatings, their surface compositions in vacuum differ significantly from bulk compositions. In vacuum, the outward arrangement of fluorinated side chains and inward orientation of the hydroxyl side chains at the copolymer uppermost surface are commonly observed.[6,22,23] This side chain arrangement minimizes the free energy at the polymer-vacuum interface.

The side chain arrangement for the iCVD amphiphilic films is also very dynamic as evidenced during the advancing and receding contact angle measurements (Fig. 7-3a and 7-3b).

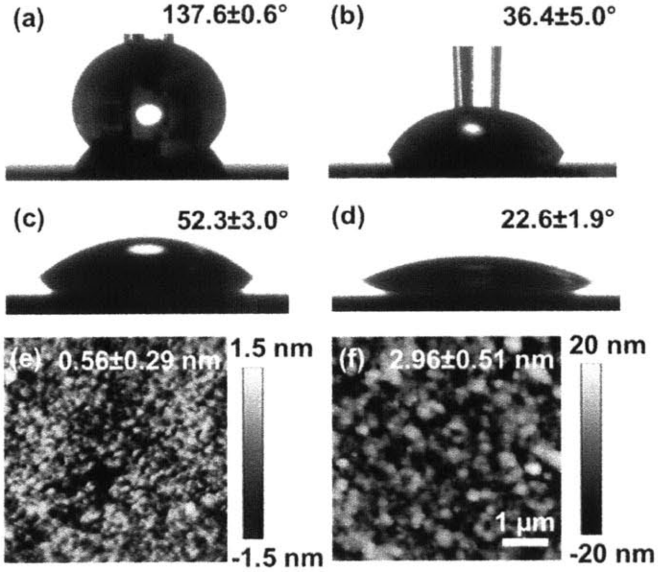

Figure 7-3 | Surface properties of iCVD antifouling coatings. a) water advancing contact angle of iCVD amphiphilic copolymer P(HEMA-*co*-PFDA). b) water receding contact angle of P(HEMA-*co*-PFDA). c) water advancing contact angle of the copolymer P(4VP-*co*-DVB). d) water receding contact angle of P(4VP-*co*-DVB). e) AFM of 30 nm iCVD amphiphilic coating in air. f) AFM of 30 nm iCVD amphiphilic coating in PBS buffer.

During a measurement of advancing contact angle, droplet volume and area in contact with the surface increase simultaneously while a droplet expands on the surface. Therefore, large advancing contact angle (137.6 ± 0.6°) of the iCVD amphiphilic films indicates low surface energy when the amphiphilic film is in the dry state, with the fluorinated side chains oriented outward. On the other hand, the drop volume and surface contacting area decrease during a receding contact angle measurement. Such a measurement therefore assesses the surface energy of a film in its wet state. A small receding contact angle (36.4 ± 5.0°) is observed for the iCVD amphiphilic films, which is likely a result of outward orientation of the hydroxyl side chains and inward arrangement of fluorinated side chains. The large contact angle hysteresis (~101.2°) is greater than all iCVD thin films to the best of our knowledge. It is also worth noting that the advancing and receding contact angles are measured within 1 minute, indicating that the complete switch of surface energy from hydrophobic in air to hydrophilic in water occurs at a very rapid rate.

The rapid surface chain reorientation is also corroborated by the AFM scans of the iCVD amphiphilic surface under dry and wet states (Fig. 7-3e and 7-3f). When measured in air, the root-mean-square (RMS) roughness is 0.56 ± 0.29 nm for an amphiphilic coating with the thickness of 30 nm on polished silicon surface (Fig. 7-3e). When submerged in PBS buffer, the ultra-thin coating undergoes considerable surface chain reorientation, and a greater RMS roughness (2.96 ± 0.51 nm) was observed (Fig. 7-3f). The increased surface roughness can also be attributed to the swelling of the nano-domains composed of HEMA units, which is under the constraints of unchanged hydrophobic PFDA nano-domains.

For the iCVD zwitterionic copolymer, the surface composition (17 $\text{mol\%}_{\text{DVB}}$) quantified via XPS (Fig. 7-2d) matches the bulk composition within experimental error, indicating that surface chain rearrangement is insignificant. This is likely a result of the cross-linked nature of the iCVD zwitterionic copolymers. The homogeneous film composition and limited degree of surface chain reorganization lead to very small water contact angle hysteresis (Fig. 7-3c and 7-3d). The advancing and receding contact angles are 52.3±3.0° and 22.6±1.9° respectively for the iCVD zwitterionic surface (Fig. 7-3c), representing one of the most hydrophilic surfaces enabled by iCVD. The high level of hydrophilicity is due to the strong electrostatic hydration of zwitterions, which is considered the molecular origin of the excellent fouling resistance of zwitterionic chemistry.[11,24,25]

7.4.3 Fouling resistance of iCVD antifouling films

Static protein adsorption test is one of the most prevalent methods to compare fouling resistance across different surface chemistries. Here, four different surfaces (i.e., gold, glass, and iCVD amphiphilic and zwitterionic films) are treated with 0.1 g L^{-1} fluorescently labelled BSA (BSA-fluorescein isothiocyanate) solutions (PBS-buffered) for two hours. After thorough rinsing, fluorescent micrographs are taken to assess the resistance to protein adsorption (Fig. 7-4).

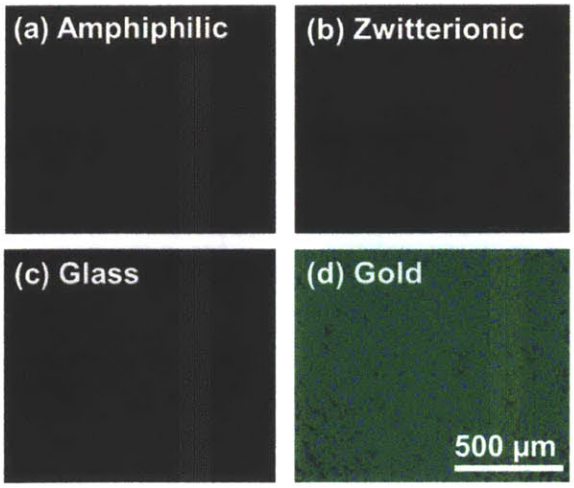

Figure 7-4 | Protein adsorption on iCVD antifouling coatings, glass and gold. All four surfaces were incubated with 0.1 g L^{-1} fluorescein-labeled BSA for two hours and then imaged with fluorescent microscopy. Black background observed in a, b and c indicates no detectable protein adsorption.

Gold surface is entirely covered by BSA, as illustrated by the strong fluorescence in Fig. 7-4d. Glass, iCVD amphiphilic coating and iCVD zwitterionic coating all demonstrate non-detectable protein adsorption (Fig. 7-4a to 7-4c) despite the superior fouling resistance demonstrated by the iCVD zwitterionic coating compare to glass surface during a previous accelerated fouling test.[13] Therefore, the fluorescent imaging technique is able to differentiate a surface with high fouling propensity (such as gold) from one with low fouling propensity (such as glass), but not sufficient to distinguish a surfaces with different antifouling capabilities.

In order to distinguish the antifouling capabilities of different surface chemistries, MFP is selected as an appropriate antifouling assessment tool because it is quantitative, highly sensitive, and compatible with existing materials and equipment without relying on custom synthesis or device fabrication. A set of force-displacement curves as shown in Fig. 7-5a are obtained during a single MFP measurement, where black curve represents the scenario where an AFM cantilever approaches the surface and green curve represents the case where the cantilever retracts from the surface after making a contact.

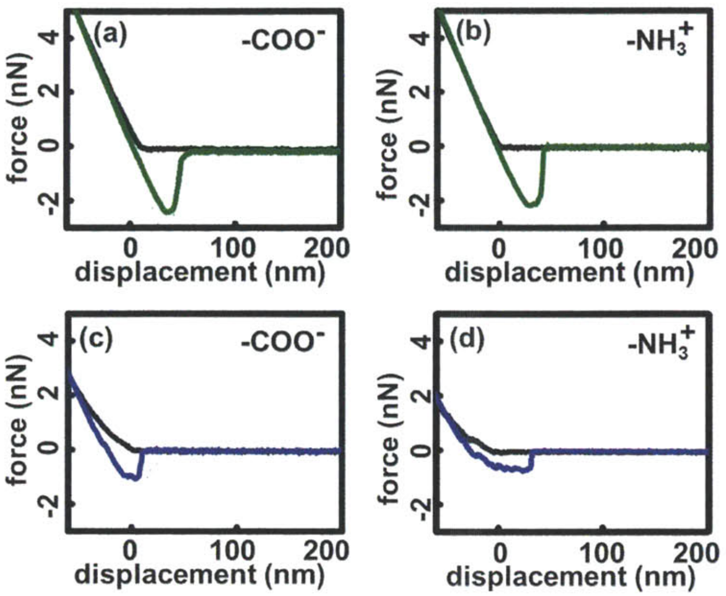

Figure 7-5 | Force-displacement curves of iCVD antifouling coatings recorded during MFP measurements. Black curves represent the case where the functionalized AFM tips are approaching the surface, whereas green curves represent force-displacement recorded during tip retraction for the iCVD amphiphilic copolymer P(HEMA-*co*-PFDA). Likewise, blue curves demonstrate the force-displacement for iCVD zwitterionic copolymer P(4VP-*co*-DVB). The functional groups labeled in each panel indicate the moieties that the AFM tips are functionalized with. Positive and negative force values indicate repulsive and attractive forces respectively.

Panels 7-5a to 7-5d demonstrate representative force-displacement curves for 4 tip-surface combinations: iCVD amphiphilic (green) or zwitterionic (blue) surfaces probed with AFM cantilevers that are end-functionalized with $-COO^-$ or $-NH_3^+$ SAMs (as labelled in each panel). Positive force values represent repulsive force; displacement values indicate distance between an AFM cantilever and the surface to be characterized. All MFP measurements are carried out in PBS buffer at room temperature. The peak force value on the retract curve (i.e., the absolute value of most negative force) is recorded as the attractive force between the specific functionality that presents on the AFM cantilevers and the surface.

At least 64 sets of such force-displacement curves are obtained for each tip-surface combination. Statistics of the attractive forces for the combinations of $-COO^-$ or $-NH_3^+$ tips and iCVD surfaces are shown in Fig. 7-6 in the form of histograms.

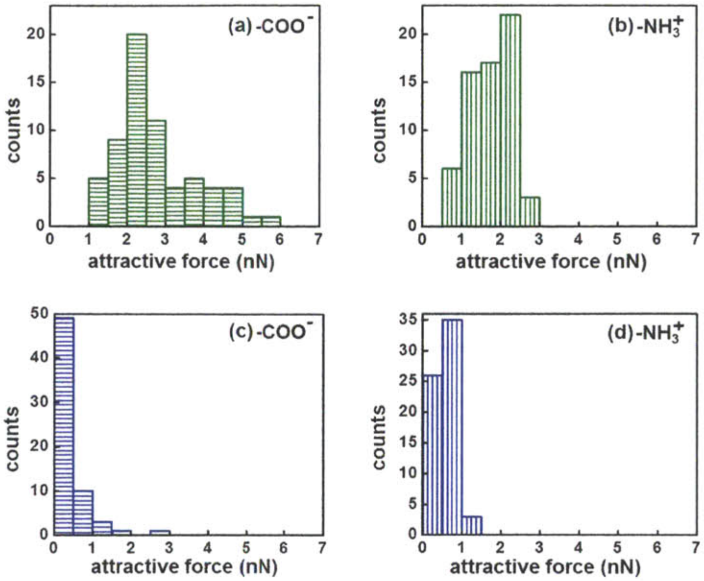

Figure 7-6 | Attractive force distribution measured during MFP tests of iCVD antifouling coatings. 64 tests were carried out for each tip-surface combination. Green bars represent results for the iCVD amphiphilic copolymer P(HEMA-*co*-PFDA) and blue bars represent results for the iCVD zwitterionic copolymer P(4VP-*co*-DVB).

The mean attractive force between the iCVD amphiphilic surface and a carboxylic-acid-functionalized AFM cantilever is 2.92 nN, whereas that for an amine-functionalized AFM cantilever is 1.79 nN. Both attractive forces are small relative to a surface with high fouling propensity, such as gold (Fig. 7-7), for which the mean attractive force is almost an order of magnitude greater than the iCVD amphiphilic surface. A slightly greater attractive force was captured with the carboxylic-acid-functionalized AFM cantilevers compared to that obtained with amine-functionalized tips. This is likely due to the hydrogen bonding between the carboxylic acid groups on the AFM tip and the hydroxyl groups present on the surface of the amphiphilic coating (green molecular structure in Fig. 7-1).

The mean attractive force between the iCVD zwitterionic coating and a carboxylic-acid-functionalized AFM cantilever is 0.43 nN, and that for an amine-functionalized AFM tip is 0.54 nN. The attractive forces are much smaller than those for the amphiphilic surface, indicating a lower fouling propensity on zwitterionic surfaces. The attractive forces obtained with carboxylic-acid-functionalized tips and amine-functionalized tips are comparable within experimental error. This is a good indication of a zwitterionic coating with balanced surface charge, which implies that the vapor-phase derivatization reaction has reached complete conversion. This reaction was carried out to convert the pyridine nitrogen to avzwitterionic nitrogen; without full conversion, the unreacted pyridine nitrogen will result in positive surface charges (with pK_a for its conjugate acid being ~5.25). The neutral surface change is critical to good antifouling performance, because a charged surface can attract foulants with the opposite charge and the electrostatic interaction is a strong driving force for surface fouling.

This test is conducted on glass and gold surfaces and with BSA-functionalized AFM cantilevers. All the attractive forces and statistical analysis are included in box charts (Fig. 7-7).

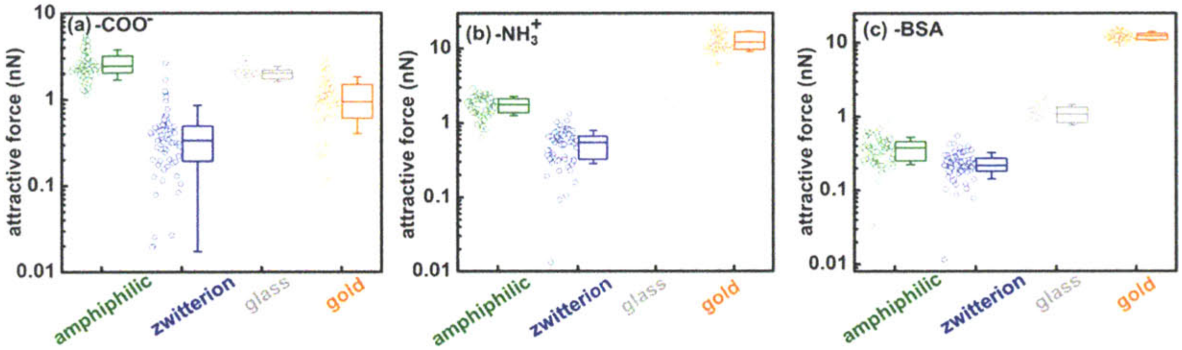

Figure 7-7 | Attractive forces and their distributions for iCVD antifouling coatings, glass and gold surfaces. The functional groups labeled in each panel indicate the moieties that the AFM tips are functionalized with. Positive and negative attractive force values indicate attractive and repulsive forces respectively. The upper and lower boundaries of each box indicate the 25 and 75 percentiles respectively. The horizontal bar inside each box represents the median.

The bottom and top of the box indicate the 25% and 75% percentiles (i.e., first and third quartiles), and the band inside the box is the median (i.e., second quartile). Circles to the left of the box charts are the attractive force values calculated from at least 64 sets of force-displacement curves. Four surfaces measured with the same type of functionalized AFM cantilever are compared simultaneously in one panel. The iCVD zwitterionic surface has the smallest molecular interaction with all the functionalized tips, which indicates that the zwitterionic surface likely has the strongest fouling resistance.

It is interesting to note that the iCVD amphiphilic surface has greater interaction with –COO$^-$ but smaller interaction with –NH$_3^+$ compared to bare glass. However, its interaction with the BSA-functionalized AFM tips is smaller than that of glass. In addition, the relative strengths of interactions across four different surfaces have similar trends for $-NH_3^+$ and BSA-functionalized AFM cantilevers. That is, for both types of cantilevers, the zwitterionic surface has the smallest interaction, and the amphiphilic surface has the second smallest interaction, whereas the interaction with gold surface is more than an order of magnitude greater than that of the zwitterionic surface. Under the pH of 7.4 (PBS buffer), the surface of BSA is negatively charged, while the amine functional groups are positively charted. Therefore, the similar trend is not due to the electrostatic interactions. Thus, it can be inferred that the dominating interaction during the surface adsorption of BSA is not electrostatic force, and it is highly possible that amine-mediated specific interactions represent a significant factor in the surface fouling by BSA. Therefore, MFP measurements conducted with amine-functionalized AFM cantilevers can capture the protein fouling propensity of various surfaces and serve as a versatile assessment tool for the comparison of antifouling capabilities and for the fast screening of novel antifouling surface chemistries.

7.5 Conclusion

Two types of distinct antifouling chemistries, namely amphiphilic and zwitterionic copolymers, are synthesized via iCVD in the form of ultra-thin film coatings. The film composition, architecture, hydrophilicity, and surface chain mobility are discussed in the context of their correlations with surface antifouling properties. Attempts are made to compare the fouling resistance with the widespread static protein adsorption method. However, this method is proven insufficient to distinguish different antifouling capabilities of surfaces with inherent fouling resistance. Therefore, molecular force spectroscopy is applied to evaluate the fouling resistance of the iCVD antifouling surfaces as well as control surfaces with different fouling propensities. The building blocks of various fouling species, specifically carboxylic acid and amine functional groups, are attached to AFM cantilevers and the molecular interactions with all four surfaces are quantified with MFP. The superior fouling resistance of the zwitterionic chemistry, in comparison to the amphiphilic chemistry and a smooth and hydrophilic glass surface, is clearly manifested with this characterization method. The antifouling capabilities of all four surfaces measured with amine-functionalized AFM cantilevers correlate very well with that measured with BSA-functionalized tips. This MFP-based method represents a rapid and quantitative fouling assessment tool for the evaluation and comparison of the vast diversity of existing antifouling chemistries. It is worth noting that the key assumption of this characterization method is that different fouling species have the same probability to attach to a certain surface when they are immobilized on a cantilever as when they are free in the solution and in the presence of other fouling species. Future work will focus on the detailed assessment of these effects on the molecular force interactions and surface fouling.

References

1. Elimelech, M. & Phillip, W. A. *Science* **333,** 712-717, (2011).
2. Callow, J. A. & Callow, M. E. *Nat Commun* **2,** 244, (2011).
3. Smith, R. S. *et al. Science Translational Medicine* **4,** 153ra132, (2012).
4. Yang, R., Asatekin, A. & Gleason, K. K. *Soft Matter* **8,** 31-43, (2012).
5. Banerjee, I., Pangule, R. C. & Kane, R. S. *Adv. Mat.* **23,** 690-718, (2010).
6. Baxamusa, S. H. & Gleason, K. K. *Adv. Funct. Mat.* **19,** 3489-3496, (2009).
7. Krishnan, S. *et al. Langmuir* **22,** 5075-5086, (2006).
8. Shaffer, D. L. *et al. Environmental Science & Technology* **47,** 9569-9583, (2013).
9. Fritzmann, C., Löwenberg, J., Wintgens, T. & Melin, T. *Desalination* **216,** 1-76, (2007).
10. Natalio, F. *et al. Nat Nano* **7,** 530-535, (2012).
11. Jiang, S. & Cao, Z. *Adv. Mat.* **22,** 920-932, (2010).
12. Coclite, A. M. *et al. Adv. Mat.* **25,** 5392-5423, (2013).
13. Yang, R., Jang, H., Stocker, R. & Gleason, K. K. *Advanced Materials* **26,** 1711-1718, (2014).
14. Yang, R., Xu, J., Ozaydin-Ince, G., Wong, S. Y. & Gleason, K. K. *Chem. Mater.* **23,** 1263-1272, (2011).
15. Yang, R. & Gleason, K. K. *Langmuir* **28,** 12266-12274, (2012).
16. Lau, K. K. S. & Gleason, K. K. *Macromolecules* **39,** 3688-3694, (2006).
17. Lau, K. K. S. & Gleason, K. K. *Macromolecules* **39,** 3695-3703, (2006).
18. Amadei, C. A., Yang, R., Chiesa, M., Gleason, K. K. & Santos, S. *ACS Applied Materials & Interfaces*, (2014).
19. Matin, A. *et al. Separation and Purification Technology* **124,** 117-123, (2014).
20. Ozaydin-Ince, G., Matin, A., Khan, Z., Zaidi, S. M. J. & Gleason, K. K. *Thin Solid Films* **539,** 181-187, (2013).
21. Petruczok, C. D., Yang, R. & Gleason, K. K. *Macromolecules* **46,** 1832-1840, (2013).
22. Coclite, A. M., Shi, Y. & Gleason, K. K. *Advanced Functional Materials* **22,** 2167-2176, (2012).
23. Coclite, A. M., Shi, Y. & Gleason, K. K. *Advanced Materials* **24,** 4534-4539, (2012).
24. Holmlin, R. E., Chen, X. X., Chapman, R. G., Takayama, S. & Whitesides, G. M. *Langmuir* **17,** 2841-2850, (2001).
25. Tegoulia, V. A., Rao, W., Kalambur, A. T., Rabolt, J. F. & Cooper, S. L. *Langmuir* **17,** 4396-4404, (2001).

CHAPTER EIGHT

Conclusion

8.1 Conclusion and Outlook

The fabrication of effective antifouling reverse osmosis (RO) membranes and the new concept of synergistic fouling resistance have been demonstrated for the first time in this thesis, which resolves the bottleneck of biofouling for seawater desalination. This thesis provides both scientific insights and practical solutions to the global problems of compromised device performance resulted from biofouling and fresh water scarcity for sustainability.

The successful fabrication of antifouling RO membranes relies on the enabling technology, initiated chemical vapor deposition (iCVD). In this thesis, antifouling zwitterionic chemistry was developed with iCVD for the first time, and has become an active and important component in the rich library of iCVD chemistry. Specifically, iCVD zwitterionic coatings were applied to commercially available RO membranes without jeopardizing the membrane performance (i.e., water permeability and salt rejection; CHAPTER TWO). The as-modified RO membranes demonstrated excellent fouling resistance to a range of common species including components in natural organic matters, extracellular matrixes, proteins and bacteria. Insights into the fine film architecture revealed the structure-property correlations for the iCVD zwitterionic coatings and attributed the antifouling properties to the surface-concentrated zwitterionic moieties resulted from a diffusion-limited vapor phase functionalization reaction (CHAPTER THREE).

Chlorination is the most prevalent disinfection and a very important antifouling strategy in water industry. However, the iCVD zwitterionic coatings lack chlorine tolerance because the ester bonds in the methacrylate repeat units are susceptible to oxidation by hypochlorite. Therefore, a novel pyridine-based zwitterionic structure was designed for better chemical stability. Special attention was paid to ensure the monomer precursors, 4-vinylpyridine and divinylbenzene (DVB), are prevalent and cost-effective. Despite the prevalence of the copolymer, characterization of its composition is not trivial to conduct due to various isomers of DVB that are extremely difficult to separation. Beer-Lambert and Finemann-Ross equations were adapted from solution free-radical polymerization to describe the surface polymerization during iCVD, with which the copolymer composition can be calculated based on FTIR spectra (CHAPTER FIVE).

The pyridine-based zwitterions were used as antifouling chemistry for the first time and demonstrated excellent fouling resistance as well as stability. Stress tests were conducted where the new zwitterionic films were treated with 1,000 ppm chlorine solution for as long as 24 hours. The films remained chemically and morphologically unchanged after the treatment, which enabled the very interesting observation of synergistic antifouling when chlorination and surface coating were adopted simultaneously (CHAPTER SIX). The antifouling performance can be enhanced by 10 folds during the combination treatment compared to the performance when simple multiplicative effects are assumed. This represents the first observation of synergy in antifouling applications, which opens up a whole new area where a vast diversity of combinations of antifouling strategies can be used simultaneously to gain drastically improved performance.

A key advantage of the iCVD zwitterionic coatings is the substrate-independence of the vapor application process, which makes these coatings easily applicable to numerous applications where both inertness and stability are essential.

The broad-spectrum fouling resistance of iCVD surfaces was demonstrated with a reductionist approach, molecular force spectroscopy and the fouling resistance can be tested under harsh, high-salinity conditions.

Another example involves the organic functionalization of silicon. Surface of silicon was passivated and functionalized with organic molecules at room temperature by transferring the surface grafting scheme developed for commercial RO membranes (CHAPTER FOUR). The iCVD passivation method led to the lowest surface recombination velocity reported to date for air-stable organic passivation, which can benefit a wide range of industries ranging from semiconductor devices to clean energy production.

The iCVD zwitterionic chemistries and the new synergistic approach to antifouling are transferrable to many other applications including the design of highly efficient and specific separation processes and performance enhancement of electrochemical reactors. The ability to nondestructively deposit conformal layers on virtually any substrate can greatly facilitate the integration of antifouling coatings into existing products. Most importantly, the coating fabrication and the synergistic strategy are compatible with existing membrane and water purification infrastructure, which will have important industrial and ultimately societal implications by enabling the advancement of low-cost seawater desalination in water-scarce areas.

An important problem yet to be solved in seawater desalination is the poor chlorine resistance of the commercial TFC membranes. The energy consumption of the RO process alone is very close to the theoretical minimum, but the overall energy consumption and capital investment for an RO plant are not ideal for the wide-spread installation of RO worldwide. The root of these problems resides in the membranes' sensitivity to chlorine damage. The pretreatment processes, chlorine-removal and re-chlorination infrastructures are necessary to protect RO membranes. The new chlorine-resistant antifouling coatings bring hope to the next-generation chlorine-tolerant and antifouling RO membranes. However, more work needs to be done to improve the membrane itself. In particular, the chlorine-resistant zwitterionic coatings may be applied on the latest salt-rejecting layers,[1-3] which resist exposure to chlorine.

Surging population growth, urban development and vast industrialization will increase fresh water demand worldwide and the need for new source of fresh water is urgent. The existing freshwater augmentation means, such as water conservation, water recycle and reuse and regional transportation alone may not be sufficient to meet the need. Seawater desalination provides a potential solution by obtaining fresh water from the vast oceans and can be economically favorable if the biofouling and chlorine tolerance issues are successfully resolved. The materials and strategies developed in this thesis will help eliminate the most energy- and chemical-intensive step, pretreatment of seawater, in a RO plan and reduce the environmental impacts of brine discharge. The substrate-independent and scalable iCVD approach therefore promises to lower the price of freshwater in water-scarce countries, where desalination may serve as the only viable means to provide the water supply necessary to sustain agriculture, support personal consumption, and promote economic development.

References

1. Olenych, S. G., Moussallem, M. D., Salloum, D. S., Schlenoff, J. B. & Keller, T. C. S. *Biomacromolecules* **6,** 3252-3258, (2005).
2. Salloum, D. S., Olenych, S. G., Keller, T. C. S. & Schlenoff, J. B. *Biomacromolecules* **6,** 161-167, (2004).
3. Holt, J. K. *et al. Science* **312,** 1034-1037, (2006).

APPENDIX A

Probing nano-scale heterogeneities of iCVD amphiphilic copolymers

A.1 Abstract

Undesired bacterial adhesion and biofilm formation on wetted surfaces leads to significant economic and environmental costs in various industries. Amphiphilic coatings with molecular hydrophilic and hydrophobic patches can mitigate such biofouling effectively in an environmentally friendly manner. The coatings are synthesized by copolymerizing (Hydroxyethyl)methacrylate and perfluorodecylacrylate via initiated chemical vapor deposition (iCVD). In previous studies, the size of the patches was estimated to be ~1.4-1.75 nm by fitting protein adsorption data to a theoretical model. However, no direct observation of the molecular heterogeneity exists and therefore the origin of the fouling resistance of amphiphilic coatings remains unclear. In this appendix, the amphiphilic nature is investigated by amplitude modulation atomic force microscopy (AM-AFM). High resolution images obtained by penetrating and oscillating the AFM tip under the naturally present water layer with sub-nanometer amplitudes reveal, for the first time, the existence of amphiphilic nanodomains (1-2 nm^2). Compositional heterogeneity at the nano-scale is further corroborated by a statistical analysis on the data obtained with dynamic AM-AFM force spectroscopy. Variations in the long range attractive forces, responsible for water affinity, are also identified. This nanoscopic results on the polymers wettability are also confirmed by contact angle measurements (i.e. static and dynamic). The unprecedented ability to visualize the amphiphilic nano-domains as well as sub-nanometer crystalline structures provides strong evidence for the existence of previously-postulated nanostructures, and shed light on the underlying antifouling mechanism of amphiphilic chemistry.

A.2 Introduction

Surfaces which resist biomolecule and microbe adsorption are highly sought after for tissue engineering, medical implants and drug delivery systems, as well as for marine antifouling, water purification and desalination membranes, and other industrial applications.[1]

It is known that hydrophilic building blocks or electrostatic hydrated zwitterionic groups[2] display low values of polymer/water interfacial energy, diminishing the adsorption of biofilms. Hydrophobic membranes, on the other hand, are characterized by higher values of interfacial energy and they tend to adsorb biofilms in order to reach thermodynamic equilibrium.[3] Nevertheless, hydrophobic membranes are widely used in industrial applications for their lower degradation rate and higher chemical stability compared to hydrated membranes.[4] A dichotomic anti-biofouling coating that displays solely hydrophilic or hydrophobic properties might not be adequate due to the intrinsic amphiphilic nature of large organism (e.g., bacteria) or biopolymer. On the other hand, surfaces with compositional heterogeneities have been hypothesized to resist adsorption, provided the length scale of surface domains is smaller than the region of contact between the foulant and the surface. [5,6] The alternation of hydrophilic and hydrophobic domains is postulated to limit thermodynamically favorable interactions between the foulant and the surface, hence reducing adsorption.[7,8].[9,10] However, disruption of protein adsorption requires compositional heterogeneity at the nanoscale, [2,11]to create a mismatch between the nano-domains and the anchoring sites of the protein.[12]

Amphiphilic protein-repellant surfaces have been successfully fabricated by copolymerization of hydrophilic 2-hydroxyethylmethacrylate (HEMA) and hydrophobic (*1H,1H,2H,2H*-perfluorodecyl)acrylate (PFDA), through initiated chemical vapor deposition (iCVD)[9]. In this appendix, CVD was used to synthesize thin films of the pure homopolymer pHEMA, the pure homopolymer pPFDA, and copolymers of HEMA and PFDA which spanned the entire compositional range in between. These surfaces were extensively characterized to determine composition, morphology, swelling, and contact angle properties. On the hydrophilic pHEMA, the BSA uptake reduced by 75% as compared to the hydrophobic pPFDA. All of the amphiphilic surfaces measured displayed an even lower BSA uptake than pHEMA. The copolymer composition with 40% PFDA displayed the lowest BSA uptake, with a reduction of 95% as compared to the pPFDA surface. In this initial study, the substrates were silicon wafers. In follow-up work, the same compositional range of thin films were deposited directly on the polymeric reverse osmosis membranes.[13] The ability of these CVD coated membranes to resist bacterial adhesion was studied and again the copolymer deposited from the 40% PFDA provided the best antifouling performance.

BSA protein is a globular protein that exhibits a structure made of hydrophilic and hydrophobic patches.[14] BSA predominantly exposes hydrophilic patches toward the surface that are rich of hydrophilic residues and hydrophobic patches towards the interfaces which display hydrophobic nature. This phenomenon increases protein/surface interaction. On the other hand, in the case of copolymers, the creation of surface ambiguity with molecular heterogeneity comparable to the dimension of the patches limits favorable interactions. While nano-domains responsible for the low protein adsorption were not directly visualized in the previous study,[9] a random lattice model was used to estimate the average size to be ~ 1.4-1.75 nm. The model successfully explained the experimental observation of the minimal BSA adsorption with 40% PFDA content. This composition also resisted the attachment of *Escherichia coli* (*E.coli*).[13]

In this appendix, direct visual evidence of nano-scale surface compositional domains on the iCVD amphiphilic surfaces (i.e. copolymer HEMA/PFDA) is provided. To achieve this goal, the investigation techniques must meet three requirements: 1) high lateral resolution imaging, i.e. ≈1-2 nm; 2) minimal sample invasiveness of soft matter; 3) spectroscopic-like capabilities for the identification of compositional heterogeneity and, possibly, for the detection of the accumulation of adsorbed water layers on the hydrophilic domains. In order to meet these requirements, we employ a recently-reported high resolution and minimally invasive mode of amplitude modulation atomic force microscopy (AM-AFM) operated under ambient conditions, i.e. Small Amplitude Small Set-point (SASS).[15] In this imaging mode, the cantilever oscillates near the surface with oscillation amplitude on the order of sub- nanometer (please refer to section A.3). This allows resolving the molecular heterogeneities of random amphiphilic thin polymers, something not achievable with traditional imaging mode (i.e. Non-Contact NC mode). Requirements 2 and 3 are simultaneously addressed by employing phase contrast imaging and force spectroscopy while carefully controlling peak forces.[16] Furthermore, we define nano-scale observables that provide information about the presence or absence of chemical heterogeneity on the samples and we corroborate these results with macroscopic contact angles measurements.[17]

A.3 Experimental Section

Film preparation. All iCVD films were deposited in a custom built vacuum reactor (Sharon Vacuum), as previously described.[2,18,19] Thermal excitations of the initiator were provided by heating a 0.5 mm Nickel/Chromium filament (80% Ni/ 20% Cr, Goodfellow) mounted in a parallel array and the temperature was measured by a thermocouple attached to one of the filaments. The filament holder straddled the deposition stage which was maintained at a set point temperature using water cooling. The vertical distance between the filament and the stage was 2 cm.

All the chemicals were used as purchased without further purification. Silicon (Si) wafers (Wafer World, test grade) were coated without pre-treatment. During iCVD depositions, *tert-*

butyl peroxide (TBPO, Aldrich, 97%) initiator and the nitrogen patch flow were fed to the reactor at room temperature through mass flow controllers (1479 MFC, MKS Instruments) at 1.5 sccm and 1.1 sccm respectively. 2-Hydroxyethylmethacrylate (HEMA, Aldrich, 97%) and *1H,1H,2H,2H*-perfluorodecyl acrylate (PFDA, Aldrich, 97%) monomers were heated in a glass jars up to 75 °C and 80 °C respectively, and delivered into the reactor using needle valves. Systematic variation of the flow rate ratios was performed to yield copolymers with various compositions. Films were deposited at a filament temperature of 250 °C and a stage temperature of 30 °C. Total pressure in the vacuum chamber was maintained at 0.121 Torr for all depositions.

In situ interferometry with a 633 nm HeNe laser source (JDS Uniphase) was used to monitor the film growth and deposit the desired thicknesses on Si substrates. A more accurate film thickness measurement on the Si wafer substrates was made post-deposition using a J.A. Woollam M-2000 spectroscopic ellipsometer at three different incidence angles (65, 70, and 75°) using 190 wavelengths from 315 to 718 nm. The data were fit using a Cauchy-Urbach model.

SASS imaging. Recently, two groups[15,20] have independently demonstrated that it is possible to scan under the water layer universally present when a surface is exposed to ambient condition. This allows increasing resolution and minimizing conservative and dissipative peak forces.[21] Remarkably similar results have been shown in the two common modes of dynamic operation respectively, namely AM[15] and frequency modulation FM AFM.[20] One of these two modes is referred as Small Amplitude Small Set-point (SASS). SASS has been shown to maximize resolution without the requirement of intrinsic 3-dimensional lattice periodicity or sufficient stiffness of the sample.[15,22,23,24,25] SASS technique consists in imaging with sub-nanometer oscillation amplitudes, free amplitudes in the range of 1-5 nm and sharp tips with radii smaller than 5 nm. Under these conditions, the tip oscillates in the proximity of the surface. Moreover, small cantilevers (*OLYMPUS 55TS*) were employed to reduce thermal noise while imaging in SASS.[26] While these cantilevers were very stiff, i.e. $k \approx 170$ N/m, the maximum energy dissipated per cycle in SASS was less than 1.7 eV throughout.

Reconstruction of force profile in AM AFM. The ability to recover the tip-sample interaction as a function of tip-sample distance (d_m) from observables is generally defined as the reconstruction of nano-scale force profile.

The experiments have been carried out using *Asylum Research Cypher Scanning Probe Microscope*. The silicon cantilevers' parameters (*OLYMPUS 55TS*) are: $k\approx 150N/m$, $Q\approx 700$, $f=f_0\approx 1.9$ *MHz and* $R\leq 5nm$. The size of the tip (R) has been constantly monitored *in situ* by following the onset of the transition from the attractive to the repulsive regime, i.e. A_C method.[27] The force reconstruction exploits Katan-Sader-Jarvis formalism[28] (eq. (7-2)) in which the force versus distance profile is recovered from the variations in the frequency shift Ω that occur by decreasing the cantilever-sample separation (z_c). Then from z_c is possible to obtain the tip/sample distance d_m by subtracting the perturbed oscillation amplitude A:

$$d_{\min} \approx z_c - A \tag{7-1}$$

The normalized conservative force F_{ts}^* as function of d_m reads:

$$F_{ts}^*(d_m) = \frac{2k}{|F_{AD}|}\int_{u=d_m}^{u=\infty}\left[\left(1+\frac{A^{1/2}}{8\sqrt{\pi(u-d_m)}}\right)\Omega(u) - \frac{A^{3/2}}{\sqrt{2(u-d_m)}}\frac{d\Omega(u)}{du}\right]du \tag{7-2}$$

where the force has been normalized with the absolute value of the force of adhesion $|F_{AD}|$ and where Ω is the normalized frequency expressed by:

$$\Omega(d_m) = \left[1+\frac{A_0}{QA}\cos(\Phi(d_m))\right]^{\frac{1}{2}} - 1 \tag{7-3}$$

where A_0 is the free or unperturbed amplitude of oscillation and Φ is the phase lag relative to the driving force. The free amplitude, A_0, is a key parameter to avoid bi-stability and discontinuity in the amplitude-phase-distance (APD) curves. For *OLYMPUS 55TS*, the value of A_0 needed to avoid bistability was less than 5 nm.

The normalized energy dissipated per cycle, E_{dis}^*, is estimated with the standard equation:[29,30]

$$E_{dis}^* = \frac{\pi k A_0 A}{E_{dis}(Max)Q}\left[\sin(\Phi) - \frac{A}{A_0}\right] \tag{7-4}$$

where $E_{dis}(Max)$ corresponds to maxima in the APD curve, and can be plotted versus d_m to highlight particular long range dissipative process (i.e. capillary).

Contact angle measurements. The contact angle measurement was executed with a Krüss FM40Mk2 EasyDrop contact angle instrument and static contact angles were measured using 2 μL DI water droplets. The data for each polymer refers to a series of 5 measurements. Advancing and receding contact angles were measured by recording the advancing and receding of the contact line, while increasing or decreasing the droplet volume by means of the sessile drop method.[31] The initial volume was set to 2 μL and the volume of the droplet is increased up to 5μL, after which the receding phase was evaluated.

A.4 Results and Discussion

Table A-1 summarizes the HEMA and PFDA content for the four polymers investigated in this appendix. In particular, each polymer has been labeled in respect to its hydrophobic content (i.e. for F40 the hydrophobic content is equal to 40%).

Table A-1| HEMA and PFDA content for the four polymers

Type	Label	% $_{\text{PFDA}}$	% $_{\text{HEMA}}$	Normalized protein adsorption (%)	Static Contact Angle (deg)	Advancing Contact Angle (deg)	Receding Contact Angle (deg)	Hysteresis (deg)
Hydrophilic homopolymer	F0	0	100	25	65.8±2.1	82.3±0.9	22.5±1.4	59.3±1.3
Amphiphilic copolymer	F40	40	60	5	115.1±0.5	122.1±0.3	26±1.8	96.1±1.5
Amphiphilic copolymer	F75	75	25	20	123.0±0.2	123.4±0.6	70.7±1.7	52.7±1.6
Hydrophobic homopolymer	F100	100	0	100	123.2±0.6	128.7±0.4	81±2	45±4

In the previous study[9], protein adsorption onto the polymer films was measured by a quartz crystal microbalance with dissipation monitoring (QCM-D, Model E4, Q-sense). This work shows that the amphiphilic copolymer, F40 is superior in resisting BSA protein adsorption as compared to either the hydrophilic (F0) or hydrophobic homopolymers(F100) respectively.[9] The normalized protein adsorption results are summarized in Table A-1. We note that the hydrophobic homopolymer is characterized by the higher protein adsorption. This is due to the fact that apolar surfaces destabilize the BSA proteins, facilitating their unfolding, and leading to strong inter-protein and protein-surface interactions.[32]

It can be argued that imaging in the NC mode of operation in AM AFM is preferable for soft matter imaging.[16] The NC mode is experimentally reached by sufficiently decreasing the free amplitude, i.e. typically ~ to 1 nm, while keeping the set-point as high as possible.[33] On average, in the NC mode the tip oscillates higher above the sample so there is no mechanical contact and/or sample deformation.[33] A drawback of the NC imaging mode is that compositional contrast via the phase channel might be limited or minimal. A second drawback is the origin of contrast in NC imaging mode even in topography, i.e. long range unlocalized interactions. Unlocalized interactions (i.e. van der Waals) limit lateral resolution and might even negatively affect apparent height reconstruction.[34] The limitations of NC mode imaging might be particularly pronounced in ambient conditions since nano-scale water films covering the tip's and the sample's surfaces screen the forces originating from the sample.[35] Traditional NC imaging methods are limited in resolution since they operate with long range non-localized forces (Fig. A-1b, top) and therefore are not appropriate for visualizing nano- and sub-nano-scale features. Thanks to its sub-nanometer oscillation amplitudes, SASS mode of operation is sensitive to more localized forces and, as seen in Fig. A-1b, bottom, it can resolve nano-domains on the F75 copolymer with phase contrast of more than 20°. In Fig. A-1b, the transition from the NC mode ($A_{sp}\approx1.5$ nm) to the SASS mode ($A_{sp}\approx0.4$ nm) was induced while acquiring the image by sufficiently reducing the oscillation amplitude A_{sp} (Fig. A-1a) while keeping A_0 constant at $A_0\approx1.7$ nm as recently reported.[15]

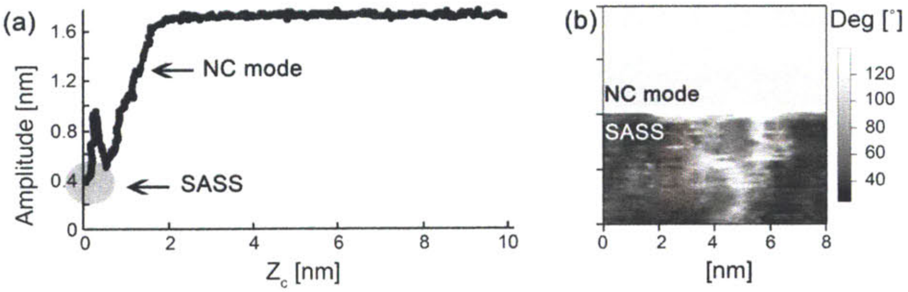

Figure A-1| Experimental amplitude curve obtained as a function of cantilever separation z_c with a standard AC55TS (OLYMPUS) cantilever on the F75 (a). In (b), the phase contrast channel shows that nanoscale structures with lateral dimensions on the order of 1 nm are resolved in the SASS mode of imaging (bottom of the image contrast >60°) while no contrast is observed in the NC mode (top of the image contrast <0.5°)). The transition from NC mode to the SASS mode was induced by simply reducing the set point from ≈ 1.5 nm (NC mode) to ≈0.4 nm (SASS mode) as predicted in (a). The free amplitude was $A_0\approx1.7$ nm.

The SASS mode was then utilized to acquire 10x10 nm phase images with 256 by 256 pixel resolution (Fig. A-2) for the 4 polymers listed in Table A-1. Phase contrast is sensitive to surface compositional variation and it can be converted to energy dissipation maps between the tip and the surface during each oscillation cycle.[36,29] Phase contrast images have been employed here on all the coatings with various compositions. While several images in SASS were obtained for each polymer, those shown in Fig. A-2 are representative scans of the coatings and therefore are the focus of the following discussion. Hydrophilic homopolymer (F0, Fig. A-2a). The phase contrast is not significant for F0 compared to F40 (Fig. A-2b), F75 (Fig. A-2c) and F100 (Fig. A-2d) even in SASS. The distribution of phase values is shown in Fig. A-2f with the mean value at ~65°. This coating composition has the lowest standard deviation in phase contrast out of the four coating compositions, i.e. $\sigma=2.3°$. The qualitative observations and quantitative results obtained for this sample are in accordance with the homogeneous chemical composition of the surface. Thus, these results can be regarded as direct evidence of the absence of nano-scale domains in terms of compositional variations or heterogeneity.

Amphiphilic copolymers (F40, Fig. A-2b and F75, Fig. A-2c and A-2e). The images display domains on the order of 1-2 nm^2. Furthermore, the phase values are broadly distributed (Fig. A-2f and A-2g) indicating that the origin of the contrast is compositional heterogeneity. The broadened distribution of phase values is evidenced quantitatively by the standard deviations values of 12.1° for F40 and 10.9° for F75; the 95th percentiles are 58.3° and 75.2° for F40 and F7 5respectively. The enhanced phase contrast confirms the surface chemical heterogeneity characteristic of the copolymers P(HEMA-*co*=PFDA) while the nano-scale dimensions of the domains are confirmed from dimensions of the features in the phase images, which are measured to be 1-2 nm^2.[11] This size is consistent with the values inferred from a random lattice model (i.e., 1.4-1.75 nm).[37]In summary, the combination of these findings supports a correlation between the presence of chemical heterogeneous nano-domains and low values of protein adsorption for the copolymers. The nano-domains thermodynamically discourage the adsorption of protein due to low surface/protein interaction. Moreover, the heterogeneity minimizes protein conformational re-organization. If this reorganization had happened, the protein would have increased its entropy, leading to a spontaneous adsorption process (i.e. Gibbs free energy less than zero).[38] In Fig. A-2e, an increased scanning area (20x20 nm) for the F75 copolymer also shows the nano-domains structure. Thus, these results can be regarded as direct evidence of the presence of nano-scale domains in terms of compositional variations or heterogeneity.

Hydrophobic homopolymer (F100, Fig. A-2d). Surprisingly, significant phase contrast is also observed for this homopolymer. The images reveal unique lamellar (yellow lines) and hexagonal features (red hexagon) pointed out with the arrows. The standard deviation here is approximately 14.2° (Fig. A-2i). The phase contrast here can be explained by the tendency of the iCVD pPFDA polymers to form crystalline structures. The mesomorphic state of the heptadecafluorodecyl (C_8F_{17}) group in the side chain of a PFDA repeat unit has an ordered smectic liquid crystalline (LC) structure in the Smectic B phase consisting of a succession of bilayers.[39,40] Each bilayer is composed of two heptadecafluorodecyl groups without interpenetrating and thus has the characteristic thickness of 3.2 nm, precisely twice the length of extended heptadecafluorodecyl groups[37] The heptadecafluorodecyl groups are oriented perpendicularly to the polymer backbones and exhibit hexagonal packing with a lattice parameter of 0.64 nm.

It is also worth mentioning that the peaks centered at 130° and 150° in histograms A-2g and A-2i respectively do not express true phase contrast and are interpret as outliers. This is corroborated by comparing the population of the intervals 130±10° and 150±10°. These intervals represent, in both cases, less than 1% of the entire population, and the peaks can be attributed to instabilities or feedback errors during the scans due to topography induced transient amplitudes. Thus, these peaks do not refer to a variation in the surface composition. . Furthermore, anon-zero standard deviation in phase can follow from errors related to thermal excitation, i.e. typically ~0.5-1° in our experiments, or feedback. Here feedback errors were minimized by keeping the scan axis at speeds below 20 nm s^{-1} as discussed in detail below.

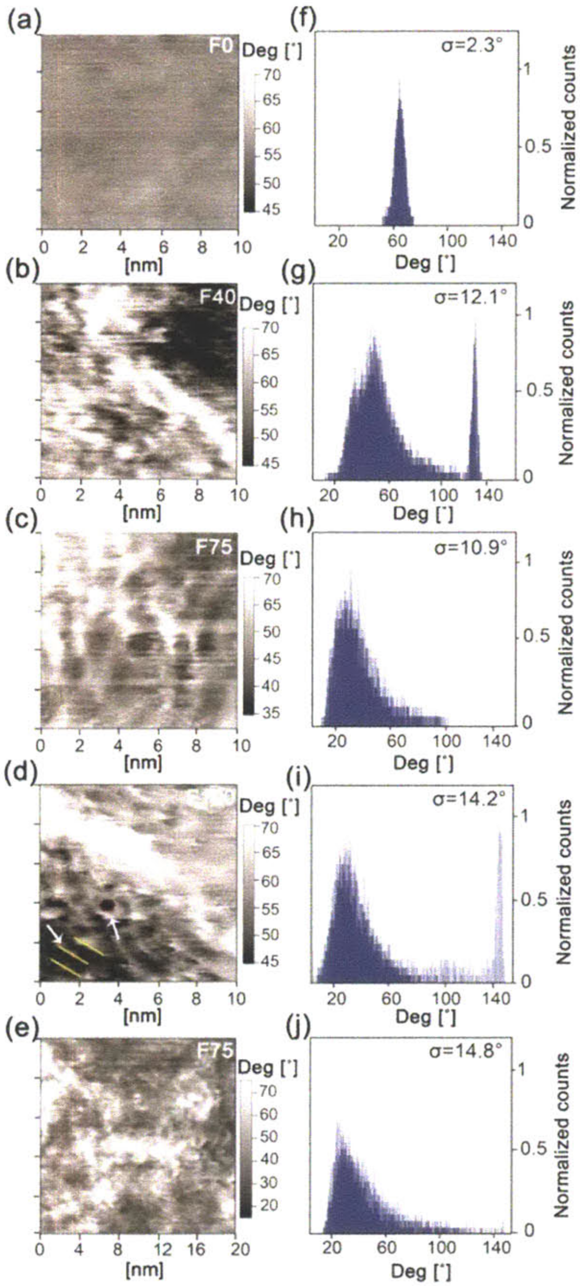

Figure A-2 | 10x10 nm phase images of the (a) F0, (b) F40, (c) F75, (d) F100. All images have been obtained in the SASS mode and with tips with radii of 5 nm or less. In (a) the phase image presents contrast of less than 2 degrees whereas (b), (c) and (d) show nano domains (1-2 nm^2) with greater contrast, i.e. ~10°. Phase image (e) refers to F75. The size of the domains is consistent and scales with a larger scan areas (20x20 nm) as shown in (e). In (d), hexagonal packings of perfluorinated side chains in PFDA repeat units have been highlighted in red and lamellar structures in yellow. Parameters: $A_0 \approx 1$ nm, $A_{sp} \approx 0.3$ nm and scan rate 1Hz. Histograms (f)-(j) represent the distribution of the phase contrast of images (a)-(e) respectively.

It could be argued that the phase contrast observed in Fig. A2b to A-2e could have been an artifact of the non-ideal response of the feedback loop, [29,41] related to the coupling of phase with topography . In order to minimize this effect, small errors in the amplitude signal (maxima ~10 pm) were achieved by 1) scanning rate of. 20nm/s or less in the scan axis, 2) choosing an appropriate number of pixels per scan to allow resolving domains of 0.01 nm^2 or less (pixel size $< 0.01nm^2$), 3) carefully tuning the feedback gains for optimum tracking. Moreover, a correlation study between the height (topography) and the phase signals has been carried out in order to confirm the lack of correlation (Pearson product-moment Correlation Coefficient PCC) between the two observables. In summary, the PCC is centered at zero in all cases giving r= 0.05, -0.18, 0.02 and -0.08 for the images in Fig. A-2a to A-2d respectively. These results confirm that any phase contrast in the images above is related to compositional heterogeneity in the nano-scale rather than error related artifacts.

Note that nano-domains were also resolved in a previous study by means of scanning electron microscopy.[6] In particular, the authors reported larger domain dimensions than those reported here but they did not exclude the possible presence of the smaller domains. Further confirmation of the presence of heterogeneous nano-domains is given by employing force spectroscopy measurements in AM-AFM. In particular, recently proposed force spectroscopy methods[17,42] are exploited to identify compositional heterogeneity in the nano-scale and, possibly, the source of fouling resistance. Conservative and dissipative interactions are recovered as a function of minimum distance of approach d_m (see Materials and Methods section). This allows increasing the number of observables such as F_{AD}, ΔdF_{AD} and $\Delta\Phi^*$. The force of adhesion F_{AD} represents the minimum value in the conservative force and is an important parameter that distinguishes surface heterogeneity[43]. Small variations of F_{AD} can indicate chemically homogeneous surfaces. ΔdF_{AD}, defined as a distance ΔdF_{AD} for which $F_{ts}* \leqslant 0.8|F_{AD}|$, can represent a footprint of nano-scale adsorbed water layer[42], reaching values on the order of 1 nm when adsorbed water films are present on the surface[42]. The arbitrary value 0.8 has been chosen to tolerate a certain level of noise due to reconstruction of force profiles. ΔdF_{AD} can also be employed to qualitatively discriminate between nanoscale variations in terms of the surface energy of a material. For example, ΔdF_{AD} will vary as water adsorbs on a surface[38] and constant ΔdF_{AD} values should follow from homogeneity of surface properties. However, if the sample displays heterogeneity in terms of surface energy this will translate into large variations in ΔdF_{AD}

when measurements are acquired on different regions of the surface.[42] Step-like variations in the normalized phase difference $\Delta\Phi^*$, which occur before mechanical contact between the tip and the surface is established (d_m>0 nm), are related to capillary phenomena and thus to the presence of adsorbed water on the surface[42,44].

Fig. A-3 shows the Fts^* (red lines) and $\Delta\Phi^*$ (black line) versus the minimum distance between the tip and the surface d_m. The datahave been obtained from experimental amplitude-phase-distance (APD) curves acquired at several spots on the four samples. In each figure the two most dissimilar phase and force versus distance profiles, obtained from 100 APD curves randomly acquired on the surface of each polymer, are plotted. Note that since $\Delta\Phi^*$ can be directly related to energy dissipation,[44] the overlapping of $\Delta\Phi^*$ in the figures represents homogeneous energy dissipation profiles.[30] It is only for the F0 homopolymer that a step-like variation ($\Delta\Phi \approx 6°$), highlighted with a red ellipse in Figure 3a, is observed. This signal indicates the presence of capillary interactions and is consistent with the hydrophilic nature of the homopolymer (static contact angle = 65.8° ± 2.1°) and the presence of nano-scale water films on the surface. The corresponding energy dissipation is $E_{dis}(cap) \approx 2$ eV, where *cap* stands for capillary. This value is in accordance with those typically reported in the literature for such phenomena with the use of sharp tips, i.e. $R \leq 5$ nm, as employed here.[45] Conversely, for the three samples containing the hydrophobic compound (PFDA) $\Delta\Phi^* \approx 0$ in the long range, i.e. $d_m > 0$. The lack of long range dissipation, including capillary dissipation, agrees with the intrinsic non-wetting macro-scale nature of the three samples, as confirmed by static contact angle measurements (Table A-1); F40, F75 and F100 assume static contact angles of 115° ± 0.5°, 123° ± 0.2° and 123° ± 0.6° respectively. Dynamic contact angles confirm the non-wetting behavior of these three polymers. In particular, for all three polymers the advancing contact angle reaches a value of approximately 125°. However, F40 polymer is characterized by a receding contact angle of 26° ± 1.8°, which is significantly lower compared to those of F75 and F100. The low receding contact angle of F40 leads to a high degree of contact angle hysteresis (i.e. 96.1° ± 1.5°). It is widely acknowledged that high values of contact angle hysteresis are caused by the presence of regions with contrasting surface properties or by surface roughness.[31,46] In our case, we can disregard the second reason, since the roughness of F40is similar to that of F75 and F100. Other reason behind high values of contact angle hysteresis might be connected to surface reconstruction at the film–water interface.[47] In particular, after contact with water, the surfaces might reconstruct so that the hydroxyl moieties preferentially orient outward and the fluorinated moieties preferentially orient inward.

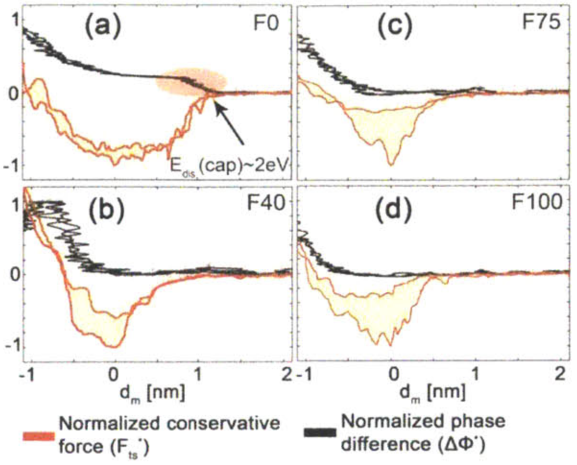

Figure A-3 | Normalized conservative force (Fts*, red lines) and normalized phase difference signal (ΔΦ*, black lines) as a function of d_m. (a) F0, (b) F40, (c) F75, (d) F100. Data were acquired at random spots in each surface. For each sample the most dissimilar results are plotted. Larger green areas imply large variations or heterogeneity in terms of the conservative force profile (b, c, d). All plots show similar dissipative processes via the normalized phase difference $\Delta\Phi^*$ signals (black lines) since these overlap. $\Delta\Phi^*\approx 0$ implies zero dissipation showing that in (b), (c), (d) dissipation occurs mainly after mechanical contact between the tip and the sample ($\Delta\Phi^*\approx 0$ for $d_m > 0$). (a) F0 presents long range dissipative processes with $\Delta\Phi^* > 0$ for $d_m > 0$ (labeled with a red ellipse). |Fts| (minima) ranging between 0.63/0.65, 0.22/0.56, 0.16/0.33, 0.39/1.32 nN and ΔΦ (maxima) ≈ 36°/38°, 8°/9°, 8°/9°, 9°/11°, for samples (a) to (d) respectively. The largest values have been employed to normalize the y axes in each figure. The reference value $d_m = 0$ nm has been taken as coinciding with minima in Fts* and thus indicating the point of mechanical contact.

Contrary to the phase signal, the conservative force F_{ts}^* profiles show remarkable variations (green areas in Fig. A-3) for the polymers containing the hydrophobic matrix. These variations can be quantified by a statistical study based on ΔdF_{AD} (left side Fig. A-4) and F_{AD} (right side Fig. A-4) as obtained from the APD population curves. First, note that only the hydrophilic homopolymer, F0, displays a narrow distribution in F_{AD} (i.e. relative standard deviation 3.6%) centered at 0.64 nN. This provides further confirmation regarding the homogeneous chemical nature of the surface and the absence of heterogeneous nanoscale domains. The other three samples reflect their compositional heterogeneity yielding a broader distribution in terms of F_{AD} (i.e. relative standard deviation 24.7%, 25.6% and 26.1% for the F40, F75, F100 respectively). These stochastic variations in local surface chemical composition, as quantified by F_{AD}, corroborate the findings obtained from phase contrast images in SASS (Fig. A-2b, A-2c, A-2d and A-2e). Second, in terms of ΔdF_{AD}, it can be observed that the F0 homopolymer is characterized by a distribution centered at 1.08 nm (Fig. A-4a) with relative standard deviations of 13.9%, which is indicative of a uniform grade of wettability. Moreover, it implies that the water layer has a thickness in the range of 1nm.[42] For the F40, F75 and F100 polymers, average values of ΔdF_{AD} are on the order of sub-nanometer. These values are closer to those obtained in the absence of nano-scale water films. Standard deviations are 25.9%, 29.8%, 37.5% for F40, F75 and F100 respectively. Variations in ΔdF_{AD}, i.e. standard deviations ~20-40%, might relate to heterogeneity in nano-scale wetting and heterogeneous surface energy (copolymers) or inherent chemical structures that compose the pPFDA homopolymer, F100, as detailed above when discussing Fig. A-2d. The presence of heterogeneity in terms of surface energy discourages any kind of interaction between proteins and polymers as has been confirmed in previous studies conducted with other techniques (i.e NEXFAS spectroscopy).[48]

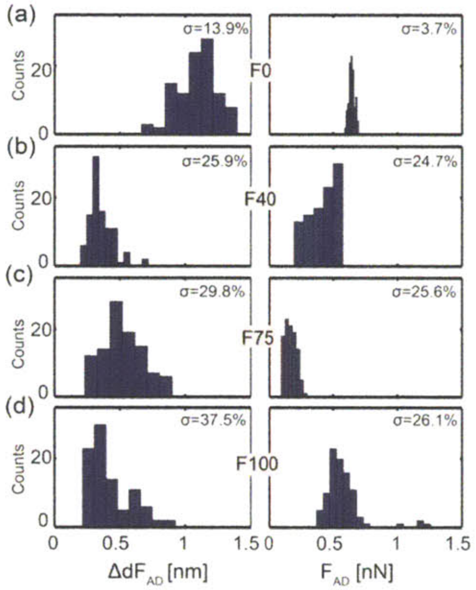

Figure A-4 | Histograms of the population of force curves taken randomly on each sample. (a) F0, (b) F40, (c) F75, (d) F100. For each sample the force of adhesion *(F_{AD})* and distance ΔdF_{AD} are shown. Smaller variations in F_{AD} and larger values of ΔdF_{AD} are observed for the 100% hydrophilic homopolymer (F0, a) as compared to the 100% hydrophobic polymer (F100, d).

A.5 Conclusion

The presence of nano-domains has been confirmed on amphiphilic coatings by employing a minimally invasive and high resolution mode of AM-AFM with SASS under ambient conditions. In particular, it has been demonstrated that the surfaces of the amphiphilic copolymers (i.e., F40, F75) consist of nano-scale domains of compositional heterogeneity. Heterogeneity is also found in these samples in terms of their ability to form nano-scale water films. However, water films patches on the amphiphilic coating are not sufficiently large in the *xy* plane to induce capillary phenomena.[49] In summary, the exceptionally fine resolution of the AM-AFM with SASS operation mode enabled the visualization of nanometer and sub-nanometer domains in amphiphilic copolymers for the first time. This provides direct evidence of the unique film morphology and sheds light on the nature and origin of the fouling resistance of amphiphilic chemistry. The sub-nanometer crystalline structures are also resolved nicely with the AM-AFM technique. This is the first observation of crystalline structures of all iCVD thin film coatings, which is corroborated by XRD measurements. The unprecedented high resolution mapping of molecular domains with simultaneous spectroscopic capabilities resolves the long-lasting challenge of direct visualization of molecular structures and can serve as a powerful tool in the fast-growing fields of nanofabrication and nanotechnology.

ACKOWLEDGMENT

We would like to thank Maritsa Kissamitaki and Martí de Cabo Jaume for producing the visual abstract and figures. C.M. gratefully acknowledges the support of the Masdar Institute in funding this research. K.K.G. and R.Y. thank the King Fahd University of Petroleum and Minerals in Dhahran, Saudi Arabia, for funding the research reported in this paper through the Center for Clean Water and Clean Energy at MIT and acknowledge the support from DOE Office of ARPA-E under award AR0000294.

References

1. Banerjee, I., Pangule, R. C. & Kane, R. S. *Advanced Materials* **23,** 690-718, (2011).
2. Rong Yang, Jingjing Xu, Gozde Ozaydin-Ince, Sze Yinn Wong & Gleason, K. K. *Chemistry of materilas* **3,** 1263–1272, (2011).
3. Werner, C., Maitz, M. F. & Sperling, C. *Journal of material chemistry* **17**, (2007).
4. Yun-Feng Yang, Yang Li, Qing-Lian Li, Ling-Shu Wan & Xu, Z.-K. *Journal of memmbrane science* **362,** 255-264, (2010).
5. Weinman, C. J. *et al. Soft Matter* **6,** 3237-3243, (2010).
6. Wong, S. Y. *et al. Biomacromolecules* **13,** 719-726, (2012).
7. Krishnan, S. *et al. Langmuir* **22,** 5075-5086, (2006).
8. Finlay, J. A. *et al. Langmuir* **24,** 503-510, (2007).
9. Baxamusa, S. H. & Gleason, K. K. *Adv. Funct. Mater.* **19,** 3489-3496, (2009).
10. Zhao, Z. *et al. ACS Applied Materials & Interfaces* **5,** 7808-7818, (2013).
11. Macritchie, F. *Adv. Protein Chem.* **32,** (1978).
12. Gudipati, C. S., Finlay, J. A., Callow, J. A., Callow, M. E. & Wooley, K. L. *Langmuir* **21,** 3044-3053, (2005).
13. Ozaydin-Ince, G., Matin, A., Khan, Z., Zaidi, S. M. J. & Gleason, K. K. *Thin Solid Films* **539,** 181-187, (2013).
14. Rabe, M., Verdes, D. & Seeger, S. *Adv. Colloid Interface Sci.* **162,** 87-106, (2011).
15. Santos, S. *et al. Appl. Phys. Lett.* **103,** 063702, (2013).
16. Guzman, H. V., Perrino, A. P. & Garcia, R. *ACS Nano* **7,** 3198-3204, (2013).
17. Amadei, C. A., Tang, T. C., Chiesa, M. & Santos, S. *The Journal of Chemical Physics* **139,** 084708, (2013).
18. Yang, R., Buonassisi , T., Gleason, K. K. & . *Advanced Materials* **25,** 2078-2083, (2013).
19. Yang, R. & Gleason, K. K. *Langmuir* **28,** 12266-12274, (2012).
20. Wastl, D. S., Weymouth, A. J. & Giessibl, F. J. *Physical Review B* **87,** 245415, (2013).
21. John E Sader *et al. Nanotechnology*, 94-101, (2005).
22. Gan, Y. *Surf. Sci. Rep.* **64,** 99-121, (2009).
23. Giessibl, F. J. *Science* **267,** 68-71, (1995).
24. Fukuma, T., Kobayashi, K., Matsushige, K. & Yamada, H. *Appl. Phys. Lett.* **87,** 034101-034103, (2005).
25. Nic Mullin *et al. Appl. Phys. Lett.* **94,** 173109 - 173109-173103, (2009).
26. Walters, D. A. *et al. Rev. Sci. Instrum.* **67,** 3583-3590, (1996).
27. Santos, S. *et al. Rev. Sci. Instrum.* **83,** 043707, (2012).
28. Katan, A. J., Van Es, M. H. & Oosterkamp, T. H. *Nanotechnology* **20,** 165703, (2009).
29. Cleveland, J. P., Anczykowski, B., Schmid, A. E. & Elings, V. B. *Appl. Phys. Lett.* **72,** 2613-2615, (1998).
30. Tamayo, J. & Garcia, R. *Appl. Phys. Lett.* **73,** 2926-2928 (1998).
31. Eral, H. B., 't Mannetje, D. J. C. M. & Oh, J. M. *Colloid Polym. Sci.* **291,** 247-260, (2013).
32. Anand, G., Sharma, S., Dutta, A. K., Kumar, S. K. & Belfort, G. *Langmuir* **26,** 10803-10811, (2010).
33. San Paulo, A. & García, R. *Biophys. J.* **78,** 1599-1605, (2000).
34. Santos, S. *et al. Nanotechnology* **22,** 345401, (2011).
35. Sergio, S., Albert, V., Tewfic, S., Neil, H. T. & Matteo, C. *Nanotechnology* **22,** 465705, (2011).
36. Ricardo Garcia, Javier Tamayo & Paolo, A. S. *Surface and interfaces analysis* **27,** 312-316, (1999).
37. Anna Maria Coclite , Yujun Shi & Gleason, K. K. *Adv. Funct. Mater.* **22,** 2167–2176, (2012).
38. Roach, P., Farrar, D. & Perry, C. C. *J. Am. Chem. Soc.* **127,** 8168-8173, (2005).
39. Honda, K., Morita, M., Otsuka, H. & Takahara, A. *Macromolecules* **38,** 5699-5705, (2005).
40. Volkov, V. V. *et al. Polymer* **33,** 1316-1320, (1992).

41. Kaggwa, G. B., Kilpatrick, J. I., Sader, J. E. & Jarvis, S. P. *Appl. Phys. Lett.* **93,** 011909, (2008).
42. Amadei, C. A., Santos, S., Pehkonen, S., Verdaguer, A. & Chiesa, M. *J. Phys. Chem. C* **117,** 20819–20825, (2013).
43. Butt, H. J., Cappella, B. & Kappl, M. *Surf. Sci. Rep.* **59,** 1-152, (2005).
44. Santos, S., Amadei, C. A., Verdaguer, A. & Chiesa, M. *The Journal of Physical Chemistry C* **117,** 10615-10622, (2013).
45. Zitzler, L., Herminghaus, S. & Mugele, F. *Physical Review B* **66,** 155436, (2002).
46. Raj, R., Enright, R., Zhu, Y., Adera, S. & Wang, E. N. *Langmuir* **28,** 15777-15788, (2012).
47. Erbil, H. Y., McHale, G., Rowan, S. M. & Newton, M. I. *Langmuir* **15,** 7378-7385, (1999).
48. Krishnan, S. *et al. Macromolecules* **43,** 4733-4743, (2010).
49. Yaminsky, V. V. *Colloids and Surfaces A* **159**, (1999).